Inaugural dissertation

For obtaining the doctoral degree of the

Combined Faculty of Mathematics, Engineering and Natural Sciences

of the

Ruprecht - Karls – University Heidelberg

Presented by

M.Sc. Anna Platzek

Born in: Bad Kreuznach/ Germany

Oral examination: 27.05.2025

Organellar remodeling during stress in *Saccharomyces cerevisiae*

DISSERTATION

Anna Platzek

Heidelberg
2025

Referees: Prof. Dr. Britta Brügger
Prof. Dr. Sebastian Schuck

SUMMARY

Cells have to adapt rapidly to changing physiological demands, such as differentiation, stress and disease. Extensive studies have defined many stress response pathways at the level of gene activity and protein abundance, but stress-induced changes of protein subcellular localization have not been investigated comprehensively on a proteome-wide level.

In this thesis, I established and applied the Dynamic Organellar Maps (DOMs) approach by label-free mass spectrometry for the first time to yeast. DOMs detected protein localization changes of native, untagged proteins upon different stresses.

Firstly, I used endoplasmic reticulum (ER) stress and found that almost 10% of the known proteins expressed in yeast, shifted within or between organelles. I showed that a distinct multitude of secretory pathway proteins accumulated in the ER. In-depth analysis and experimental validation refined the extent and selectivity of misfolded proteins retained in the ER. Moreover, I identified new ER proteins subjected to the ER reflux pathway and identified transmembrane components of reticulon clusters, which separated from the residual ER. Lastly, I demonstrated that nuclear pore complex integrity was altered which affected nuclear import.

Secondly, I applied DOMs to nitrogen-starved cells to identify novel cargo proteins which were degraded by non-selective macroautophagy. I detected several proteins which were already known to be autophagic cargos or to be involved in cargo recruitment and transport. Further analysis provided a list of candidate cargo proteins which serve as a basis to determine if starvation induced autophagy degrades cargo proteins non-selectively.

In conclusion, I established DOMs in yeast and revealed that global and suborganellar changes in protein localization are key elements of cellular stress responses.

ZUSAMMENFASSUNG

Zellen müssen sich schnell an verändernde physiologische Anforderungen wie etwa Differenzierung, Stress und Erkrankungen anpassen. In umfangreichen Studien wurden viele Stressreaktionswege auf der Ebene der Genaktivität und der Häufigkeit von Proteinen definiert, allerdings wurden stressbedingte Veränderungen der subzellulären Lokalisierung von Proteinen bisher nicht umfassend auf Proteom--Ebene untersucht.

In meiner Doktorarbeit habe ich die Methode, Dynamic Organellar Maps (DOMs), mithilfe unmarkierter Massenspektrometrie in Hefe etabliert und angewandt. Mit DOMs wurden Veränderungen der Proteinlokalisierung von nativen, nicht-markierten Proteinen unter verschiedenen Stresssituationen untersucht.

Zunächst habe ich das endoplasmatische Retikulum (ER) gestresst und festgestellt, dass sich fast 10 % der bekannten Proteine, die in Hefe exprimiert werden, innerhalb oder zwischen den Organellen bewegen. Ich zeigte, dass sich eine Vielzahl von Proteinen des sekretorischen Weges im ER anreicherten. Eine eingehende Analyse und darauffolgende experimentelle Validierung präzisierten das Ausmaß und die Selektivität der im ER zurückgehaltenen fehlgefalteten Proteine. Darüber hinaus habe ich neue ER-Proteine identifiziert, die dem ER-Reflux unterworfen sind, und Transmembrankomponenten von Retikulon-Clustern identifiziert, die sich vom restlichen ER abgetrennt haben. Schließlich konnte ich zeigen, dass die Integrität des Kernporenkomplexes verändert war, was sich auf den Kernimport auswirkte.

Zweitens wandte ich DOMs in Zellen an die unter Stickstoffentzug litten, um neue Zielproteine zu identifizieren, die durch nichtselektive Makroautophagie abgebaut werden. Ich fand mehrere Proteine, von denen bereits bekannt war, dass sie Zielproteine von Autophagie sind oder an der Rekrutierung und dem Transport von ihnen beteiligt sind. Weitere Analysen ergaben eine Liste von potentiellen Kandidaten, die als Grundlage dienen, um zu bestimmen, ob die durch Nährstoffmangel induzierte Autophagie Zielproteine nicht-selektiv abbaut.

Zusammenfassend lässt sich sagen, dass ich erfolgreich DOMs in Hefe etabliert habe. Ich konnte zeigen, dass globale und suborganellare Veränderungen der Proteinlokalisierung Schlüsselelemente zellulärer Stressreaktionen sind.

TABLE OF CONTENTS

PUBLISHED DATA AND CONTRIBUTIONS

All experiments presented in this thesis were conceptualized, performed, analyzed and arranged, by me unless otherwise stated in this section, the results section and in figure legends.

A significant fraction of the data presented in this thesis, was recently published as a preprint article (*Platzek et al., 2025*). This includes data presented in figures 2, 4, 5, 6A, 6B, 7, 9, 10A, 11A, 11B, 12A, 12C, 13A, 13C, 13D, 14C.

I adapted and optimized the subcellular fractionation to yeast with the contribution of Sebastian Schuck and Georg Borner.

Mass spectrometry data acquisition was performed by Georg Borner, Alexandra Davies and Vincent Albrecht. Initial mass spectrometry data processing was performed by Georg Borner and Vincent Albrecht. The DOM-ABC web app (*Schessner et al., 2023*) was used for data quality filtering and normalization, protein assignment to predefined organellar marker proteins (SVM compartment classification) and analysis of shifting proteins (MR analysis). The reference database and the organellar marker list were generated by Sebastian Schuck. Detailed mass spectrometry data analysis, including analysis of the full proteome, cytosolic shift analysis, organellar shift analysis, neighborhood analysis was performed by Georg Borner.

I performed all principal component analyses and generated the corresponding plots in figures 4A, 6A, 6D, 9A, 11B, 12A, 12C, 13A, 15, 16C, 17B based on the adapted source code at https://github.com/JuliaS92/SpatialProteomicsQC (*Schessner et al., 2023*) with minor modifications to the layout.

Descriptions of methods that I had not performed myself include “Mass spectrometry acquisition”, “Mass spectrometry raw data analysis”, “Generation of compartment marker list”, “Organellar mapping data analysis in DOM-ABC web app”, “Full proteome quantification analysis”, “Cytosolic pool analysis”, “Identification of proteins shifting towards the ER during ER stress”, which were obtained from (*Platzek et al., 2025*) and had originally been written by Sebastian Schuck or Georg Borner.

Klára Odehnalová generated the yeast strain SSY4355 and acquired images in Figure 9B. Sebastian Schuck generated the strains SSY60 and SSY61 used for the starvation maps.

All python scripts that I developed for data analysis and generation of plots were improved with ChatGPT-4 by OpenAI.

LIST OF ABBREVIATIONS

AIM	Atg8-interacting motif
ALP	alkaline phosphatase
ATG	Autophagy-related gene
COP	coat protein complex
CPY	carboxypeptidase Y
Cvt	cytoplasm-to-vacuole targeting
DDA	data-dependent acquisition
DIA	data-independent acquisition
DTT	dithiothreitol
ER	endoplasmic reticulum
ERGIC	ER-Golgi intermediate compartment
ESCRT	endosomal sorting complex required for transport
FG-nucleoporin	phenylalanine-glycine-rich nucleoporin
GFP	green fluorescent protein
GO	gene ontology
GPI-AP	glycosylphosphatidylinositol-anchored protein
HTL	HaloTag ligand
IB	immunoblotting
LC-MS	liquid-chromatography mass spectrometry
mNG	mNeonGreen
MVB	multivesicular body
NE	nuclear envelope
neon	mNeonGreen
NLS	nuclear localization signal
NPC	nuclear pore complex
OST	oligosaccharyltransferase
PA	phosphatidic acid
PAS	phagophore assembly site
PM	plasma membrane
PS	phosphatidylserine
SAM	S-adenosylmethionine
FAS	Fatty acid synthetase
RHD	reticulon homology domain
Scarlet	mScarlet-i3
SDS-PAGE	Sodium dodecyl sulfate polyacrylamide gel electrophoresis
sfGFP	superfolder green fluorescent protein
ss	signal sequence
Tm	tunicamycin
TORC1	target of rapamycin complex 1
UPR	unfolded protein response
WT	wildtype

1 INTRODUCTION

1.1 Protein trafficking

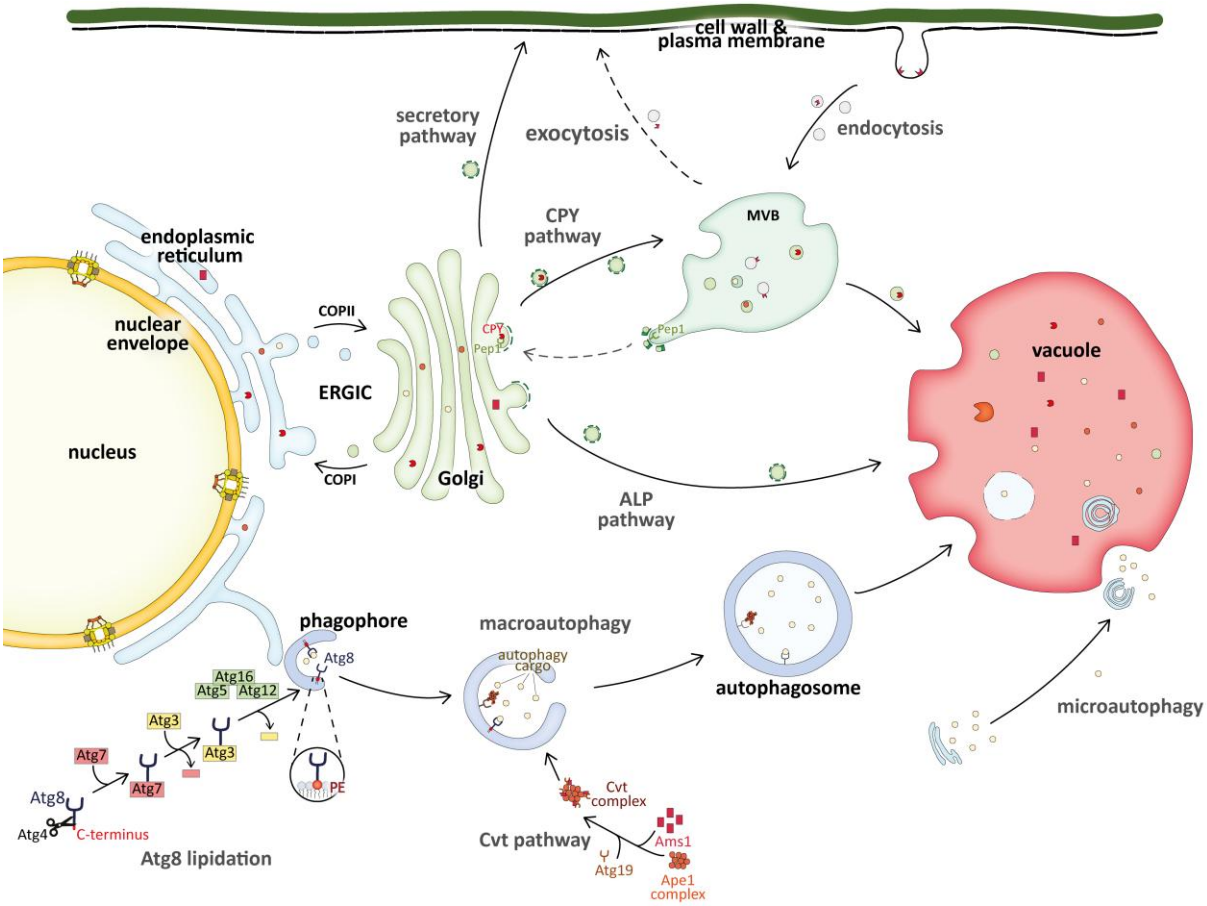

Figure 1: Protein trafficking pathways in yeast. Secretory proteins are synthesized, glycosylated and folded in the ER. They are transported in specialized COPII vesicles via the ER-Golgi intermediate compartment (ERGIC) to the Golgi apparatus. From there they are further modified and sorted for transport to the vacuole, the plasma membrane or secreted from the cell. There are three main pathways for transport of vacuolar proteins in yeast (1) the carboxypeptidase Y (CPY) pathway via the multivesicular body (MVB) compartment (2) the direct alkaline phosphatase (ALP) pathway and (3) the cytoplasm-to-vacuole targeting (Cvt) pathway, using autophagosome-like vesicles for transport. Upon nutrient deprivation or low energy state, macro- and microautophagy are activated, transporting unused or unfunctional proteins and organelles to the vacuole for degradation. Nuclear-cytoplasmic exchange is regulated by nuclear-pore complexes (NPC) in the nuclear envelope. In order to signal to communicate with other cells through the extracellular space, endocytosis internalizes plasma membrane proteins and molecules and transport these to the MVB for sorting. Scheme generated by me.

Eukaryotic cells maintain several specialized membrane-enclosed compartments, called organelles to organize and hence regulate metabolic processes spatially and temporally (*Diekmann and Pereira-Leal, 2013*). In order to maintain the organelle identities, composition and altogether maintain cellular homeostasis, characteristic proteins are constantly synthesized and delivered throughout the cell to their destination organelle (Figure 1). About

70% of all proteins are translated by ribosomes in the cytosol and depending of their targeting sequence post-translationally transported and translocated into the nucleus, mitochondria, ER or peroxisomes (*Panzner et al., 1995; Wu et al., 2019*). About one third of the proteins are destined for the lumen and membrane of organelles. These secretory proteins contain hydrophobic signal sequences (*Walter and Blobel, 1980*) which are recognized by the ribosome and the translocon and activate translocation into the lumen of the endoplasmic reticulum (ER) (*Nyathi et al., 2013; Rapoport et al., 2017*). Membrane proteins with a single C-terminal transmembrane domain, called tail-anchored proteins, are bound in the cytosol by Get3 and ER membrane insertion is mediated by other components of the Get pathway in the membrane (*Schuldiner et al., 2008*).

During co-translational translocation of the nascent ER resident polypeptide, the signal peptidase removes the N-terminal 15 to 30 amino acids (*Evans et al., 1986*) and the oligosaccharyltransferase (OST) complex transfers an oligosaccharide onto a selected asparagine of the nascent polypeptide (*Chen et al., 2001*), which is further modified in ER and Golgi (*Zhang and Wang, 2016*). The ER lumen contains chaperones and other protein-folding enzymes which assist and accelerate the folding of the polypeptide chain into the functional structure. In order to keep or retrieve these ER resident proteins in the ER, they contain an ER retention signal. Correctly folded proteins are recognized by specific cargo receptors (*Miller et al., 2003; Strating and Martens, 2009*) and packed into specialized coatomer protein (COP)II vesicles and exported via the ER-Golgi intermediate compartment (ERGIC) to the Golgi apparatus for further modifications (*Barlowe et al., 1994*). The receptors are transported back to the ER in COPI vesicles, together with falsely targeted ER resident proteins recognized by an ER retrieval sequence (*Pelham et al., 1988; Nickel and Wieland, 1997*). Depending on the destination organelle and the function, mature proteins in the Golgi are transported to the plasma membrane and cell wall via the secretory pathway (*Spang, 2015*) or secreted into the extracellular space (*TerBush et al., 1996*). Proteins targeted to the vacuole lumen use two conserved pathways: the Pep1-dependent carboxypeptidase Y (CPY) pathway or the direct adaptor protein 3 (AP-3)-dependent alkaline phosphatase (ALP) pathway. In yeast there is a third pathway, the cytosol-to-vacuole transport (Cvt) pathway transports specific vacuole enzymes.

In the CPY pathway, the cargo receptor for several yeast vacuolar hydrolases and proteases Pep1/ Vps10, cycles between Golgi and prevacuolar compartment (here called multivesicular

body, MVB) (*Cooper and Stevens, 1996*). Pep1 binds glycosylated soluble cargo proteins in the late-Golgi and transports it inside of clathrin-coated vesicles towards the endosome-like compartment, the multivesicular bodies (*Pearse and Robinson, 1990*). Transmembrane proteins which use the CPY pathway require the family of GGA proteins to facilitate transport (*Hirst et al., 2000*).

The MVBs receive material from both the CPY pathway and the endocytic pathway, in which plasma membrane proteins and macromolecules from the extracellular environment are internalized in clathrin-coated vesicles (*Robinson, 1997*).

The ALP pathway is a direct pathway from the Golgi to the vacuole and its most promiment cargo is the alkaline phosphatase Pho8 (*Stepp et al., 1997; Cowles et al., 1997*).

The Cvt pathway was only identified in yeast and targets the peptidases Ape1 and the mannosidase Ams1 to the vacuole via specialized vesicles (*Lynch-Day and Klionsky, 2010*).

The cargo proteins are recognized by two cargo receptors Atg19 and Atg34 (*Scott et al., 2001; Suzuki et al., 2010*) and thereby tethering these to the membrane of specialized Cvt vesicles. These vesicles are constitutively formed using the autophagy machinery but are smaller in size compared to autophagosomes (*Baba et al., 1997; Khalfan and Klionsky, 2002*).

Upon nutrient deprivation or low energy state of the cell, distinct autophagy pathways are activated. Autophagy transports cargo proteins and organelles marked for degradation either directly to the vacuole (microautophagy), by chaperones (chaperone-mediated autophagy, not in fungi) or by sequestering cargos in a double membrane vesicle, called the autophagosome (macroautophagy). In the vacuole cargos are degraded and single amino acids are further used for signaling and synthesis of essential proteins to maintain cellular homeostasis (*Metur and Klionsky, 2024*).

In order to provide integrity of the nucleus and a constant exchange of molecules and proteins between nucleus and other organelles, nuclear pore complexes (NPCs) are embedded in the nuclear envelope (*Paine et al., 1975; Dultz et al., 2022*). These large multimeric complexes recognize RNA and proteins in both nucleoplasm and cytoplasm. Because of the intrinsically disordered phenylalanine-glycine rich nucleoporins, in the cytosolic interface and the channel, the nuclear pore complex has a natural diffusion barrier.

Transport of RNA and proteins is regulated by recognition of a nuclear localization sequence by specific receptors, called importins, which guide the cargo proteins through the pore into the nucleus (*Kalderon et al., 1984; Gorlich et al., 1995; Li et al., 2016*).

1.2 ER stress

The ER is the largest membrane-bound organelle of a cell and enables protein synthesis and modification, lipid metabolism and organelle communication. It has to adapt rapidly in size and shape to changing physiological conditions, such as differentiation, disease, and toxins (*Schwarz and Blower, 2016*). Two common chemical inducers of ER stress in both yeast and mammalian tissue culture are dithiothreitol (DTT) and tunicamycin (Tm). The reducing agent DTT interferes with the oxidizing lumen of the ER and hence disrupts disulfide-bond formation (*Braakman et al., 1992*). Tunicamycin inhibits the first step of N-linked glycosylation (*Barnes et al., 1984*), resulting in lack of glycosylation. Hypoglycosylation of proteins will also lead to accumulation of misfolded proteins (*Travers et al., 2000*).

In yeast, these triggers impair proper folding and maturation of newly synthesized proteins, but also the tremendous amount of newly synthesized proteins can result in exceeding the maximum folding capacity of the ER. Since only correctly folded proteins can leave the ER, proteins accumulate and the cell experiences ER stress.

This accumulation results in expansion of the ER and increase of its volume, called ER dilation (*Bernales et al., 2006; Schuck et al., 2009*).

Several stress response mechanisms are activated to restore organellar and cellular function. ER associated degradation (ERAD) recognizes misfolded proteins in the ER, retranslocates those into the cytosol where they are labeled and degraded by the proteasome (*Smith et al., 2011*). The unfolded protein response (UPR). The transmembrane kinase Ire1 and misfolded proteins compete for binding of the lumenal ER chaperone Kar2 (*Bertolotti et al., 2000*), on the other hand it was suggested that Ire1 directly binds misfolded proteins which function as activating ligands (*Gardner and Walter, 2011*). Dissociation of Kar2 from the lumenal domain of Ire1 drives oligomerization, trans-autophosphorylation of Ire1 (*Shamu and Walter, 1996*) and subsequent activation of its RNAase activity. Ire1 generates a spliced variant of HAC1 mRNA, which functions as a transcription factor after translation and upregulates genes involved in ER quality control machinery to enhance translocation, folding, transport and

clearing of accumulated misfolded proteins (*Cox et al., 1997; Travers et al., 2000; Walter and Ron, 2011*) and downregulates ribosome biogenesis (*Pincus et al., 2014*).

Additionally, Ire1 is able to sense aberrant lipid compositions, which are triggered by depletion of inositol, increased lipid saturation, altered lipid packing density (*Cox et al., 1997; Volmer et al., 2013; Halbleib et al., 2017; Radanovic and Ernst, 2021; Reinhard et al., 2024*). These perturbations of the physicochemical properties of the ER membrane are called lipid bilayer stress.

Lastly, after prolonged ER stress, both selective and non-selective autophagy degrade parts of the ER through which misfolded proteins and excess aberrant ER domains are removed (*Bernales et al., 2006; Schuck et al., 2014; Fregno and Molinari, 2018*).

These transcriptional responses and morphological changes affect the entire cell and have been thoroughly analyzed. However, it has not been investigated systematically which proteins relocate and how this might affect organelle composition, structure and function.

1.3 Autophagy by nitrogen-starvation

When cells are deprived of amino acids and nitrogen, the central regulator of growth and metabolism, target of rapamycin complex 1 (TORC1) is inactived through several upstream amino-acid sensing complexes and relocalizes from the vacuole to distinct perivacuolar sites (*Loewith and Hall, 2011; Hughes Hallett et al., 2015*). The loss of phosphorylation activates two distinct types of autophagy in yeast: microautophagy and macroautophagy. The former involves direct transport and invagination of cargos into the vacuole. This is often mediated by the endosomal sorting complex required for transport (ESCRT) protein (*Hatakeyama and De Virgilio, 2019; Schuck, 2020*).

Upon activation of macroautophagy, the Atg1 protein kinase complex recruits downstream factors to a specialized phagophore assembly sites (PAS), mostly confined to the vacuole but also found at the ER (*Hollenstein et al., 2019; Bieber et al., 2022*).

The phosphatidylinositol 3-kinase complex I is recruited to the PAS, where it subsequently recruits scaffold proteins and lipids to initiate formation of a double-membrane structure, called phagophore. While the phagophore expands, it engulfs proteins, aggregates and organelles marked for degradation. The membrane closes to form the autophagosome and is subsequently fused with the vacuole to degrade and release the degradation products back into the cytoplasm. The family of proteins involved in these processes are called autophagy-

related genes (Atg) (*Takeshige et al., 1992*). Together they mediate cargo recruitment, formation, expansion, closure and fusion (*Mizushima et al., 2011*).

Autophagy can be either non-selectively sequester and degrade cytosolic proteins and molecules (*Baba et al., 1994*) or selectively recognize proteins and organelles by autophagy receptors. These receptors bind ubiquitylated cargo and tether it to the phagophore membrane-anchored Atg8 via their Atg8 interacting motif (AIM) (*Rogov et al., 2014; Johansen and Lamark, 2011*).

In order to tether Atg8 to the phagophore membrane a ubiquitin-like conjugation machinery mediates activation, conjugation and transfer onto the lipid (Figure 1, bottom left). (1) the C-terminus of Atg8 is cleaved off by the protease Atg4; (2) Atg8 is conjugated to the E1-like activating enzyme, Atg7, by its new C-terminal glycine; (3) Atg8 is transferred to the E2-like conjugating enzyme, Atg3; (4) Atg8 is conjugated to the lipids phosphatidylethanolamine (PE) or sometimes phosphatidylserine (PS) in the phagophore membrane, mediated by the E3-like ligase, Atg5-Atg12-Atg16 complex (*Ichimura et al., 2000; Hanada et al., 2007*).

Incorporation of Atg8 in the phagophore membrane enables not only cargo binding, but also provides a scaffold for downstream factors (*Kaufmann et al., 2014*) and creates curvature to promote vesicle formation (*Carlsson and Simonsen, 2015*).

In order to understand the physiological role of autophagy for maintenance of cellular homeostasis, cargo proteins, selective autophagy receptors and regulatory mechanisms were stepwise identified. In the first years after detection of autophagy, autophagic and Cvt cargos have been mainly identified by electron-microscopy (*Baba et al., 1994; Baba et al., 1997*) and laborious analysis of autophagy-deficient mutants (*Tsukada and Ohsumi, 1993; Thumm et al., 1994; Harding et al., 1996*) in microscopy-based (*Oda et al., 1996; Suzuki et al., 2002*) or biochemical assays (*Noda et al., 1995; Noda and Klionsky, 2008*).

A faster and more systematic method to examine autophagic cargo and cargo selectivity was proteomic profiling of autophagosomes. By fractionation or immunoprecipitation of autophagosomes, they successfully identified specific cytosolic complexes to be selectively degraded (*Suzuki et al., 2014*) and new receptors for selective autophagy of ribosomes and glycogen (*Takeda et al., 2024; Isoda et al., 2024*). However, these approaches were always limited to autophagosomal content and neglect the effect of starvation and autophagy-

deficiency on other degradative pathways such as microautophagy or the ERAD pathway; and it does not recognize factors outside of the autophagosome lumen.

In recent years starvation-induced autophagy has been found to not randomly sequester cytoplasmic material but selectively degrade cytosolic cargos, mRNA or ribosomes (*Makino et al., 2021; Isoda et al., 2024; Takeda et al., 2024*). These results raise additional questions to understand the interplay of selective and non-selective autophagy: Are specific proteins and molecules selectively degraded upon starvation and if there is selectivity, how is it mediated? Using an unbiased, proteome-wide, mass spectrometry approach, I tried to identify novel cargo proteins which were selectively degraded by starvation-induced autophagy.

1.4 Dynamic organellar mapping

The cellular stress response does not only involve regulation of transcription and translation but also changing size and shape of organelles. Thereby, proteins change their localization within an organelle (suborganellar) or relocate throughout the entire cell. In order to monitor localization changes, proteins of interest are often labeled with fluorescent probes after fixation or by adding another fluorescent tag directly *in cellulo*. Using extensive fluorescently tagged strain collections, many high-throughput microscopy studies have been performed to detect protein localization (*Huh et al., 2003; Meurer et al., 2018*) and protein localization changes upon different conditions (*Tkach et al., 2012; Breker et al., 2013*). However, these microscopy based approaches are often time-consuming and might affect expression levels, protein localization and function. Therefore, in the strain collections of *Saccharomyces cerevisiae* several proteins can never be evaluated correctly, such as proteins with signal sequences for ER, mitochondria or peroxisomes, lumenal ER proteins with retention sequences, glycosylphosphatidylinositol-anchored proteins (GPI-APs) and other tail-anchored proteins. In recent years, mass spectrometry has evolved into a powerful tool for protein profiling through interaction networks and more recently localization through organelle profiling (*Lundberg and Borner, 2019*). Until now only one study has applied organellar profiling to unperturbed yeast to identify native protein localization (*Nightingale et al., 2019*), but changes in protein localization were never detected.

Thus, I applied a label-free organelle profiling mass-spectrometry (MS) approach called Dynamic Organellar Maps (DOMs) (*Itzhak et al., 2016; Schessner et al., 2023*) to *Saccharomyces cerevisiae*. This method detects proteins on a proteome-wide scale and

predicts protein localization of yet undefined proteins. By comparing maps made under different conditions protein localization changes are detected, suborganellar structures further characterized, stress response and disease pathways redefined (*Itzhak et al., 2016; Davies et al., 2018; Kozik et al., 2020; Schessner et al., 2023*).

To generate an organellar map (Figure 2) cells are gently lysed and homogenized to separate organelles but keep them intact. Then, organelles are partially separated by 6 differential centrifugation steps at 1,000 g, 3,000 g, 6,000 g, 12,000 g, 24,000 g and 78,000 g, referred to as 1k-78k fractions. Hereby, larger and denser organelles or microsomes will sediment in the earlier fractions, whereas protein complexes will sediment in the later fractions (*Graham, 2001*). The distribution of each protein across fractions is measured by liquid-chromatography mass spectrometry (LC-MS), creating a unique abundance profile for each detected protein. Hereby, proteins associated with the same organelles and complexes display similar distribution across fractions and thus similar abundance profiles. The entirety of all abundance profiles is called organellar map.

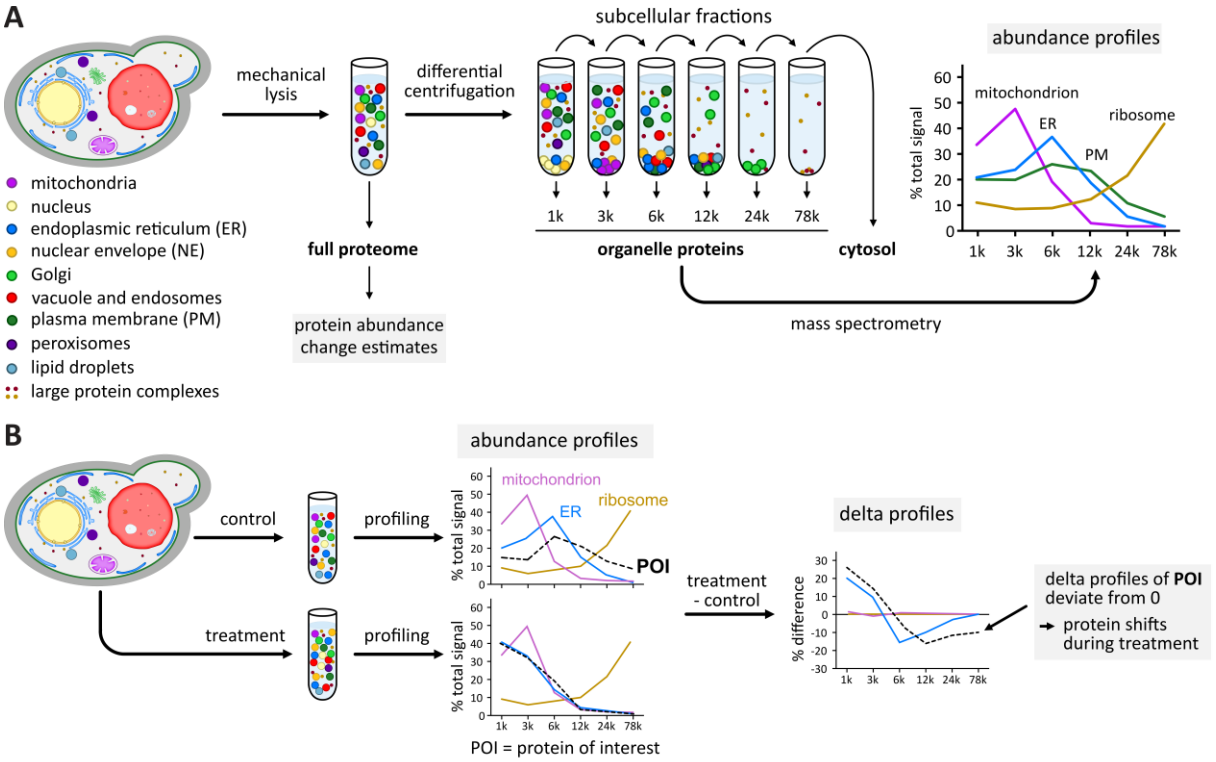

Figure 2: Workflow for organellar mapping and dynamic organellar mapping. (**A**) Workflow to generate an organellar map. Cells are lysed, homogenized, and subjected to differential centrifugation. The full proteome sample (homogenized cell lysate), six membrane fractions (1k-78k) and one cytosol fraction (supernatant 78k) are analyzed by quantitative label-free liquid-chromatography mass spectrometry. The distribution of each protein across the 6 membrane fractions displays the abundance profile of each protein. Proteins associated with the same organelle display similar abundance profiles. All abundance profiles together represent an organellar map. (**B**) Workflow for dynamic organellar mapping. Organellar maps are generated under different conditions and abundance profiles compared by subtracting the treatment profiles from the

control profiles to obtain delta profiles. If a protein changes their localization upon the treatment, their delta profile shows the change in distribution. Based on the delta profiles proteins which significantly change their localization are identified. (A) and (B) were adapted from (*Platzek et al., 2025*) and modified.

Normalizing the intensities of the 6 fractions of each replicate ensures that the resulting abundance profiles are unaffected by protein abundance changes of the respective treatment. Hence, ensuring that the data analysis remains unbiased.

Dimensionality reduction via principal components analysis (PCA) is performed, to visually assess quality and reproducibility of the organellar map. To identify significant protein localization changes, the abundance profiles of maps made under different conditions are subtracted from each other, creating a delta profile. The delta profile of a protein shows the changes of distribution across the fractions. For each protein the magnitude of changes (Movement score) is determined by a multivariate outlier test (*Fauconnier and Haesbroeck, 2009*) and the consistency across replicates (Reproducibility score) is evaluated by the Pearson correlation (*Itzhak et al., 2016*). Plotting Movement score against Reproducibility score and choosing unique cut-offs based on the experimental design, identifies consistently significantly relocalizing proteins.

The predicted organellar translocations are evaluated visually by PCA maps, support vector machine (SVM) analysis, cytosol shift analysis, organellar shift analysis and nearest neighbor analysis.

PCA maps serve as initial instance to evaluate effects of a treatment on proteome remodeling. They show protein association with a cluster and shifting of these proteins and organelle associated proteins upon the respective treatment when comparing control and treated maps. The SVM analysis enables an approximate analysis of directions of shifts, based on supervised non-linear separation of classes to define distinct clusters. By providing a list of proteins with known localization, the marker list, new proteins are assigned to a specific cluster of an organelle (*Varmuza and Filzmoser, 2009*). This allows novel evaluation of unknown proteins and reevaluation of proteins in reference databases. The supernatant of the 78k fraction contains mainly cytosolic proteins or proteins dissociated from organelles, hence is called cytosol fraction. Calculating the proportion of the cytosol fraction over all membrane fractions (sum of 1k-78k) provides information about the cytosolic pool of a protein and includes information about the large class of cytosolic proteins. Comparing the cytosolic pools of a protein under different conditions determines the cytosolic shift and hence reveals additional localization changes towards or away from the cytosol. The

organellar shift analysis and nearest neighbor analysis are both based on the correlation of protein abundance profiles with averaged marker profiles and single protein profiles, respectively. The organellar shift analysis reveals the direction of a protein localization change and identifies proteins shifting within, towards or away from a respective organelle. The nearest neighbor analysis identifies other proteins whose profiles highly correlate with the protein of interest profile (*Borner et al., 2014*). This enables both prediction of protein interactions and evaluation of changing surrounding proteins, the neighborhood, upon a localization change.

Applying DOMs to *Saccharomyces cerevisiae* upon different stresses together with the collection of analyses will enable me to reevaluate the native protein composition of organelles, identify suborganellar localizations and proteins in proximity to each other and ultimately uncover global and local stress response mechanisms.

2 AIMS OF THIS THESIS

Organellar remodeling upon various stresses has been studied extensively in the past. In this study I propose that changes in protein localization are an underappreciated aspect of the cellular stress response.

My aims were:

(1) Establishing DOM in the budding yeast *Saccharomyces cerevisiae*, to enable assignment of all native proteins to an organelle or suborganellar compartments

(2) Applying DOM to ER stressed cells to reveal novel proteins affected and pathways involved in the cellular stress response.

(3) Applying DOM to nitrogen-starved cells to discover novel cargo proteins degraded by non-selective macroautophagy.

3 RESULTS

3.1 Establishing organellar mapping in yeast

Dynamic organellar mapping has been successfully applied to different organisms and tissues such as cultured human cells (*Itzhak et al., 2016*) and mouse primary neurons (*Itzhak et al., 2017*). To establish this method in yeast I slightly adapted and optimized the protocol regarding cell lysis, homogenization and removal of unbroken cells (*Itzhak et al., 2019*).
In order to not additionally stress the cells, I modified the cell wall removal, the spheroplasting, as such to not perform DTT incubation prior to prolonged zymolyase treatment. Spheroplasting efficiency was decreased compared to the previous protocol which included destabilization of the cell wall by 10 min DTT treatment. Because many cells were not lysed and homogenized completely, I included a short clearing spin to remove unbroken cells. This ensured that only organelles, microsomes and big protein complexes were sedimented in the subsequent centrifugation steps. Using the proposed centrifugation steps to separate but not purify the organelles, resulted in heterogeneously distributed organellar markers across the different fractions (Figure 3).

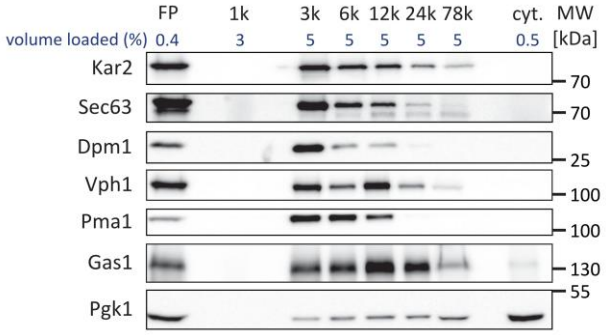

Figure 3: Optimization of subcellular fractionation of W303 wildtype control cells. The immunoblot shows the differential distribution of specific organellar proteins across the subcellular fractions. In dark blue annotated is the proportion of total sample volume loaded, being able to compare signal intensities. Antibodies stained organelles as follows: Kar2, ER lumen; Sec63, ER membrane; Dpm1, ER membrane (tail-anchored); Vph1, vacuole membrane; Pma1, plasma membrane; Gas1, cell wall; Pgk1, cytosol. Experiment was conceptualized, performed and arranged by me.

I generated preliminary organellar maps (data not shown) and Georg Borner analyzed them by LC-MS to further optimize dounce homogenization and to confirm that my organelles were separated sufficiently as they formed distinct clusters in a PCA plot.

3.2 Generation of reference maps

After successfully optimizing the workflow, I generated 6 maps from exponentially growing, untreated wildtype (WT) cells in technical duplicates on 3 different days. These reference maps serve to generate a marker list based on existing reference datasets (*Kraus et al., 2017; Ho et al., 2018*) and furthermore optimize compartment predictions for yet unassigned proteins. Using data-dependent acquisition (DDA), we detected 3602 partial protein profiles and 2971 complete profiles which is about 55% of the yeast proteome (*Ho et al., 2018*).

Next, we used SVM analysis to assign profiled proteins to a defined organelle, which is incorporated in the DOM-ABC web app. Initially, Sebastian Schuck created a combined reference database based on information in the Saccharomyces Genome Database and localization studies (*Breker et al., 2013; Kraus et al., 2017; Ho et al., 2018*). The reference database contains information about roughly all 5400 proteins in yeast and their main subcellular localization in equilibrium. Then Sebastian Schuck generated a marker list using the SVM module to define a set of proteins which were consistently assigned to the same organelle annotated in the reference database. The marker list of 1908 proteins combined inseparable organelles such as ERGIC, COPI, COPII with Golgi, omitted cytoskeleton proteins and proteins with dual localizations. This resulted in 12 defined compartments: nucleus, cytosol, mitochondria, vacuole and endosomes, plasma membrane (PM) and cell wall, Golgi, ER, ribosome, nuclear envelope (NE), proteasome, lipid droplet, peroxisome. The PCA plot of the combined reference maps showed distinct clusters of the defined marker categories (Figure 4A). This verified that DOM is suited to consistently analyze protein subcellular localization in yeast.

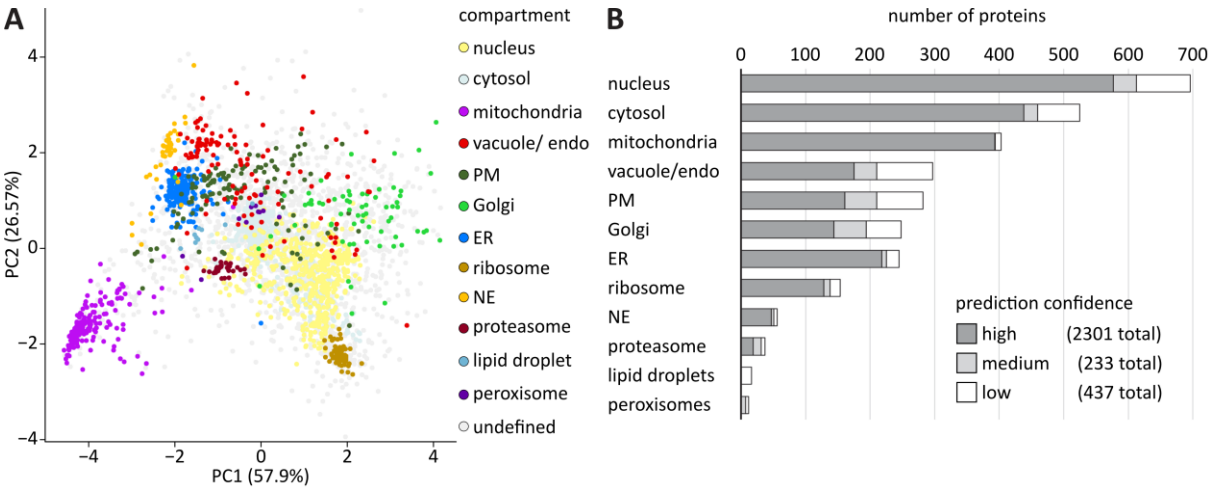

Figure 4: Proteins were assigned to distinct organelles in the reference map. (A) Principal components analysis (PCA) plot of untreated WT cells visualize the reference maps. 6 organellar maps of WT control cells were combined and PCA performed.

Pre-defined marker proteins form distinct clusters, all unassigned proteins are labeled as “undefined”. **(B)** Reference maps compartment predictions of all 2971 complete profiles proteins. Displayed are numbers of proteins assigned to a respective organelle with high, medium and low confidence. PCA in (A) was performed and plotted by me. Graph in (B) was adapted from (*Platzek et al., 2025*).

The SVM model was first trained with the marker list and then applied to the reference maps and predicted the localization of 2971 profiled proteins (Figure 4B). Localization of about one third of proteins did not agree with the reference database because the compartment classifiers of 418 proteins shuttling between two compartments or unknown, were not present in the marker list. Additionally, 578 proteins with both big membrane and cytosolic pools could not be assigned to only one organelle. After adding the classifier “cytosol” to these, the predicted localization by SVMs agreed with 89% of those in the reference database. Despite the limitation to assign proteins to only one classified organelle, SVM localization predictions support interpretation of predicted protein shifts.

3.3 ER stress maps

The extent to which the ER and other organelles are affected by ER stress and how they respond by organellar remodeling have mainly been explored by microscopy of fluorescently tagged proteins. Thus, I applied DOMs to identify global protein localization changes of native proteins and refine stress response pathways.

I generated triplicate maps of control, DTT and Tm treated cells (Figure 5A). Across the 9 maps we detected 3424 protein profiles of which 2607 were mapped consistently. Analysis of the full proteomes revealed that upon stress known proteins which corresponded to genes targeted by an active UPR (*Schmidt et al., 2019*) were upregulated (Figure 5B). These included ER-resident chaperones to enhance protein folding, modification and degradation and ER import and export machinery, verifying the induction of ER stress under my conditions. Out of the 1343 and 1137 differentially regulated proteins in DTT and Tm, respectively, 847 were upregulated in both conditions to same extents (Figure 5C). Since about one third of the measured proteome is differentially regulated by both treatments, we concluded that the treatments induced major proteome remodeling. Gene ontology (GO) term enrichment analysis of all 2607 proteins confirmed that both stressors upregulated similar pathways for protein quality control and degradation and downregulated similar pathways responsible for ribosome biogenesis and translation (*Travers et al., 2000; Steffen et al., 2012*) (Figure 5D). Interestingly, DTT downregulated mitochondrial proteins responsible for organelle integrity

and respiratory function, whereas Tm induced slight upregulation of these proteins, verifying the different modes of action of the stressors.

In conclusion, the protein abundance changes demonstrated that both ER stressors induce global proteome remodeling of pathways involved in the secretory pathway and degradation but also act differently on some organelles such as mitochondria.

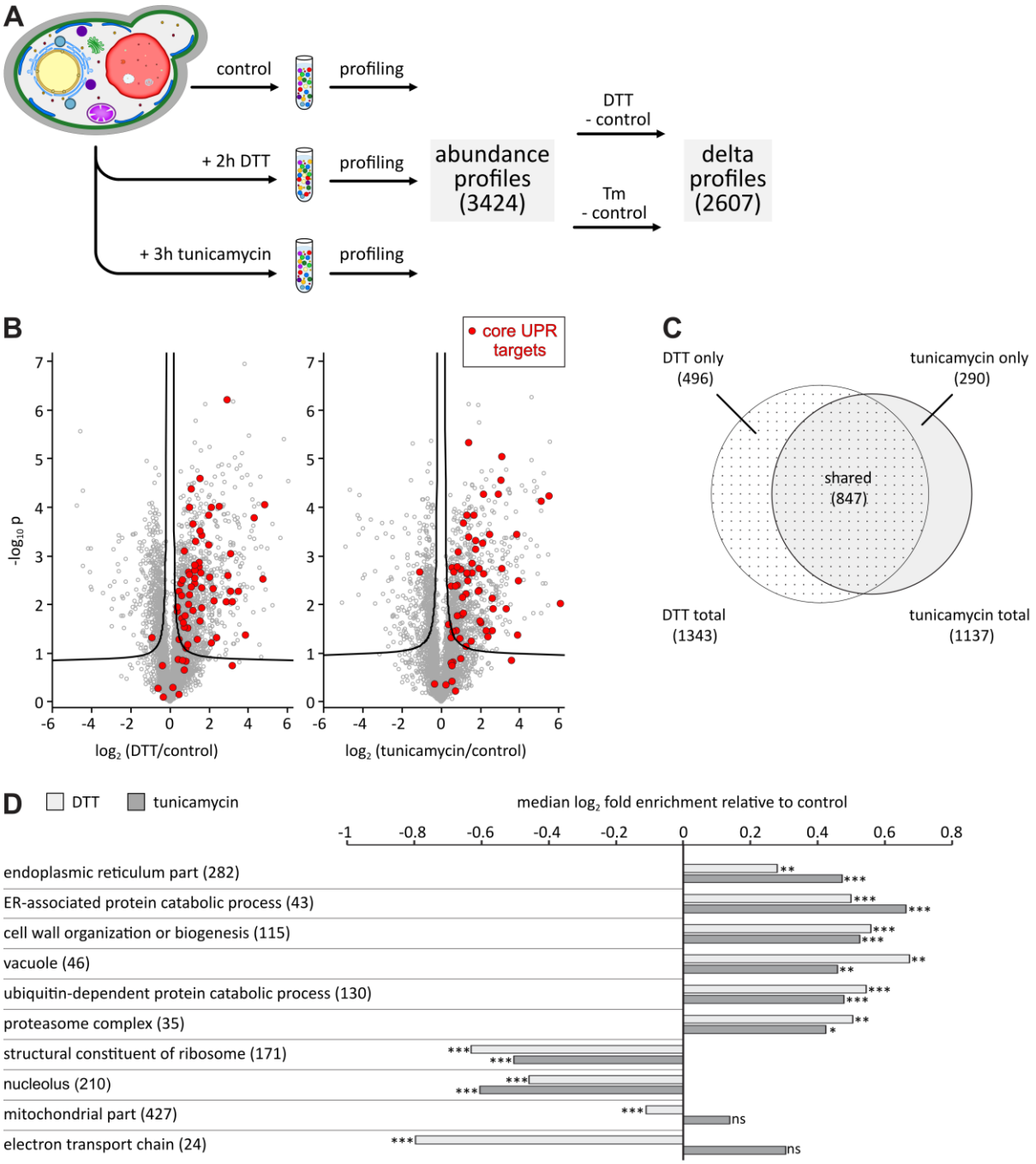

Figure 5: ER stress induces protein abundance changes. (A) Workflow of dynamic organellar mapping for ER stress. Cells were treated as indicated and subjected to subcellular fractionation and mass spectrometry profiling. The quality filtered dataset contained 3424 abundance profiles, after filtering for complete profiles over all 9 maps, 2607 profiles were used for subsequent data analysis. **(B)** Volcano plots of full proteomes of DTT and Tm treated cells. Plotted are the log_2 fold abundance changes upon ER stress against their respective significance value (p-value), determined with a two-tailed t-test. Volcano lines

mark 5% FDR cut-offs based on data permutation. Highlighted in red are proteins upregulated by the UPR. **(C)** Venn diagram of differentially regulated proteins upon DTT and Tm treatment. **(D)** Gene ontology enrichment analysis of full proteomes of DTT or Tm treated cells compared to their respective control. Selected terms show shared up- or downregulation in both strains. The number of proteins assigned to each term is indicated in brackets. Significant enrichment of terms is labeled as follows: ns, not significant; *, p<0.05; **, p<0.01; ***, p<0.001. (A), (B), (C), (D) were adapted from (*Platzek et al., 2025*).

To evaluate the utility of the ER stress maps, I performed PCA on the averaged triplicate maps of each condition and plotted the results (Figure 6A). The control map showed distinct compartment clusters, which shifted throughout the map upon ER stress. Especially the ER and nuclear envelope (NE) cluster largely shifted upon DTT and to a minor extent upon Tm. The ribosomal cluster did not shift upon ER stress.

Next, we identified proteins which significantly changed their protein localization. Therefore, we used the Movement Reproducibility (MR) analysis incorporated in the DOM-ABC web app. The DOM-ABC web app applied an additional quality filter to reduce noise of less reproducible replicates before it performed the MR analysis. Hence, roughly 2300 complete protein profiles were analyzed to detect significant shifts (Figure 6B).

410 and 149 proteins were predicted to significantly change their localization upon DTT and Tm, respectively. These are referred to as ER stress hits. As their median $\log_2$ abundance change is only 0.23, this suggests that the predicted hits were mainly spatially regulated and not transcriptionally. Moreover, this confirmed previous findings that DTT induced more prominent organellar remodeling (*Schuck et al., 2009*), even though the total proteome abundance changes between DTT and Tm were nearly equal. Assumingly, more proteins accumulated in the ER upon DTT treatment, resulting in ER expansion and dilation causing potentially denser microsomes and hence altered sedimentation behavior.

The localization of the hits were annotated based on the reference database. In cells in equilibrium (control map), almost half of the mapped proteins were part of the cytosol and the nucleus, as opposed to only 9% and 12% of the mapped DTT and Tm hits, respectively. But ER and NE proteins were nearly 6-fold overrepresented in DTT hits, but not Tm hits. Together with proteins of post-ER compartments they constitute almost 70% of all DTT hits (Figure 6C).

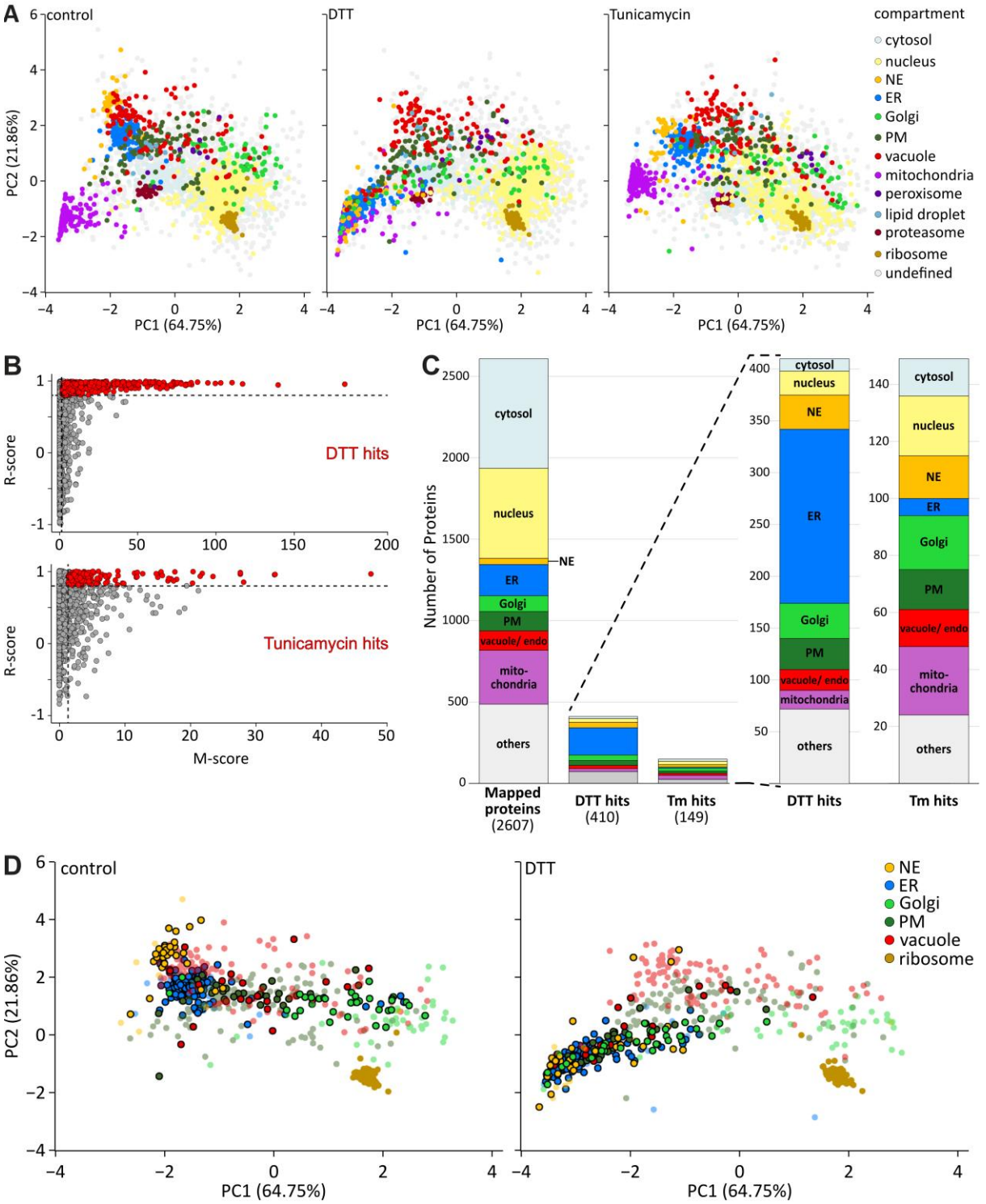

Figure 6: Protein localization changes upon ER stress. (A) PCA plots of control, DTT and Tm treated cells. Plots show averaged biological triplicates of 6-point profiles. Defined marker proteins are displayed in color; all other proteins are annotated as "undefined". Upon ER stress the ER cluster and NE cluster showed the strongest shifts. **(B)** Detection of significant shifting proteins upon ER stress. Cutoffs were defined as movement (M) score >1.3, reproducibility (R) score >0.8, FDR <5% and hits are highlighted in red. **(C)** Bar graphs showing reference database annotated localization of all proteins mapped across 9 maps (left), the 410 DTT MR hits (middle) and the 149 Tm MR hits (right). ER, nuclear envelope, Golgi and plasma membrane proteins are overrepresented in the DTT hits compared to all mapped proteins, whereas nucleus and cytosol are underrepresented. Nuclear envelope, Golgi, plasma membrane and mitochondria proteins are overrepresented in Tm hits, compared to all mapped proteins whereas cytosol and ER are underrepresented. **(D)** Control and DTT PCA plots from (A).

Highlighted are selected DTT hits of the indicated organelles from the MR analysis. Proteins of the same organelles which did not shift are transparently displayed. The non-shifting ribosome cluster is shown as reference. PCA in (A) and (D) were performed and plotted by me. MR plot in (B) was adapted from (*Platzek et al., 2025*). Bar graph in (C) was generated by me.

This tendency of DTT-induced organellar remodeling was already apparent when closely examining the PCA plots and highlighting the respective compartments and hits (Figure 6D). In contrast to the ribosome cluster, almost all analyzed ER (171 out of 183) and NE (34 out of 38) proteins shifted, leading to a shift of the whole clusters across the DTT map. Proteins of the post-ER compartments shifted more selectively: Golgi (33 out of 89), plasma membrane (30 out of 123) and vacuole (20 out of 112). These hits shifted together with the ER cluster, whereas the non-shifting proteins maintained their position on the map.

Lastly, Tm affected relocalization of more mitochondrial proteins, suggesting that not only the extent but also the mode of action of Tm-induced stress on organelles besides the ER was different.

Consequently, using SVM analysis, cytosolic shift analysis and organellar shift analysis (shifting with the ER), Georg Borner and Sebastian Schuck were able to assign the localization after DTT-induced organellar remodeling to the hits and thus predicted the direction of the shifts. They grouped the defined shifts into seven distinct classes, summarized visually in Figure 7: 169 ER proteins shifting within the entire organelle; 89 proteins shifting towards the ER, of which 82 derived from a compartment of the secretory pathway; 12 ER proteins shifting towards the cytosol; 22 proteins of the nuclear envelope (NE) including 14 nuclear pore complex (NPC) components shifting within the entire NE; 17 proteins shifting away from the NE, of which 13 shift from the NPC towards the cytosol; 7 mitochondrial proteins shifting away, of which 6 shift towards the cytosol. 94 shifts of other affected organelles or unclear shift directions could not be classified in the above groups.

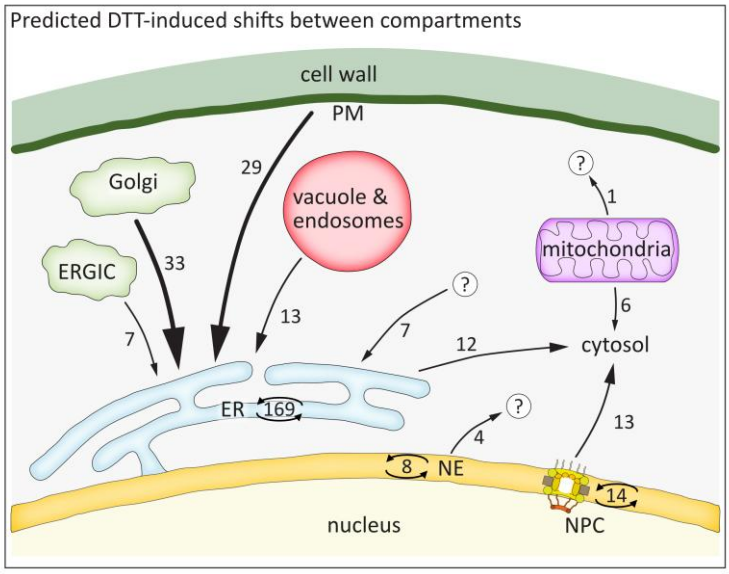

Figure 7: Scheme of predicted DTT-induced shifts between compartments. Classification of predicted DTT hits between and within organelles are displayed. 94 shifts could not be classified into the categories shown. Scheme was adapted from (*Platzek et al., 2025*) and modified by me.

3.4 Validation of ER stress induced protein localization changes

To confirm the legitimacy of the predicted hits and shift categories, I used the cytosolic terminus tagged mNeonGreen (mNG-I) library to microscopically assess changes in localization upon stress (*Meurer et al., 2018*). Since the library is based on another background strain BY4741, I optimized ER stress conditions to induce similar phenotypes as in my W303 strain (Figure 8). I included Tm treatment to validate the differences and whether the effect of DTT was visibly greater on organellar remodeling.

Yeast cells of both strain backgrounds expressing the ER marker proteins, mCherry-Ubc6 or Sec63-mNeonGreen (-neon), showed normal discontinuous ER signal under equilibrium conditions. Upon DTT and Tm treatment, the ER signal becomes continuous and even expands into the cytosol, indicating ER expansion (*Bernales et al., 2006*). Moreover, endogenous expressed Prc1-neon, showed a moderate ER signal after the indicated treatments (Figure 8A, Merge). In both strain backgrounds the ER signal of Tm-stressed cells was very weak. I continued with the respective conditions and manually imaged 79 mNG-I library strains.

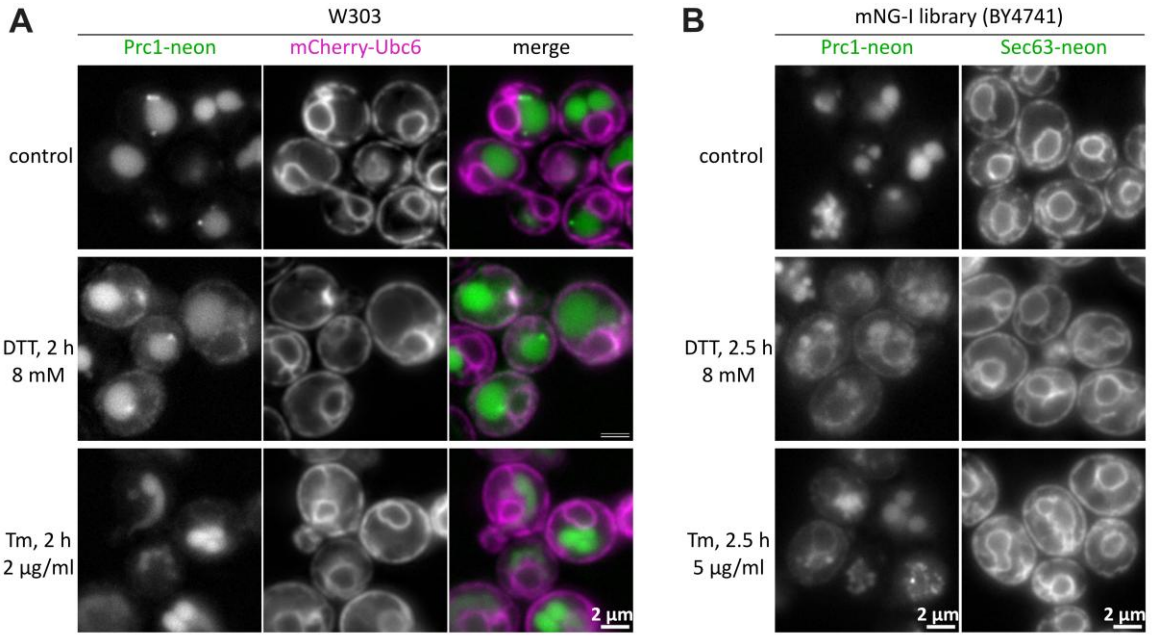

Figure 8: ER stress affects different strain backgrounds similarly. (A) Widefield fluorescence images of W303 yeast cells expressing lumenal vacuole protease Prc1-mNeonGreen (-neon) and ER marker mCherry-Ubc6 untreated, after 2 h of DTT or Tm treatment. The Prc1-neon signal overlaps visibly with the ER marker signal upon DTT treatment. **(B)** Widefield fluorescence images of BY4741 yeast cells expressing lumenal vacuole protease Prc1-neon or the ER marker Sec63-neon untreated, after 2.5 h of DTT or Tm treatment. The Prc1-neon signal is visible in vacuoles and in the ER upon ER stress. Ideal display ranges for each channel are shown for better visualization of the phenotype. Experiments were conceptualized, performed and arranged by me.

Additionally, I fluorescently tagged proteins in W303 which were not present in the library or where the tag interfered with correct localization and function. These were lumenal ER proteins, glycosylphosphatidylinositol (GPI) -anchored proteins and tail-anchored proteins. I designed and placed the fluorescent tag in a way to maintain signal sequences for correct translocation into the ER and to keep membrane domains intact. I used the rapidly maturing and more stable superfolder green fluorescent protein (sfGFP) to enhance visualization when the protein resided in the oxidizing ER lumen or was exported from the ER (*Pédelacq et al., 2006*).

Indeed, most Tm-induced phenotypes were less severe, confirming the lower numbers of significantly shifting proteins predicted by MR analysis.

Thus, I proceeded with tagging and imaging of manually selected hits in the W303 strain background. I only analyzed untreated and DTT-stressed cells and classified the localization changes in Table 1.

Table 1: Summary of ER stress hits with predicted shifts between compartments. Displayed are all proteins imaged using the mNeonGreen-I library. Proteins in bold were affected by ER stress and showed a change in their phenotype, the asterisk * indicates proteins that were further tagged in W303 and imaged, proteins in brackets were not predicted to shift significantly in the MR analysis but were still imaged. Table was adapted from (*Platzek et al., 2025*) and modified by me.

shift prediction	original compartment	end compartment	proteins	description
away from ER	ER membrane	cytosol	**Dpm1***, **Rtn1***, **Yop1***	Rtn1 puncta
	ER lumen	cytosol	**Cpr5***, **Fpr2**, **Kar2***, **Pdi1***, **Sil1***	ER reflux
	ER periphery	diverse	**Scs2***, (**Ypp1**)*	ER-PM contact site
	ER & cytosol	cytosol	**Get3***, (**Nus1**), Cdc48*, Djp1	diverse proteins
towards ER	ERGIC	ER	(**Emp46**), Erv41	ER-to-Golgi transport
	Golgi	ER	**Mnl2***	mannosidase
	Golgi	ER	**Kre2***, **Mnn2***, **Mnn5***, Och1*	mannosyl-transferases
	plasma membrane, cell wall	ER	Dfg5, **Gas1***, **Gas3** *, **Toh1***, (**Utr2**)*	GPI-AP
			Scw10, Scw4	soluble cell wall protein
	vacuole, endosome	ER	**Atg42***, Ecm14, Ecm38, **Pep1***, **Pep4**, Ppn1, **Prc1***, Vth1/2 (low signal)	CPY pathway
away from Golgi	Golgi	cytosol	Apl5, (Apl6), (Vps45)	ALP pathway, vesicle fusion
accumulation at vacuole	vacuole	vacuole	**Kog1**, **Lst8***, Tor1	TORC1
			Vps27	endosomal protein sorting
away from NE	NE	cytosol	**Dyn2*, Gle1*, Gle2***, Nup100***, Nup116*, Nup159*, Nsp1*, Nup82*, Nic96*, Nup188*, Nup192*, (Nup42)*, Nup49*, Nup57***	nucleoporins
			Kap95*, **Kap120***, **Mex67***, **Srp1***	nucleocytoplasmic transport

with NE	NE	NE	Ndc1*, Pom152*, Pom34*, Nup84*, Nup85*, Nup120*, Nup133*, Nup145* Nup170*, Nup157*, Nup53*, Asm4*, Mlp2*, (Mlp1)*, Nup1*, Nup2*, Nup60*	nucleoporins
away from mitochondria	mitochondria	ER & cytosol	**Ccp1**, **Mcr1**, Tim10 (low signal), Tim13 (low signal), Cyc1, Msp1	diverse proteins
away from original compartment	diverse	diverse	Nud1, **Mtc1**, Pfk1, Pfk2	diverse proteins

3.4.1 ER proteins moving towards the cytosol

Among the 12 proteins shifting from the ER towards the cytosol, were the unexpected integral membrane proteins Rtn1, Yop1 and the tail-anchored mannosyltransferase Dpm1. Rtn1 and Yop1 are ER membrane shaping proteins comprising a reticulon homology domain (*Voeltz et al., 2006*) and they interact with themselves and with Dpm1 (*Mast et al., 2016*). Neighborhood analysis revealed that their abundance profiles correlated highly in all conditions and they clustered tightly in the PCA plot (Figure 9A). All three proteins increased their cytosolic pools after stress (15-19% increase), but their correlation with the average ER markers decreased by 10% compared to other hits (data not shown). This prediction was in concordance with (*Papagiannidis et al., 2021; Wang et al., 2023*), who showed that Rtn1 in budding yeast and Yop1 in fission yeast separated from the ER and accumulated in cytosolic clusters.

In fact, microscopy analysis showed a colocalization of Rtn1, Yop1 and Dpm1 and a clear separation of these proteins from the ER, forming potentially clusters in the cytosol (Figure 9B). To what extent the stress-induced clusters remain attached to the ER or detach completely and how these membrane proteins were extracted from the ER upon stress, remains to be investigated. Nevertheless, DOMs correctly identified components of a new ER derived structure.

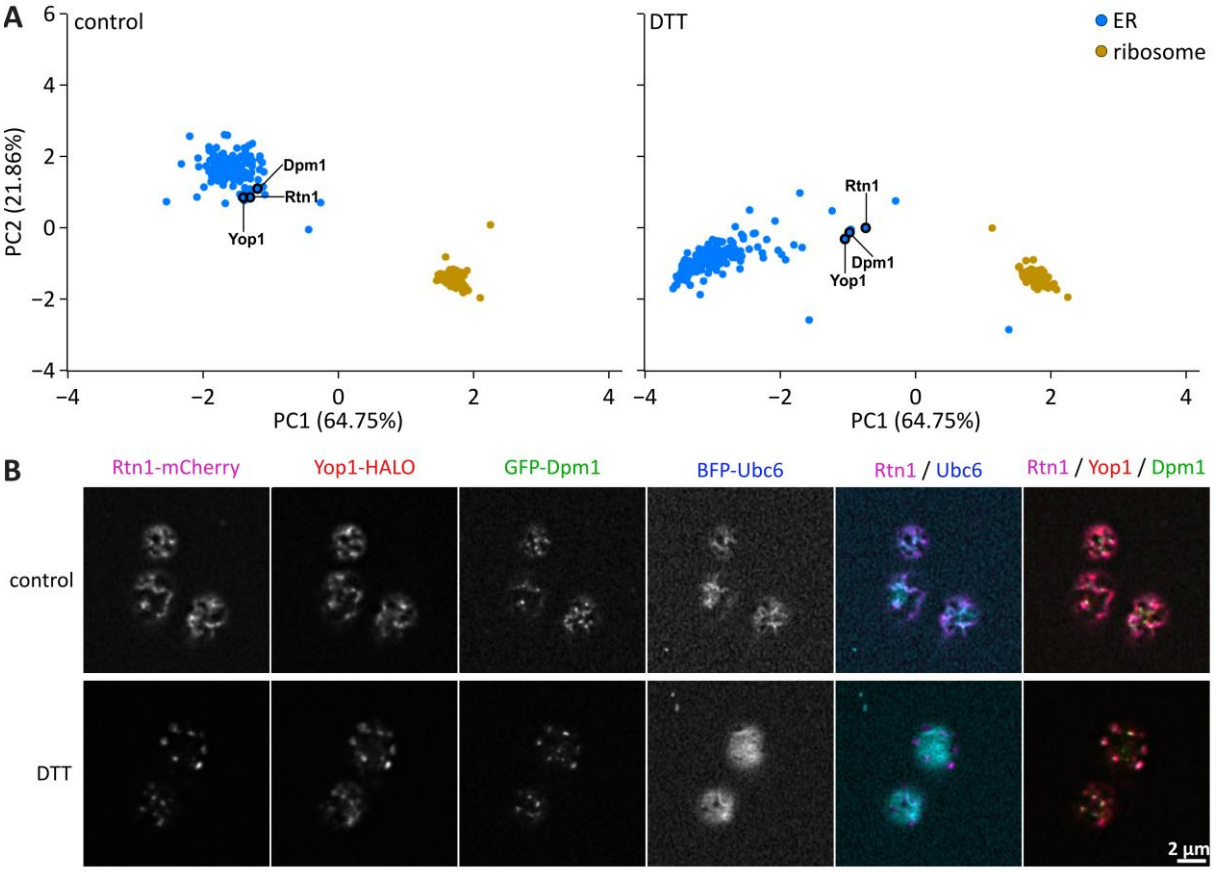

Figure 9: Reticulon proteins cluster tightly and relocalize into the cytosol upon stress. (A) PCA plots of control and DTT organellar maps. Rtn1, Yop1, Dpm1 are clustering and shift away from the ER cluster upon DTT treatment. The non-shifting ribosome cluster is shown as reference. **(B)** Deconvolved confocal microscopy images of cortical sections of cells expressing endogenous Rtn1-mCherry, Yop1-Halo and promoter driven GFP-Dpm1 and the ER marker BFP-Ubc6 untreated or upon 2 h DTT treatment. Rtn1, Yop1 and Dpm1 colocalize in both conditions. Ideal display ranges for each channel are shown for better visualization of the phenotype. PCA in (A) was performed and plotted by me. Microscopy images in (B) were acquired by Klára Odehnalová and arranged by me.

The other interesting class of proteins shifting from the ER towards the cytosol were the five soluble lumenal ER proteins, Cpr5, Fpr2, Pdi1, Sil1 and Kar2. All of these are chaperones or co-chaperones and enhance folding of newly translocated polypeptide chains inside the ER lumen. Upon ER stress but independent of ERAD or UPR, correctly folded lumenal ER proteins relocalize into the cytosol. This process is called ER reflux and has been studied mainly with artificial ER localized reporters, but it was also shown for endogenous Cpr5 and Pdi1 (*Igbaria et al., 2019*). By analyzing the cytosolic pool for all 19 lumenal ER proteins, the five MR hits mentioned above had the most striking increase in their cytosolic pool upon ER stress. Only four other chaperones and co-chaperones increased their cytosolic pool, whereas the remaining 10 did not have a detectable cytosolic pool (Figure 10A). I confirmed by microscopy that the known ER reflux cargos Pdi1 and Cpr5 relocalize back into the cytosol (data not shown) and that Sil1 is in fact a new ER reflux cargo (Figure 10B). This was also true for Fpr2

and Kar2 (data not shown). In contrast, Ero1, which did not have a cytosolic pool, stayed exclusively in the ER. During ER stress the protein levels of Ero1 increased about 8-fold as opposed to Pdi1 (3-fold) or Cpr5 (1.2-fold), suggesting that there was no defect in Ero1 import into the ER, hence the ER stayed intact during fractionation.

These results demonstrated that ER reflux is a selective process which involves more ER resident chaperones than previously known.

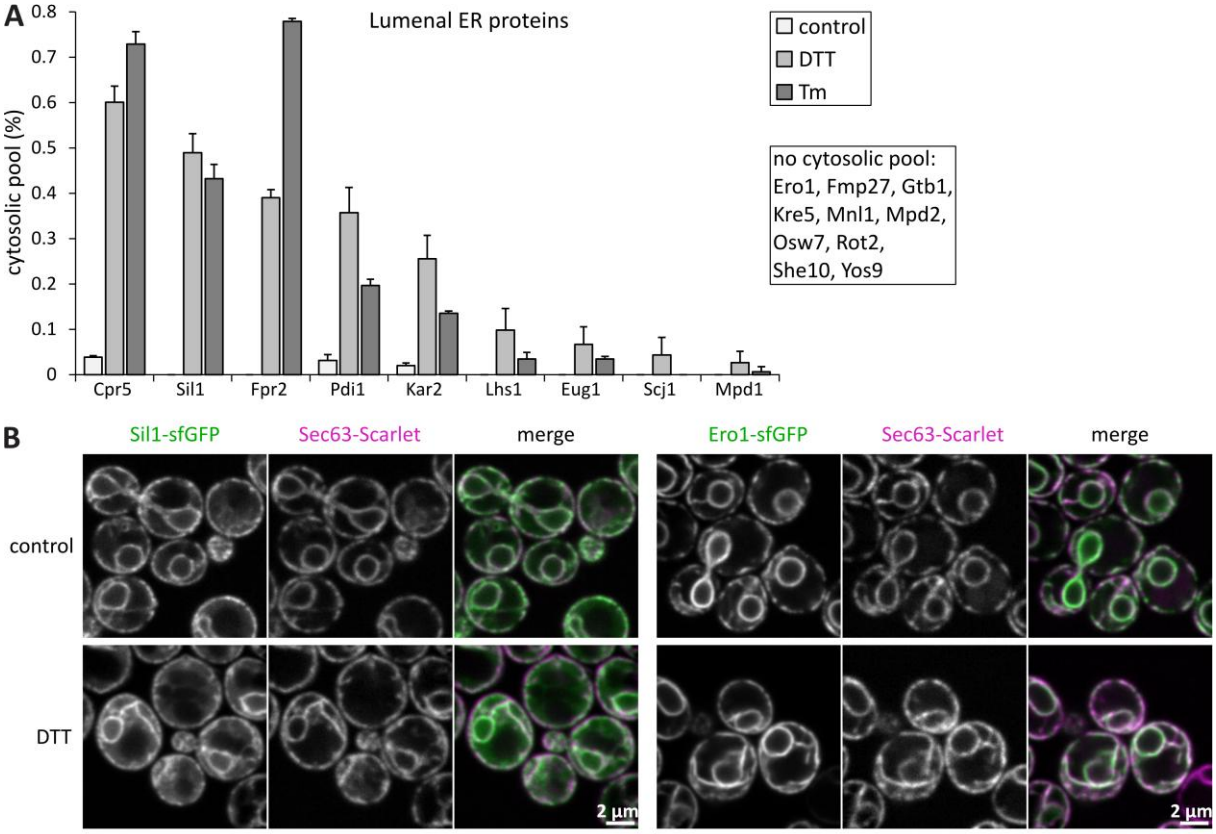

Figure 10: Selective ER reflux of lumenal ER proteins. (A) Bar graphs display the mean cytosolic pools of lumenal ER proteins in control, DTT and Tm-treated cells (n=3). Error bars show standard deviations. (B) Confocal fluorescence microscopy images of cells expressing Sil1-sfGFP or Ero1-sfGFP together with the ER marker Sec63-Scarlet untreated or after DTT treatment. Sil1 but not Ero1 shows additional cytosolic signal upon DTT treatment. Ideal display ranges for each channel are shown for better visualization of the phenotype. Bar graph in (A) was adapted from (*Platzek et al., 2025*). Experiment in (B) was conceptualized, performed and arranged by me.

Lastly, I also analyzed Get3, the cytosolic subunit of the GET complex, which binds the transmembrane domain of tail-anchored proteins in the cytosol and guides them to the ER membrane, where Get1/ Get2 heterodimer inserts them in into the membrane (*Schuldiner et al., 2008*). Get3 was predicted to further shift towards the cytosol, which I confirmed by microscopy. Upon ER stress Get3 forms cytosolic puncta which did not colocalize with Cdc48 (data not shown), suggesting that puncta formation occurs independent of the ERAD pathway. This phenotype was already described by (*Ulrich et al., 2022*) who showed that upon redox stress induced by H_2O_2, Get3 rapidly forms cytosolic puncta which dissolved during recovery.

Thus, DOMs was not only able to identify major cytosolic shifts but also identified the subtle relocalization towards the cytosol of a protein with dual localization, proving that it is a very sensitive method.

3.4.2 Retention of proteins in the ER

The most striking localization changes demonstrated the whole ER cluster together with selected proteins of other post-ER compartments (Figure 6D). For decades it has been common knowledge that proteins need to fold correctly and become glycosylated in order to be exported from the ER (*Lodish, 1988; Doms et al., 1988*). Since DTT and Tm induced misfolding of newly synthesized proteins, we expected to see an accumulation of non-ER resident proteins in the ER which could not be exported anymore. To discover proteins which are likely to shift towards the ER during stress, Georg Borner performed organelle shift analysis with all proteins known to be localizing to post-ER compartments and which were identified as significant shifting in the MR analysis. Each abundance profile was compared to the average ER marker profiles and the correlation calculated. Single profiles which aligned more than 75% with the average ER profile after ER stress were annotated as hits (Figure 11A).

There were 89 proteins which met the criteria, originally derived from ERGIC (7), Golgi (33), vacuole and endosomes (13) and plasma membrane and cell wall (29). The original compartment of seven hits could not be determined (Consequently, using SVM analysis, cytosolic shift analysis and organellar shift analysis (shifting with the ER), Georg Borner and Sebastian Schuck were able to assign the localization after DTT-induced organellar remodeling to the hits and thus predicted the direction of the shifts. They grouped the defined shifts into seven distinct classes, summarized visually in Figure 7: 169 ER proteins shifting within the entire organelle; 89 proteins shifting towards the ER, of which 82 derived from a compartment of the secretory pathway; 12 ER proteins shifting towards the cytosol; 22 proteins of the nuclear envelope (NE) including 14 nuclear pore complex (NPC) components shifting within the entire NE; 17 proteins shifting away from the NE, of which 13 shift from the NPC towards the cytosol; 7 mitochondrial proteins shifting away, of which 6 shift towards the cytosol. 94 shifts of other affected organelles or unclear shift directions could not be classified in the above groups.

Figure 7).

In the DTT maps, 465 proteins belong to a post-ER compartment of which 243 contain a transmembrane domain or a signal sequence, which targets them to the ER. The fact that only 86 of these were predicted to shift towards the ER, implies that only specific proteins misfolded and bulk flow is generally preserved.

Five soluble lumenal vacuole proteins were identified, which are targeted to the vacuole via the carboxypeptidase Y (CPY) pathway as hits shifting towards the ER upon stress. Besides these known CPY cargos Prc1/ CPY, Atg42, Pep4, Ape3, Ydr415c (*Eising et al., 2022*), also the membrane glycoproteins Vth1 and Vth2 were found as a hit. They present similarities to the known CPY cargo receptor Pep1, which also shifted towards the ER but was classified as Golgi since it shuttles between late-Golgi and endosomes (Figure 11B) (*Cooper and Stevens, 1996*).

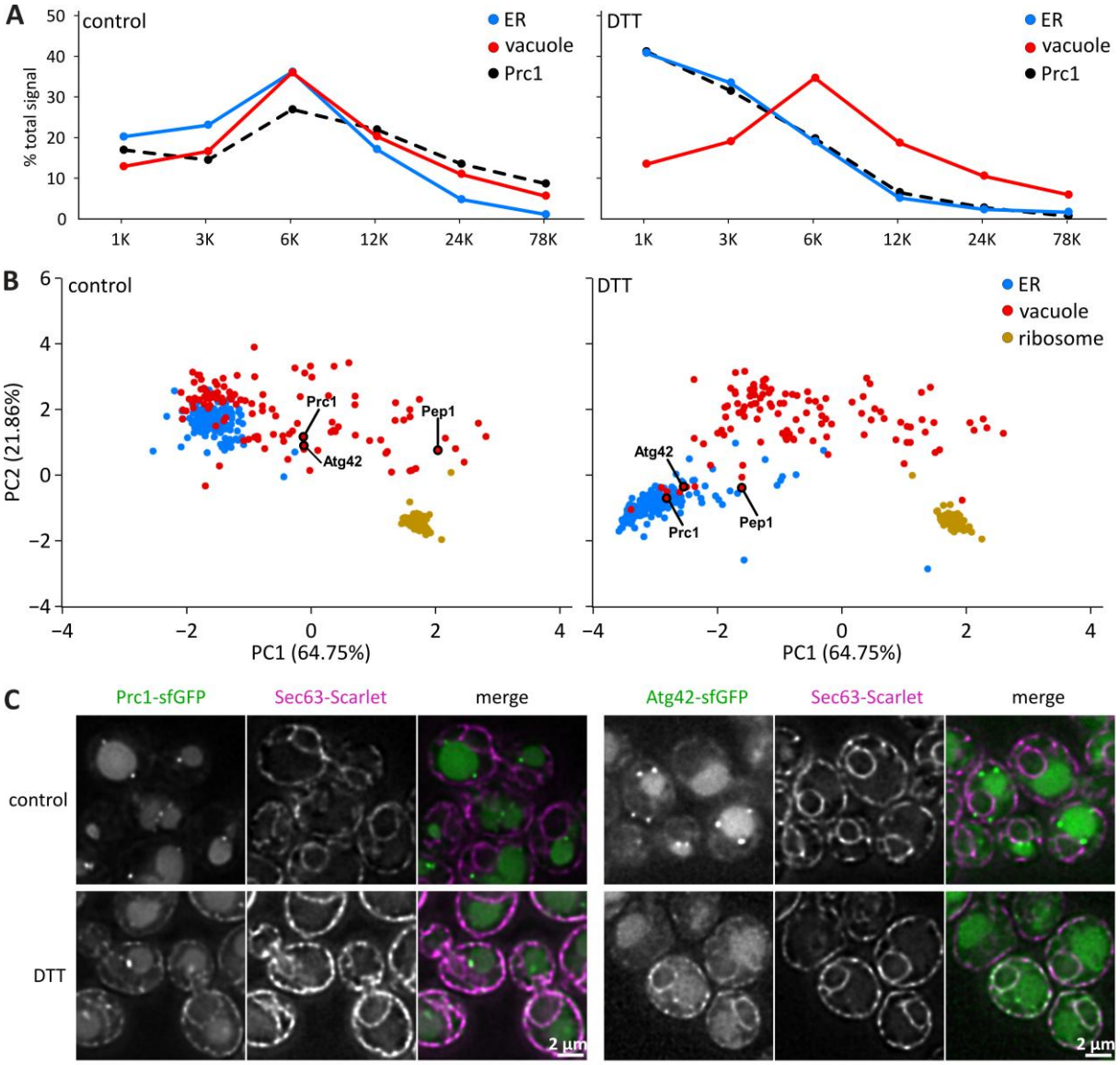

Figure 11: ER retention of proteins of the CPY pathway. (A) Abundance profiles of average ER and vacuole marker proteins and of average Prc1 in control and DTT-treated cells. In control cells the Prc1 profile aligns partially with the vacuole profile but aligns perfectly with the ER profile in DTT-treated cells. **(B)** PCA plots of control and DTT organellar maps. CPY cargos Prc1 and Atg42 together with their receptor Pep1 segregated from the vacuole cluster and shifted towards the ER cluster upon DTT treatment. The non-shifting ribosome cluster is shown as reference. **(C)** Deconvolved widefield microscopy images of cells expressing Prc1-sfGFP or Atg42-sfGFP together with the ER marker Sec63-Scarlet untreated or after 2 h DTT treatment. Both CPY cargos show vacuole, endosome and additional ER signal after DTT treatment. Same display ranges for each channel are shown for better comparison of phenotypes. PCA in (B) was performed and plotted by me. Experiment in (C) was conceptualized, performed and arranged by me.

I performed microscopy experiments and confirmed ER retention of both the CPY cargos Prc1, Atg42, Pep4 (only mNG-I library, data not shown) and Pep1 (data not shown), since all showed a strong ER signal after DTT treatment (Figure 11C). This phenotype is most likely due to misfolding of newly synthesized vacuole proteins of the CPY pathway, which are retained in the ER and cannot be targeted to the vacuole. ER retention of vacuolar proteins was exclusive for CPY pathway cargos and receptors, since cargos or components of neither the ALP

pathway, nor Vps45 mediated membrane fusion were predicted to significantly change their localization (*Eising et al., 2022*). The previously imaged strains of the mNG-I library verified that the latter pathways were not affected by ER stress (Table 1).

33 Golgi and ERGIC proteins shift towards the ER out of 74 analyzed in the DTT maps. Among these were 19 mannosyltransferases (*Fabre et al., 2014*) and 7 components of COPII-mediated vesicle transport, which shifted significantly unlike other Golgi proteins, such as the phosphoinositol transferase Aur1 which is involved in sphingolipid synthesis (Figure 12A). I verified these predictions by microscopy and showed that Kre2, Mnn2 (data not shown) and Mnn5 but not Aur1 substantially relocalized from the Golgi towards the ER upon DTT treatment (Figure 12B). Additionally, the mannosidase Mnl2 has been annotated as ER localized, however DOMs predicted it to be a Golgi protein which shift towards the ER, which I confirmed by microscopy (data not shown). If this subset of Golgi proteins accumulated in the ER because of misfolding or enhanced recycling of Golgi proteins by retrograde transport via COPI, remains to be investigated (*Todorow et al., 2000*).

Since glycosylating and cargo export in COPII vesicles were affected by ER stress, I also discovered that of the 29 relocalizing plasma membrane and cell wall proteins, 11 GPI-anchored proteins (GPI-APs) were detected (Figure 12C) (*Hamada et al., 1998*). GPI-anchors are synthesized in the inner leaflet of the ER membrane and then transferred to the C-terminus of correctly folded lumenal proteins, where the GPI-anchor is again remodeled. Correctly folded and remodeled GPI-APs concentrate at ER exit-sites, bind p24 family cargo receptors and are finally exported in COPII vesicles. (*Castillon et al., 2009; Muniz and Riezman, 2016*).
Microscopy revealed that for all imaged GPI-APs a strong ER signal was observed, confirming ER retention (Figure 12D). Even the GPI-AP Utr2, which narrowly failed to be a MR hit because of its R-score, was retained upon ER stress. 12 out of 13 DTT-mapped GPI-APs were found to significantly relocalize towards the ER, verifying that especially GPI-APs are massively affected by ER stress.

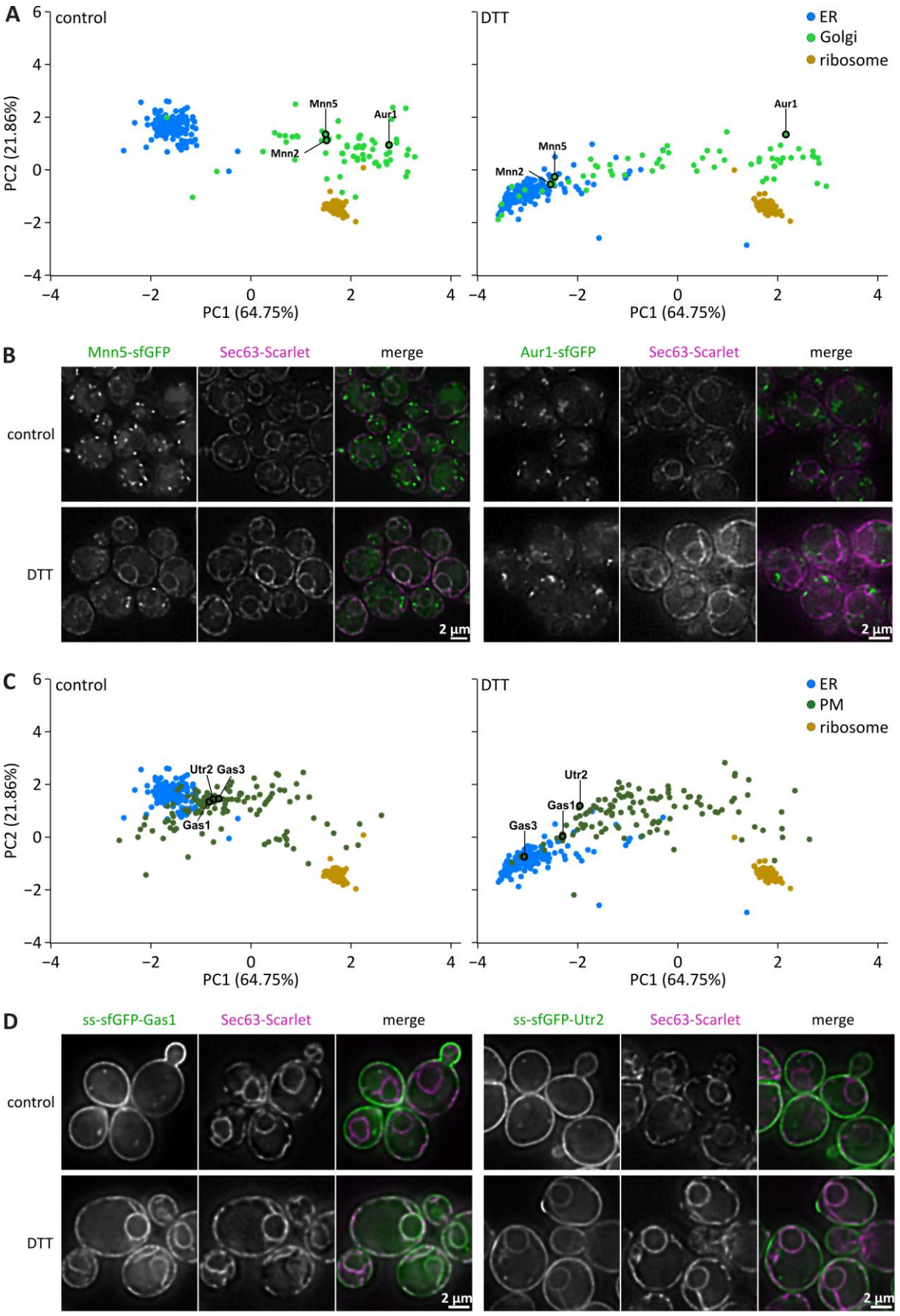

Figure 12: Golgi mannosyltransferases and GPI-anchored proteins are retained in the ER upon ER stress. (A) PCA plots of control and DTT organellar maps. Mannosyltransferases Mnn2 and Mnn5 but not the phosphoinositol transferase Aur1 segregated from the Golgi cluster and shifted towards the ER cluster upon DTT treatment. The non-shifting ribosome cluster

is shown as reference. **(B)** Deconvolved widefield microscopy images of cells expressing Mnn5-sfGFP or Aur1-sfGFP together with the ER marker Sec63-Scarlet untreated or after 2 h DTT treatment. **(C)** PCA plots of control and DTT organellar maps. GPI-APs Gas1, Gas3 and Utr2 segregated from the plasma membrane cluster and shifted towards the ER cluster upon DTT treatment. The non-shifting ribosome cluster is shown as reference. **(D)** Deconvolved widefield microscopy images of cells expressing signal sequence (ss)-sfGFP-Gas1 or ss-sfGFP-Utr2 under the estradiol inducible *GAL* promoter together with the ER marker Sec63-Scarlet untreated or after 2 h DTT treatment. Expression was induced for 16h with 50 mM estradiol prior to the treatment. Artificial Kar2ss was used for ER targeting. For (B) and (D) same display ranges for each channel are shown for better comparison of phenotypes. PCA plots in (A) and (C) were performed and plotted by me. Experiments in (B) and (D) were conceptualized, performed and arranged by me.

All in all, by using DOMs we were able to correctly predict native localization changes upon ER stress collectively, which had not been observed before when using generically tagged yeast libraries. Moreover, we uncovered selective accumulation of proteins in the ER of a specific subset of secretory pathway proteins. This included lumenal vacuole proteins of the CPY pathway, mannosyltransferases in the Golgi and GPI-APs, which were more likely to misfold and retained or not being exported due to unavailability of cargo receptors for export.

3.4.3 ER stress affects nucleoporins, importins and nuclear import

Surprisingly, DOMs predicted a strong shift of proteins of the nuclear envelope, a class of proteins hitherto unassociated with ER stress. We realized that out of the 39 hits, 25 hits are part of the nuclear pore complex (NPC), called nucleoporins. Among the shifting hits were also three nucleocytoplasmic transport factors, Kap95, Srp1 and Mex67, which were not annotated as nuclear envelope proteins in our reference database. Examining the MR hits labeled in the PCA plot, revealed a segregation of 10 nucleoporins from the nuclear envelope cluster which moved together with the ER (Figure 13A). ER shift analysis categorized these MR hits into two groups: nucleoporins which shift together with the nuclear envelope cluster or away from the nuclear envelope cluster. Moreover, the channel and cytoplasmic filament nucleoporin, Nsp1, qualified as cytosolic shift hit. Imaging of the predicted hits with the mNG library (Table 1) explained this contradictory behavior. Already after 1 h of DTT treatment, NPC subunits of the cytoplasmic filaments, the channel complex as well as 2 linker nucleoporins of the inner ring, formed cytosolic puncta, whereas subunits of the membrane ring, inner ring and nuclear basket did neither change their localization nor form cytosolic puncta (Figure 13B, C) (*Akey et al., 2022; Dultz et al., 2022*).

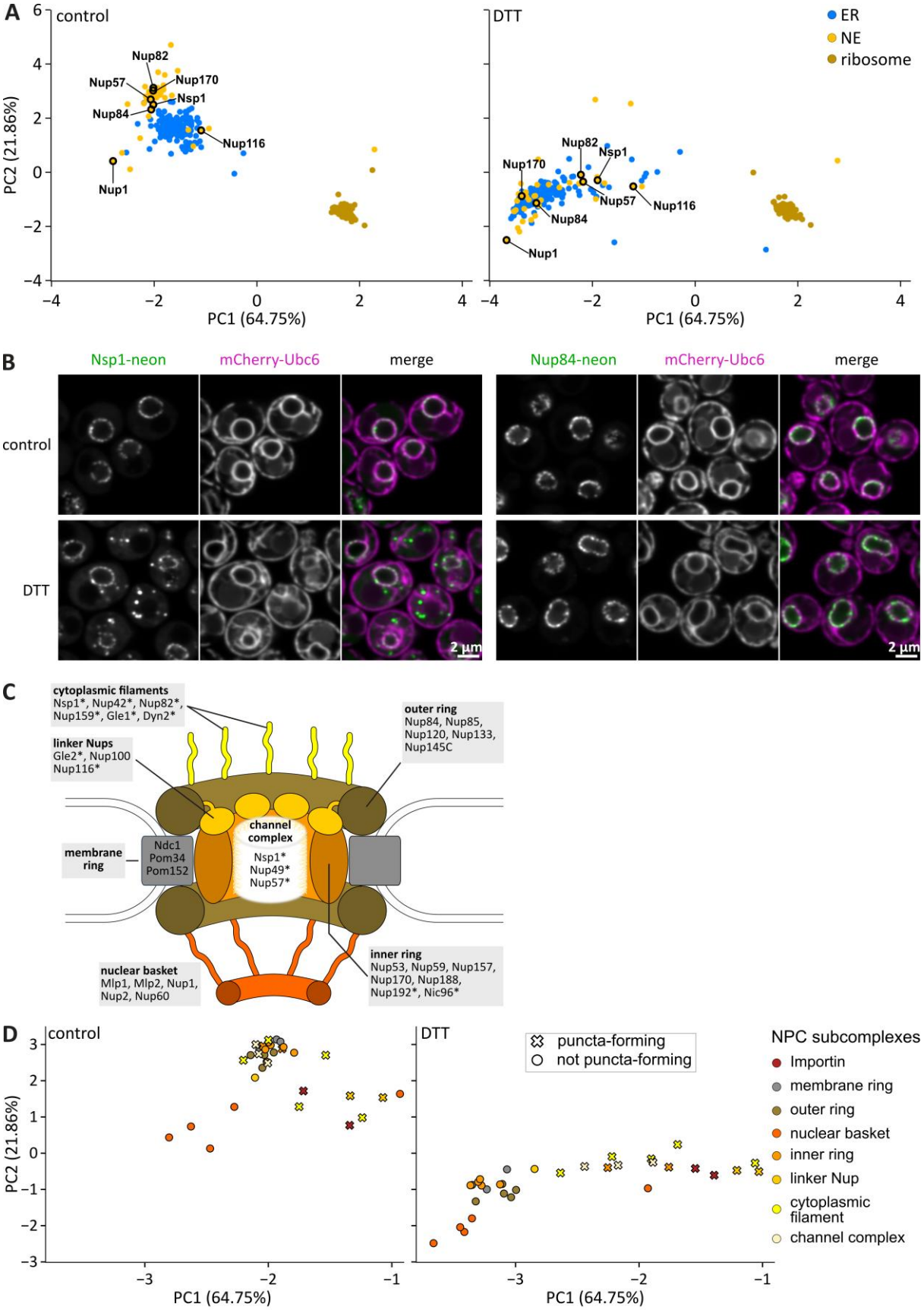

Figure 13: The NPC subcomplexes are contrarily affected by ER stress. (A) PCA plots of control and DTT organellar maps. The nuclear envelope cluster segregated and shifted bidirectionally upon DTT treatment. Selected nucleoporins (Nups) are annotated. The non-shifting ribosome cluster is shown as reference. **(B)** Confocal microscopy images of cells expressing Nsp1-neon or Nup84-neon together with the ER marker mCherry-Ubc6 untreated or after 2 h DTT treatment. Only Nps1 formed

bright cytosolic puncta upon DTT treatment, Nup84 remained unchanged. Same display ranges for each channel are shown for better comparison of phenotypes. **(C)** Scheme of the nuclear pore complex comprising seven subcomplexes. Each subcomplex corresponds to a distinct color. The asterisk indicates nucleoporins that formed cytosolic puncta. **(D)** PCA plots of control and DTT organellar maps showing only nucleoporins and importins. Colors correspond to the different subcomplexes in (B). Components of the subcomplexes shifted as unity, but entire subcomplexes shifted bidirectionally upon DTT treatment and segregated into not puncta-forming or cytosolic puncta forming. PCA in (A) and (D) were performed and plotted by me. Experiment in (B) was conceptualized, performed and arranged by me. (C) was adapted from (*Platzek et al., 2025*) and modified by me.

Next, I tagged and imaged all 31 nucleoporins in W303 and extended the list of nucleoporins demonstrating puncta-formation. I annotated the imaged nucleoporins in the PCA plot as puncta-forming and non-puncta forming and assigned the respective subunit to each datapoint (Figure 13D). First, this revealed that the components of each subcomplex rather shifted uniformly. Subcomplexes which have access to the cytoplasm separated from the membrane associated nucleoporins, which shifted more towards the ER cluster (Figure 13A, Nup1, Nup84, Nup170). Secondly, nucleoporins which shifted away from the nuclear envelope and ER cluster formed cytosolic puncta upon DTT treatment, whereas the others remained unchanged (Figure 13B). The predictive power of DOMs was so precise that the opposing phenotypes of two paralogous nucleoporins of the same subcomplex were predicted correctly: Nup116 shifted away and formed puncta while Nup100 shifted towards the ER and did not form puncta.

Associated with the NPC are also import factors, the importins. On the PCA plot the importin heterodimer, comprised of Kap95 and Srp1 (*Enenkel et al., 1995*), shifted together with nucleoporins of the cytoplasmic interface: cytoplasmic filament and linker nucleoporins. It is known that Kap95 needs to interact with the cytoplasmic linker nucleoporin Nup116 to mediate cargo import (*Iovine and Wente, 1997*) and enhances NPC assembly (*Ryan et al., 2007*). Thus, I was interested if they formed the same type of cytosolic puncta and if both accumulated in those. Indeed, microscopy confirmed that despite the larger sizes of Kap95 puncta, all visible puncta contained both proteins (Figure 14A), suggesting that they accumulated in the same puncta upon ER stress. Since Kap95 puncta were larger than other nucleoporin puncta, I subsequently analyzed the impact of this cytosolic accumulation on nuclear import. I used a common artificial reporter to quantify nuclear import, a classic nuclear localization sequence (NLS) fused N-terminally to a fluorophore, in my case mNeonGreen (*Martinez-Bono et al., 2010; Chatterjee et al., 1997*). I ensured that cells were stressed and puncta formation occurred prior to induction of NLS-neon expression with estradiol.

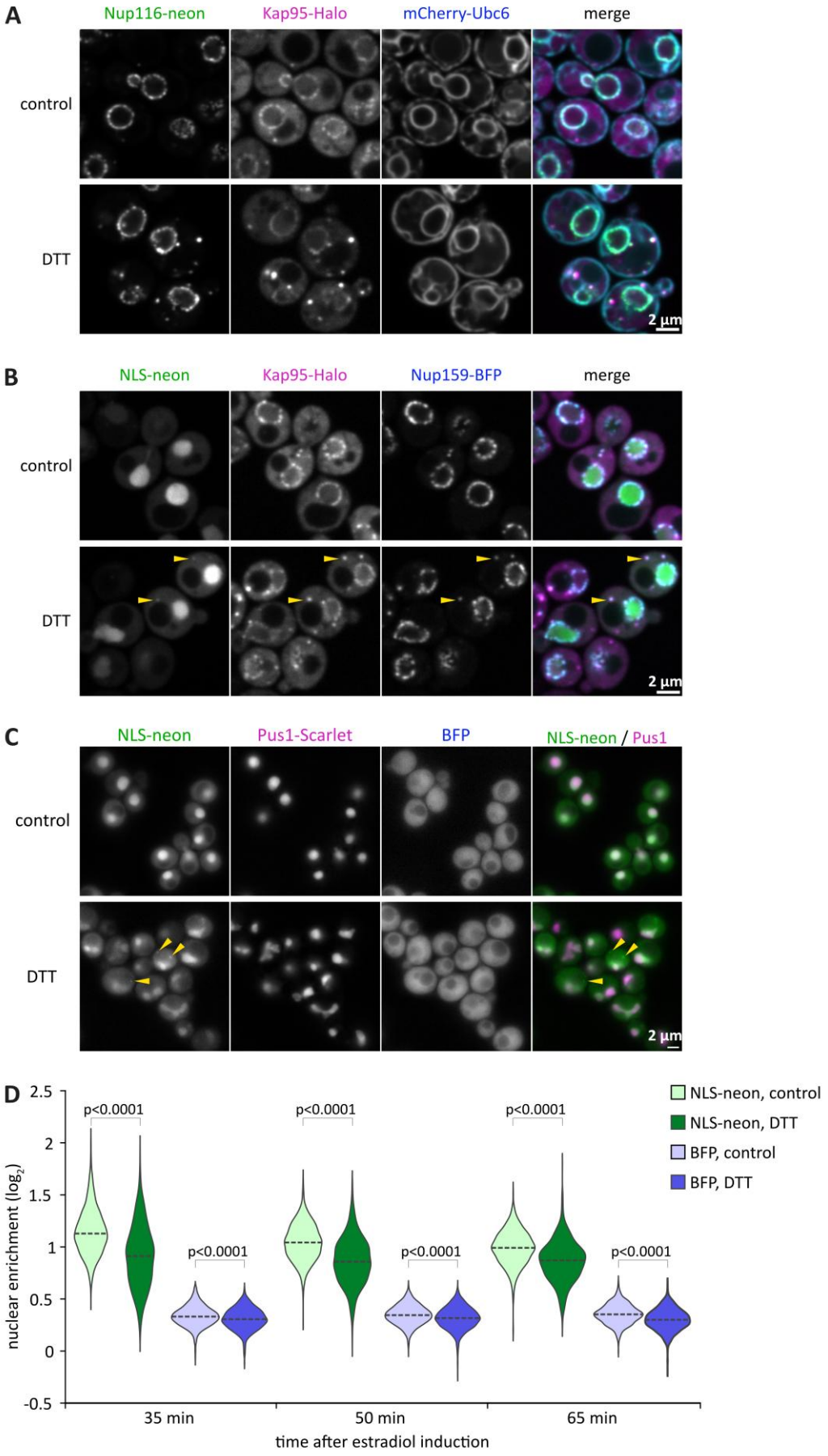

Figure 14: ER stress impairs nuclear import. (A) Confocal microscopy images of cells expressing linker nucleoporin Nup116-neon, importin Kap95-Halo together with the ER marker mCherry-Ubc6 untreated or after 2 h DTT treatment. Nup116 and

Kap95 both formed bright cytosolic puncta upon DTT treatment, which colocalized. **(B)** Confocal microscopy images of untreated or 2 h DTT-treated cells expressing mNeonGreen with a nuclear localization sequence (NLS-neon) from an inducible promoter system for 1 h, Kap95-Halo and cytoplasmic filament Nup159-BFP. All form more cytosolic puncta upon DTT, which colocalize. **(C)** Widefield microscopy images of untreated or 1 h DTT-treated cells expressing NLS-neon from an inducible promoter system for 50 min, nuclear marker Pus1-Scarlet and constitutively expressed cytosolic BFP. Upon ER stress NLS-neon forms small cytosolic puncta and has a weaker nucleus signal. **(D)** Quantification of nuclear import of untreated or 1 h DTT-treated cells expressing NLS-neon from an inducible promoter system or constitutively expressing cytosolic BFP for the indicated times. Cytosolic BFP serves as control for passive import into the nucleus. Violin plots show cellular $\log_2$ nuclear enrichment of NLS-neon or BFP nucleus signal compared to whole cell signal. 35 min >450 cells, 50 min >900 cells, 65 >900 cells in both conditions from three biological replicates were analyzed. The dashed lines indicate median nuclear enrichment. P-values were calculated with a two-tailed Mann-Whitney U-test and because of the large sample sizes all tests were statistically significant. Upon ER stress nuclear enrichment of NLS-neon was reduced at all time points.
(A) and (B) show the same display ranges for each channel for better comparison of phenotypes. (C) Ideal display ranges are shown for better visualization of the phenotype. All experiments were conceptualized, performed and arranged by me. (D) was adapted from (*Platzek et al., 2025*) and modified by me.

I observed that induced NLS-neon formed few and faint cytosolic puncta which colocalized with Kap95 and the cytoplasmic filament nucleoporin Nup159 (Figure 14B) and accumulated quickly in the nucleus, stained by Pus1 (Figure 14C). Following NLS-neon induction in pre-treated DTT cells over the course of 65 min, I observed that accumulation of newly synthesized NLS-neon in the nucleus was truly delayed, but slowly recovered upon longer NLS-neon expression (Figure 14D). To verify that NLS-neon is actively imported, I used constitutive expressed cytoplasmic BFP as control, which can passively diffuse through the NPC into the nucleus (*Timney et al., 2016*), and calculated nuclear enrichment. The distribution of BFP in nucleus and cytosol did not change upon ER stress and over the time course. This proves that active nuclear import is impaired upon ER stress, but not completely blocked since NLS-neon was still imported.

3.5 Identification of proteins affected by macroautophagy upon nitrogen starvation

I applied DOMs to nitrogen starved cells to identify novel cargo proteins and proteins involved in non-selective macroautophagy.

3.5.1 Generating starvation organellar maps

To generate starvation maps I used two strain backgrounds, control and macroautophagy-deficient. In the macroautophagy-deficient strain the E1-like enzyme *ATG7* is knocked out, disabling the lipidation of Atg8 and consequently the anchoring of cargo proteins to the phagophore membrane (Figure 15A). In order to accumulate as many autophagic cargo proteins as possible in the vacuole, both my control and autophagy-deficient mutant harbored *PEP4* and *PRB1* knockouts, which impaired degradation of proteins in the vacuolar lumen (*Takeshige et al., 1992*). In the following I will refer to the *Δpep4 Δprb1* strain as "WT" and the *Δpep4 Δprb1 Δatg7* strain as "Δatg7". I subjected my cells to 6h of nitrogen starvation, to ensure proper accumulation of cargos in the vacuole, before subjecting it to subcellular fractionation (Figure 15A).

I generated triplicate maps of WT control, WT starved, Δatg7 control and Δatg7 starved cells. All four organellar maps were measured using the more sensitive data-independent acquisition (DIA). Across the 12 maps we detected 4562 protein profiles of which 4298 were mapped consistently, representing about 80% of the yeast proteome (*Ho et al., 2018*) and obtaining over 40% more complete profiles compared to data-dependent acquisition (DDA) measured ER stress maps.

Analysis of the full proteomes, performed by Georg Borner and me, revealed that out of the 4577 detected proteins, 883 in WT starved cells and 674 in Δatg7 starved cells were significantly up- or downregulated. Previous data identified 264 significantly differentially regulated proteins upon 3h nitrogen starvation (*Muller et al., 2015*), which included the core autophagy machinery, Cvt pathway cargos, amino acid biosynthesis and transport and glycogen synthesis. 183 of these proteins were also differentially regulated in both starved strains (Figure 15B). The most prominent protein to be upregulated by starvation was Atg8, which was 2.8-fold enriched in both starved cells. Furthermore, the abundance of proteasomal proteins remained constant in all cells, exactly as described by (*Muller et al., 2015*) and it has been shown that nitrogen starvation slightly decreases proteasomal activity in WT cells, which

is recovered with autophagy-deficient mutants (*Athane et al., 2015*). Hence, any significant abundance changes detected can be attributed to transcriptional or translational regulation.

Of the 1019 differentially expressed proteins upon starvation, 511 were shared between the two strains (Figure 15C). Interestingly, in the Δatg7 strain 200 fewer proteins had significant abundance changes, implying that simply the transport of proteins and lipids by macroautophagy affected transcription and translation, which was reduced in an autophagy-deficient strain.

GO term enrichment analysis revealed that WT and Δatg7 cells respond in the same way to starvation (Figure 15D). Both strains upregulated components of the Cvt pathway, and amino acid catabolism for enhanced degradation of amino acids in the vacuole, similar as previously reported (*Muller et al., 2015*). On the other hand cell division and ribosome biogenesis (nucleolus, preribosome) were downregulated since starvation leads to TORC1 inhibition which is the main regulator of protein synthesis, metabolism and growth (*Gonzalez and Hall, 2017; Kira et al., 2014*). Interestingly, cytoplasmic proteins were regulated in different directions in WT and Δatg7 cells. In WT cells there was hardly any median abundance change, while in Δatg7 these components are downregulated. Because of the large number of proteins in that category the abundance changes were subtle but still significant. Most of these changes and directions agreed with the previous data (*Muller et al., 2015*), except for the median plasma membrane proteins, which were slightly upregulated in my cells. This could be because of longer treatment and a different strain background used by (*Muller et al., 2015*), which was still able to degrade proteins in the vacuole. Additionally, plasma membrane and cell wall proteins are usually internalized via endocytosis and transported to the vacuole via the MVB pathway (*Jones et al., 2012*). These processes were still functional in my autophagy-deficient strain.

In summary, starvation caused substantial protein abundance changes in both strains, of which the autophagy-deficient strain was slightly less affected. Nonetheless, both strains differentially regulated the same pathways and proteins, presumably transcriptionally and translationally. This suggests that macroautophagy together with many other pathways mediated the cellular stress response to counteract starvation.

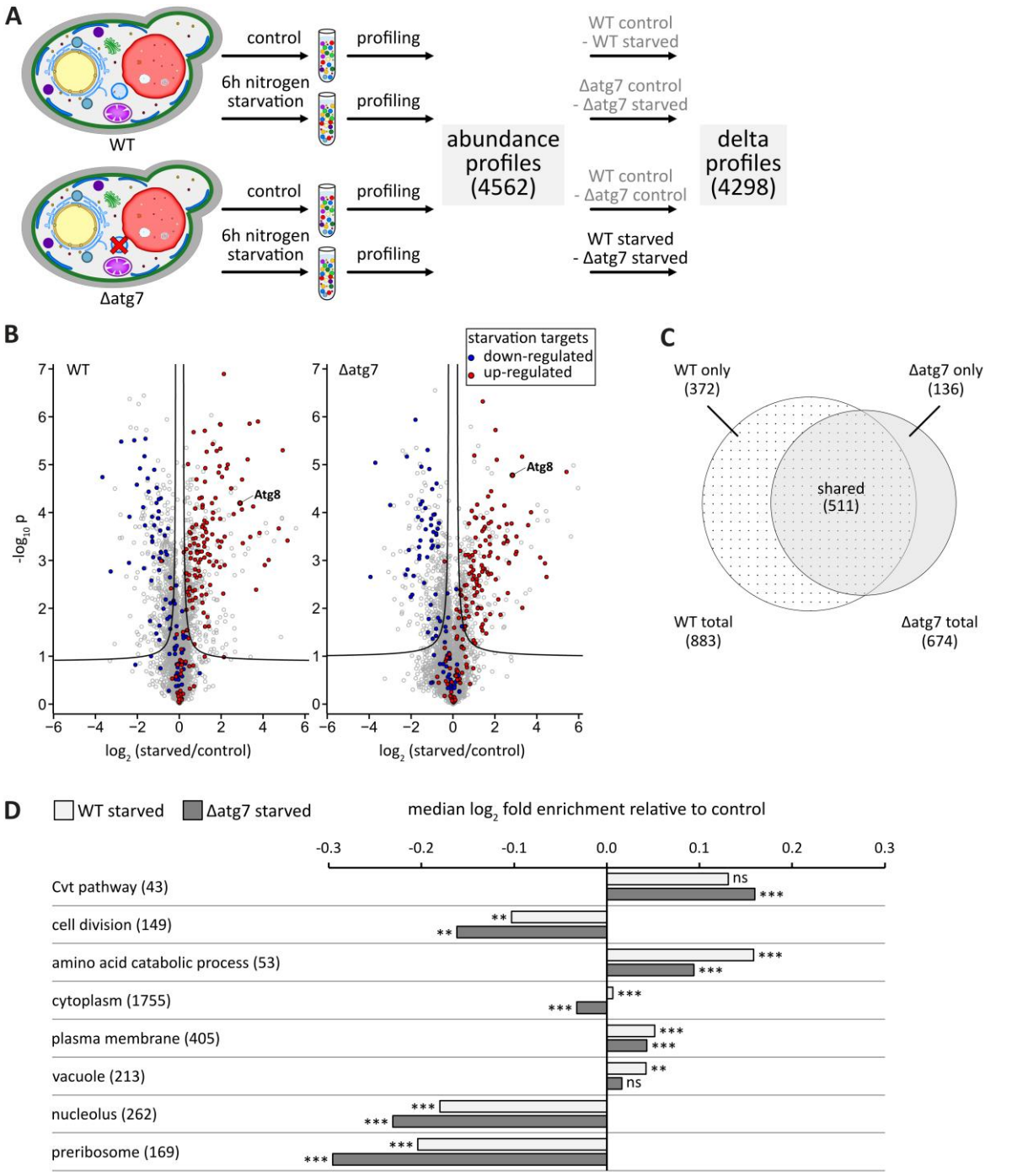

Figure 15: Protein abundance changes upon nitrogen starvation. (A) Workflow of dynamic organellar mapping for nitrogen starvation. WT and macroautophagy-deficient Δatg7 strains were treated as indicated and subjected to subcellular fractionation and mass spectrometry profiling. The quality filtered dataset contained 4562 abundance profiles, after filtering for complete profiles over all 12 maps, 4298 profiles were used for subsequent data analysis. The delta profiles generated are indicated, the black delta profile is used to identify proteins involved in macroautophagy. **(B)** Volcano plots of full proteomes of nitrogen-starved WT and Δatg7 cells. Plotted are the $\log_2$ fold abundance changes upon starvation against their respective significance value (p-value), determined with a two-tailed t-test. Volcano lines mark 5% FDR cut-offs based on data permutation. Highlighted in red and blue are proteins identified by (*Muller et al., 2015*) to be up- or downregulated upon 3h starvation, respectively. **(C)** Venn diagram of differentially regulated proteins upon starvation in either WT cells, Δatg7 cells or both. **(D)** Gene ontology enrichment analysis of full proteomes of starved WT or Δatg7 cells compared to their respective control. Selected terms show shared up- or downregulation in both strains. The number of proteins assigned to each term is

indicated in brackets. Significant enrichment of terms is labeled as follows: ns, not significant; *, p<0.05; **, p<0.01; ***, p<0.001. (A) was adapted from (*Platzek et al., 2025*) and modified. Full proteomes were filtered and normalized by Georg Borner. I performed the analysis and plotted the data in (B), (C), (D).

Since many of the proteins, in which we were interested, are cytosolic we included all six membrane fractions and additionally the cytosol fraction (7-point profiles) to all subsequent analyses. As before, to evaluate utility of the organellar maps, I performed PCA and plotted the results. The individual plotted maps display good separation of most organelles in all four conditions (Figure 16A). Several organelles did not shift, such as mitochondria and proteasomes, which also did not change their average cytosolic pools (data not shown). When comparing WT and Δatg7 control with their starved counterpart, the vacuole cluster shifted partially and most other membranous organelles shifted with it. The cytosol cluster only shifted towards the vacuole in starved WT cells, but remained stable in the other conditions. The ribosome cluster was the only one which shifted in opposite directions. In starved WT samples, ribosomes shifted towards the vacuole cluster, whereas in starved Δatg7 samples it mostly shifted away. These shifts were expected, since ribosomes are selectively and non-selectively cleared by starvation-induced autophagy, which was impaired in the mutant (*Takeshige et al., 1992; Kraft et al., 2008; Takeda et al., 2024*).

Georg Borner performed several MR analyses to identify significant shifting proteins upon starvation. Initially, to verify the suitability of the maps, WT control was compared to WT starved (data not shown). As expected, the four components of the TOR1 complex, Tor1, Kog1, Tco89 and Lst8, were among the 419 significant hits with consistent high M and R scores (>4.3; >0.97). Upon starvation TORC1 was inactivated and relocated from the vacuole to distinct perivacuolar sites (*Hughes Hallett et al., 2015*). This process was observed in the organellar maps, where TORC1 shifted from the core vacuole cluster towards the peripheral vacuole together with other peripheral vacuole complexes (Figure 16B). Furthermore, components of the autophagy machinery and the Cvt pathway, Atg1, Atg3, Atg21 and Atg34, were predicted to shift significantly upon starvation compared to control WT cells. After starvation induction in WT cells, these components all shifted towards the vacuole. In Δatg7 cells, however, Atg1 and Atg3 stayed in the cytosol upon starvation. They interacted with Atg8 during autophagosome formation and Atg8 lipidation (*Kraft et al., 2012; Yamaguchi et al., 2010*) and hence stayed in the cytosol with Atg8. The cargo receptor Atg34 targeted Ams1, a mannosidase to the vacuole via the Cvt pathway, which could not be anchored to the phagophore and thus Atg34 did not shift as strongly towards the vacuole in starved Δatg7

cells. Atg21 is required for vesicle formation in the Cvt pathway (*Meiling-Wesse et al., 2004*) and shifted from the cytosol towards the vacuole in Δatg7 cells but not as prominent as in WT cells, most likely because Atg21 functions upstream of Atg8 lipidation and was found to not be needed for starvation-induced autophagy (*Stromhaug et al., 2004*).

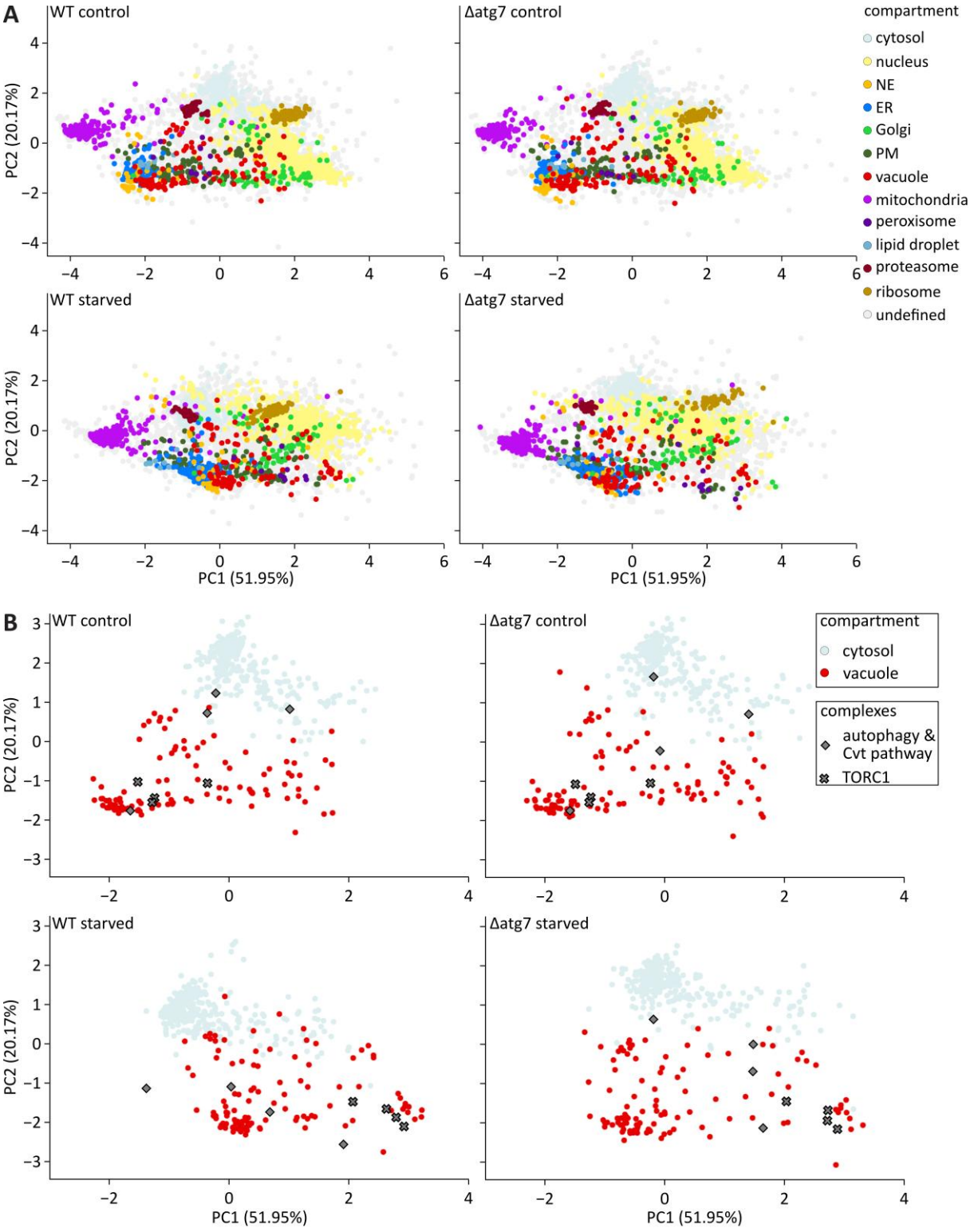

Figure 16: Organellar maps of control and starved WT and autophagy deficient cells. (A) PCA plot of control and starved WT and Δatg7 organellar maps. Plots show averaged biological triplicates of 7-point profiles. Defined marker proteins are

displayed in color; all other proteins are annotated as “undefined”. Upon starvation ER, NE, Golgi and vacuole clusters showed the strongest shift in both WT and Δatg7. The ribosome cluster shifted oppositionally in starved WT and Δatg7 maps. PCA was performed and plotted by me. **(B)** Same PCA plots as in (A). Displayed are cytosol and vacuole marker proteins. Highlighted are components of the autophagy machinery, the Cvt pathway and the TORC1 complex which are known to be affected by starvation in both strains. Upon nitrogen starvation the TORC1 complex shifted from the core vacuole cluster to the periphery. In WT cells the autophagic and Cvt components shifted from the cytosol towards the core vacuole , whereas in Δatg7 cells they shifted only partially from the cytosol to the peripheral vacuole. PCA in (A) and (B) were performed and plotted by me.

In conclusion these preliminary results demonstrated that the cellular response to starvation was still active in Δatg7 cells, but the formation of autophagosomes and cargo tethering to the phagophore membrane was defective. This verifies that the transport of autophagic and Cvt cargos towards the vacuole was impaired in the autophagy-deficient mutant and potential cargo proteins stayed in the cytosol.

3.5.2 Starvation-induced protein localization changes

To identify new proteins whose transport is Atg8-dependent and thus are involved in non-selective autophagy either as cargo or associated with the process itself, the two maps WT starved and Δatg7 starved were analyzed.

The MR analysis (Figure 17A) in the DOM-ABC web app obtained 126 significantly shifting proteins (FDR <5%), of which almost half were annotated in the reference database as cytosolic. 17% of the hits were nuclear proteins, which roughly depicted the ratio of nuclear proteins mapped across all four maps and 22% of the hits were shuttling proteins and unknown proteins, summarized in “others”. ER, Golgi and mitochondrial proteins were underrepresented as significant hits compared to proteins mapped (Figure 17B). This suggests that the majority of shifting proteins were associated with Atg8. As DOMs identified so many cytosolic proteins, these could be undefined cargo proteins, but also potential machinery for cargo recognition and transport from other organelles.

I highlighted all 126 MR hits in the PCA plots of the two starved maps (Figure 17C), from which I annotated proteins known to be involved in autophagy (Atg1, Atg8), ribosome autophagy receptor (Hab1) and cargo proteins (Fas1/2) (*Shpilka et al., 2015; Jang et al., 2024*).

All annotated proteins shifted from the vacuole strongly towards the cytosol cluster in the starved Δatg7 map. The subunits of the fatty acid synthetase Fas1 and Fas2 are known to be preferentially degraded by macroautophagy via direct binding of Atg8 upon nitrogen starvation. The kinase Atg1 responsible for phagophore assembly site formation, interacted

with Atg8 via its AIM (*Kraft et al., 2012*). Since Atg8 is not tethered to the autophagosome, all of the annotated interacting proteins shifted towards the cytosol cluster.

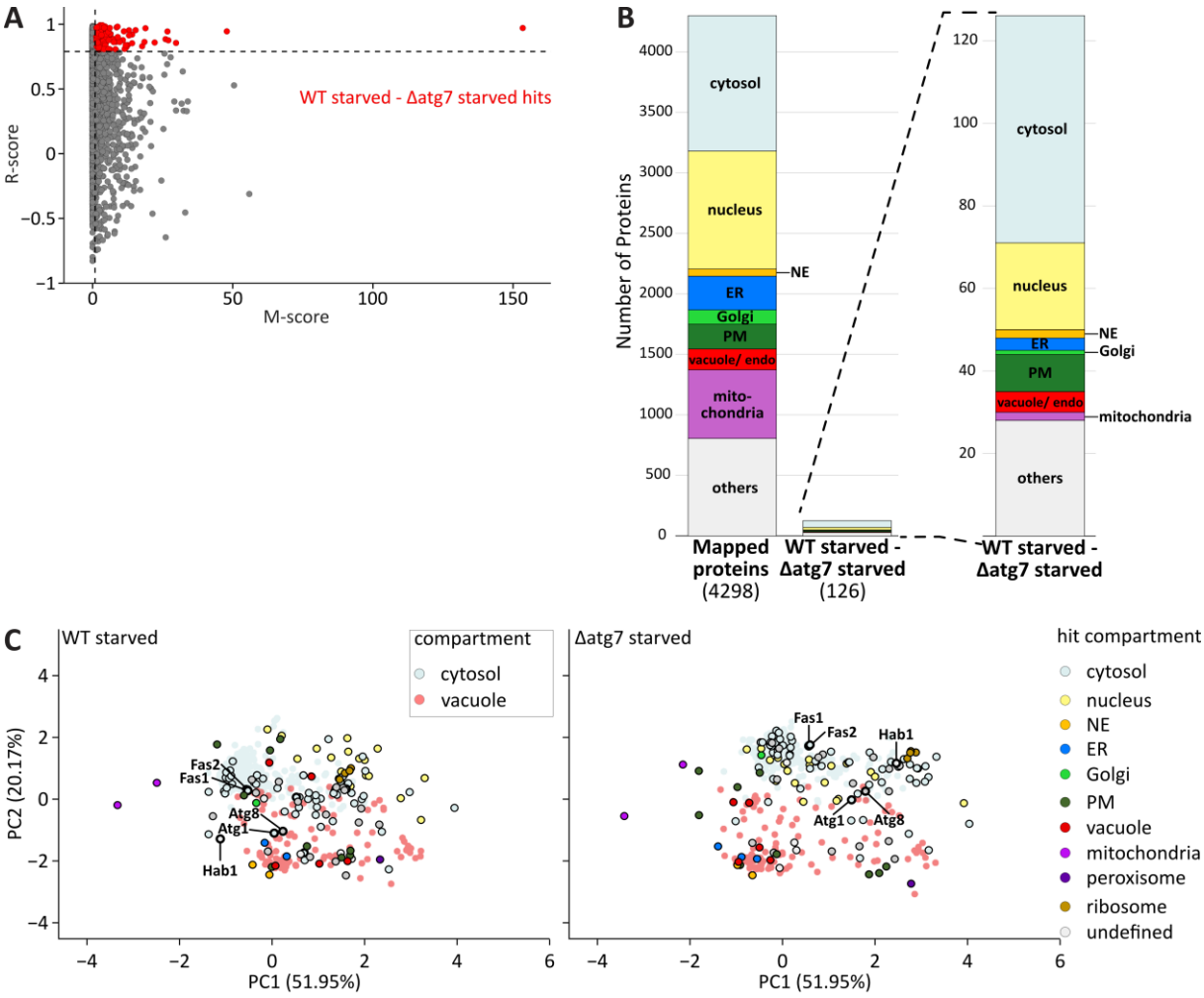

Figure 17: Protein localization changes upon starvation in autophagy deficient cells compared to WT cells. (A) Detection of significant shifting proteins in autophagy deficient (Δatg7) samples compared to WT upon starvation. Cutoffs were defined as movement (M) score >1.3, reproducibility (R) score >0.8 and hits are highlighted in red. **(B)** Bar graphs showing reference database annotated compartments of all proteins mapped across 12 maps (left) and the 126 MR hits (right). Cytosolic, nuclear and several combined localizations (others) are overrepresented in the hits. ER, Golgi and mitochondrial proteins are underrepresented in the hits compared to all mapped proteins. **(C)** PCA plot of starved WT and Δatg7 maps. Cytosol and vacuole clusters are transparently displayed as reference. Highlighted are all MR hits from (A). Labeled are either cargo or autophagy-associated proteins with high M and R scores. Plot from (A) was generated by DOM-ABC web app (*Schessner et al., 2023*) and adapted by me. (B) was generated and arranged by me. (C) PCA was performed and plotted by me.

By far the highest M-Score obtained the recently described autophagy receptor Hab1, for selective degradation of ribosomes (called ribophagy) (*Takeda et al., 2024*). Hab1 clustered closely with the 4 ribosome hits in the Δatg7 map, but it was not detected in any of the two control maps, preventing us from tracing the complete shift trajectory. Moreover, Hab1 was also significantly upregulated (3.3 and 2.3-fold) upon starvation. The neighborhood analysis revealed that in WT starved maps Hab1 had many cytosolic neighbors and components of the

autophagy machinery, whereas in starved Δatg7 cells almost all neighbors were ribosomal proteins or proteins involved in ribosomal RNA processing (data not shown). Moreover, the cytosolic proteins, shifted further away from the vacuole in starved Δatg7 cells, indicating that they were previously sequestered in autophagosomes and transported to vacuoles. Different from what the PCA plots suggest, the nucleus hits moved closer to the cytosol cluster, but cytosol shift analysis revealed that they had reduced cytosolic pools in starved Δatg7 cells and neighborhood analysis revealed that the nucleus neighbors increased. This illustrates that the 2-D reduction of the organellar maps neglected information, which was misleading when interpreting results. Nevertheless, the nucleus hits were predominantly involved in RNA processing and modification and were negligibly downregulated in WT and Δatg7 cells upon starvation, suggesting that these proteins changed their localization upon starvation but most likely not by macroautophagy or proteasomal degradation.

All in all, MR analysis identified many shifting proteins which were affected by impaired autophagosome formation and tethering to the phagophore membrane, likely representing undefined cargo proteins degraded by macroautophagy.

Since non-selective autophagy predominantly degrades cytosolic cargo, we also included the cytosolic shift analysis to identify potential new cargo proteins. This identified 128 cytosolic proteins whose cytosolic pool was greatly decreased <60% upon starvation in the WT but recovered to >90% in the Δatg7 mutant, implying that their depletion from the cytosol in WT cells was induced by macroautophagy.

I combined the MR analysis, the cytosolic shift analysis and the whole proteome data and found that among the 211 combined hits, the median abundance changes of both WT starved and Δatg7 starved was almost unchanged. Hence, I concluded that, like the ER stress maps, macroautophagy associated proteins upon starvation were rather spatially regulated than transcriptionally.

I summarized all 45 shared hits of both MR analysis and cytosol shift analysis in Table 2. Determining shift directions was not possible since the predicted localization of almost all MR hits remained identical in both WT starved and Δatg7 starved cells (data not shown). If the predicted shifts can be exclusively attributed to suborganellar localization changes, hence not noticeable for the SVM compartment classification, needs to be evaluated experimentally.

Table 2: Summary of starvation hits. Listed are 45 shared hits of both analyses (MR, cytosolic shift) WT starved vs Δatg7 starved. Proteins were summarized based on their GO term biological process (Uniprot). List of proteins and process annotation was generated by me.

biological process	proteins
autophagy, Cvt pathway	Atg3, Atg8, Atg19, Atg34, Ypt1
amino acid biosynthesis	Gly1, Sam1, Sam2
carbohydrate metabolism	Psk2, Pyc1, Ugp1
lipid metabolism	Fas1, Fas2, Ipt1
transport via Golgi	Avl9, Gea1, Mrs6, Rhb1
RNA processing & modification	Elp3, Iki3, Kti12, Mes1, Rio1, Rio2, Sap185, Snm1, Uba4
Ribosome & Ribosome-associated	Rmt2, Rpl37a, Rps3, Sqt1
others	Apl1, Ast1, Cab4, Coq8, Dph6, Ftr1, Gcg1, Iwr1, Nup49, Rts3, Ygl039w, Ygl117w, Ypk3, Yrb30

Next, I annotated and grouped biological processes to comprehend which pathways might be affected by non-selective autophagy.

Nine of the shifting proteins are part of metabolic processes such as amino acid biosynthesis, carbohydrate metabolism and lipid metabolism, all pathways which are strongly affected by starvation (*Natarajan et al., 2001; Li et al., 2015*) (Table 2). Amino acid synthesis, carbohydrate metabolism especially glycogen homeostasis and many more starvation induced pathways are all regulated via the transcriptional activator Gcn4 (*Natarajan et al., 2001*), which is activated upon TORC1 inhibition. Besides the fatty acid synthetases Fas1 and Fas2, Ipt1 involved in sphingolipid synthesis was found to be changing its localization. This demonstrates that only proteins involved in synthesis or regulation of metabolic processes changed their localization upon starvation, pointing towards a potential new regulatory mechanism for cellular stress response upon starvation.

Moreover, 13 proteins are associated with RNA processing, ribosome biogenesis and ribosomes. Since these proteins were inhibited and downregulated upon TORC1 inhibition (*Powers and Walter, 1999*) it was interesting to find this category also to change their localization upon starvation.

Unfortunately, we were not able to refine the data analysis without further experimental validation. The average vacuolar abundance profile and thus the vacuolar cluster, was not as

well defined upon starvation as expected, preventing useful results of correlation analyses of MR hits or cytosolic release hits (Figure 18A, B).

During starvation, proteins in the vacuole accumulated by other intact pathways. This ultimately changed the vacuolar sedimentation characteristics. Initially, I expected that the vacuole became bigger so that the peak vacuolar signal shifted from the 6k fraction to the 3k and 1k fraction, but upon starvation the highest total signal, in both WT and Δatg7, was detected in the 12k fraction, so the fraction with smaller particles. In contrast, the average profile of Atg8, the cargo adaptor protein inside the phagophore membrane, was equally distributed in WT and Δatg7 control cells. Upon starvation the main Atg8 peak in WT sample was accumulating in the 6k fraction, similar to the control vacuolar profiles. In starved Δatg7 cells, on the other hand, the Atg8 profile showed a dramatic shift into the 78k fraction with big protein complexes such as ribosomes.

These changes in sedimentation behavior suggest that Atg8 was accumulating in the vacuole in starved WT cells but was freely relocalizing in the cell in the autophagy-deficient mutant.

Next, Sebastian Schuck thoroughly annotated all vacuolar proteins with their membrane topology (Uniprot) and I visualized the annotations in the PCA plot (Figure 18B). As previously observed, the vacuolar cluster was loosely scattered across all four maps. But this illustration demonstrates that most integral vacuolar membrane proteins built the core vacuole cluster, some peripherally attached complexes segregated from the integral membrane protein core and the lumenal vacuolar proteins are located closer to the cytosolic core cluster. Most of the peripheral vacuolar complexes stayed compact while shifting away from the integral membrane proteins, such as the V1 subunit of the V-ATPase or the TORC1 activity regulating SEACAT and SEACIT complexes (*Panchaud et al., 2013*) together with TORC1 components. This separation is even more pronounced in both starved samples.

I subsequently determined the amount of lumenal vacuolar proteins found in the cytosol, giving a good estimation of the intact state of the vacuole during subcellular fractionation (Figure 18C). In all four maps, nearly all lumenal proteins had a cytosolic pool between 10% and 50%, thus I assume that during lysis of my cells the vacuole was ruptured and lumenal proteins leaked into the supernatant. This observation is more striking in the Δatg7 mutant samples, suggesting that the stability of the vacuole was affected by impaired autophagy.

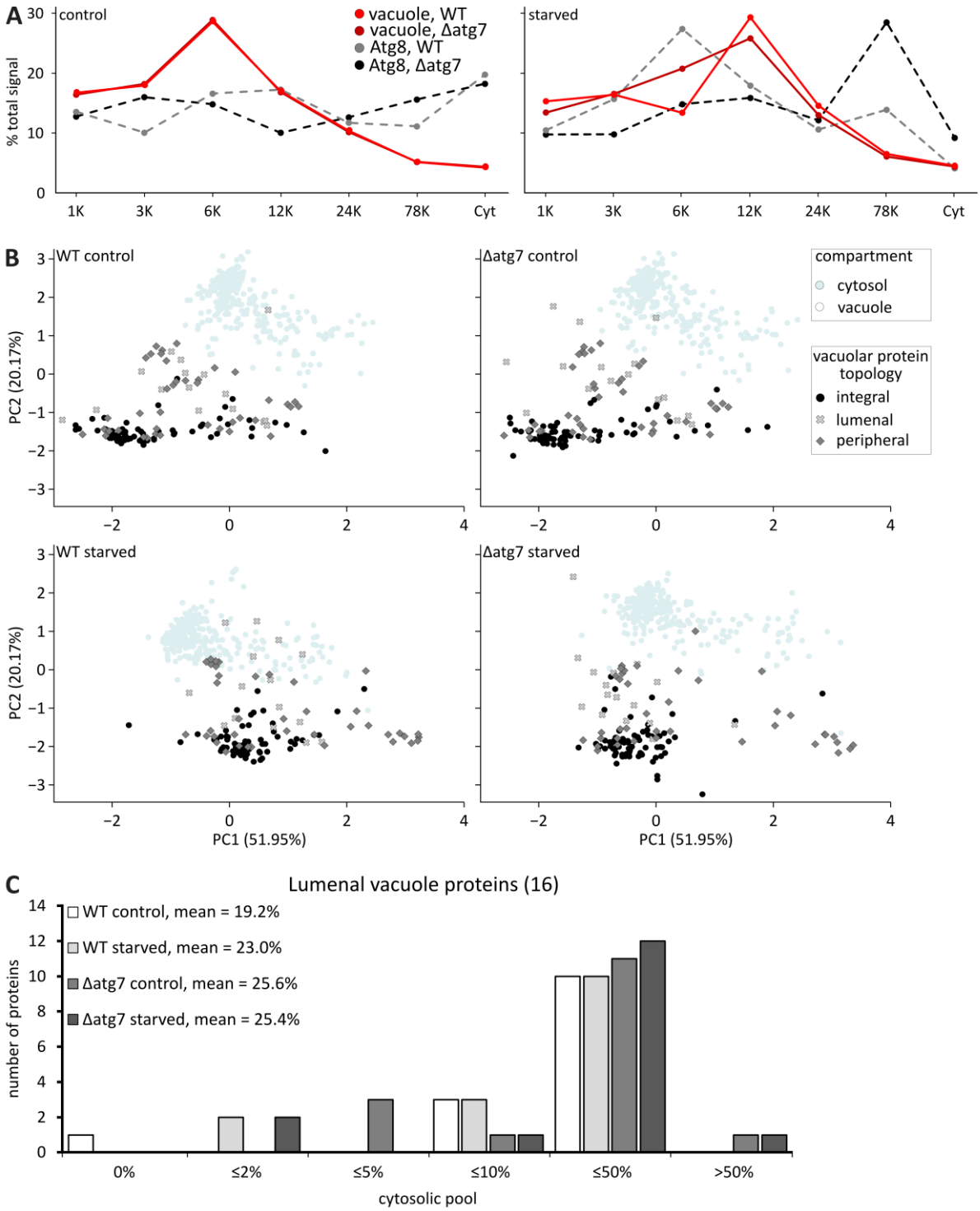

Figure 18: Peripheral membrane and lumenal vacuole proteins leak into the cytosol. (A) Abundance profiles of all averaged vacuole markers (red lines) and averaged Atg8 (grey and black lines) in control (left) and starved (right) maps. Vacuole profiles in WT and Δatg7 maps align exactly in control conditions and predominantly in starved conditions. Atg8 profiles in WT and Δatg7 maps align partially in control conditions but diverge completely in starved conditions. (**B**) PCA plots of starvation maps. Shown are the cytosol marker proteins and all mapped vacuole proteins. Topology of vacuole proteins is annotated with different symbols. Integral vacuole membrane proteins formed the core vacuole cluster, whereas peripheral vacuole membrane proteins shifted away partially. (**C**) Leakage analysis of lumenal vacuole proteins in all four starvation maps. Bar graphs show number of proteins with different cytosolic pools. Average leakage was between 20 and 25%. (A) was arranged by me. PCA in (B) was performed and plotted by me. (C) was generated and arranged by me.

In summary, starvation maps predicted many proteins known to be involved in the Cvt pathway or macroautophagy such as, Atg19, Atg1, Atg3, Atg8 and Hab1, verifying the suitability of the DOM results. The selected 45 hits serve as basis to experimentally validate their non-selective degradation by macroautophagy.

4 DISCUSSION AND OUTLOOK

In this study, I successfully established Dynamic Organellar Maps (DOM) in yeast, applied it to stressed cells and systematically evaluated localization changes by microscopy. The combined approach demonstrated that DOMs consistently detected valid changes in organellar remodeling on a global scale. Moreover, my results prove that upon stress, organellar remodeling by protein suborganellar redistribution is an underestimated but known process to maintain cellular homeostasis (*Litsios et al., 2024; Hein et al., 2025*).

4.1 Establishing DOM in yeast

Generating organellar maps is relatively easy. Since the organelles are only crudely purified, DOMs is fast, reproducible, the amount of samples is high and potential membrane contact sites might be preserved. The availability of all these factors, simplifies the investigation of intracellular trafficking and signaling, metabolic processes, organelle biogenesis and remodeling.

Because DOMs is a label-free mass spectrometry method, the native proteins and organelles are analyzed. This enables me to correct previous annotations purely based on high-troughput microscopy and *de novo* detection of many proteins, which are up to now still lost or dysfunctional in screening libraries because of the compromising tag (*Breker et al., 2013; Weill et al., 2019; Weill et al., 2018*).

Now that I have generated yeast reference organellar maps, it will be easier for other laboratories to establish, adapt and optimize this method for their own research questions.

Recent developments in mass spectrometry technology and computational analysis enabled my collaborator Georg Borner to measure my latest organellar maps, the starvation maps, with DIA. This technique allows to select multiple precursor ions at once and enhances sensitivity and hence numbers of detected peptides and proteins (*Chapman et al., 2014; Demichev et al., 2022*). The DIA measured starvation maps obtained 40% more complete profiles over a larger amount of maps, compared to reference and ER stress maps. Using DIA for future DOM applications will improve detection of low abundant proteins, illuminating signaling pathways and stress responses.

4.2 DOMs detect specific localization changes upon ER stress

4.2.1 Misfolding and selective retention of secretory pathway proteins

The predictive power of protein localization changes by DOMs was improved throughout this project, resulting in not only the detection of a large number of hits but also the precise prediction of almost 80% of the directions of DTT-induced localization changes. This revealed several extensive trends of organellar remodeling upon ER stress. Many proteins of the secretory pathway are retained in the ER, specifically proteins targeted to the vacuole via the CPY pathway, mannosyltransferases in the Golgi and almost all mapped GPI-anchored proteins.

Moreover, four of the ERGIC hits, Emp24, Erv25, Erp1, Erp2, belong to the cargo receptor p24 family and mediate transport of Golgi targeted proteins from the ER to the Golgi in COPII vesicles (*Strating and Martens, 2009*). All p24 family members are structurally very similar and contain a domain which is presumably stabilized by several disulfide bonds (*Anantharaman and Aravind, 2002*). Upon DTT treatment, they misfold and therefore cannot recognize and export cargo proteins. This hypothesis is supported by the fact that all of these are not predicted to shift significantly upon Tm and might be still functional. This could be tested by following a specific cargo such as GPI-APs and compare DTT and Tm treatments.

It has been shown that upon deletion of p24 family proteins Gas1 is not exported anymore (*Marzioch et al., 1999*). Hence, I conclude that the ER retention of GPI-APs is a combined defect of impaired glycosylation, misfolding and inaccessible export receptors.

Five of the 410 DTT MR hits were components of the OST. It was shown that for the active site cysteine of both Ost6 and its paralogue Ost3 the redox state affected efficiency of N-glycosylation (*Schulz et al., 2009*). Hence, DTT treatment decreased site-specific glycosylation and subsequent N-glycosylation is impaired for selected glycosylation sites, leading to misfolding of specific polypeptides.

There is a tendency that proteins shifting towards the ER are more likely to be modified, because two thirds are annotated as glycosylated, form disulfide bonds or have GPI-anchors, compared to one third of all defined post-ER proteins with a modification. However, the annotations might not be complete, some of the glycosylated hits are not hits in the Tm maps, hence there might be other mechanisms as to why specific non-modified proteins are predicted to shift towards the ER.

4.2.2 ER reflux of selected lumenal chaperones

DOMs revealed another known process, the relocalization of specific lumenal ER chaperones from the ER to the cytosol (*Igbaria et al., 2019; Lajoie and Snapp*). We were able to specifically predict and extend the list of chaperones undergoing this reflux. However, there is no structural or functional discrepancies between the five verified refluxed and the unchanged Ero1 or other chaperones without cytosolic pool.

This ERAD-independent process, is supposedly mediated by fully folded and functional chaperones to potentially remove small secretory proteins as a way to debulk the ER lumen or to regulate cytosolic processes by sequestering cytosolic proteins and interrupting signaling. The machinery and regulation of recognition of specific chaperones and transport out of the ER into the cytosol is not understood.

Mammalian protein disulfide isomerases were found to be present in the cytosol and regulate cytosolic transcription factors or stabilize cytosolic proteins (*Kobayashi et al., 2021; Guo et al., 2002*). Analysis of the cytosolic pools revealed that in control a small amount of Pdi1, Kar2 and Cpr5 had detectable cytosolic pools, which increased more than 10-fold upon ER stress (Figure 10A). Hence, lumenal ER chaperones in yeast might also have additional regulatory functions in the cytosol upon ER stress.

4.2.3 Selective exclusion of ER shaping proteins from the general ER membrane

Proteotoxic stress, like DTT and Tm induced ER stress, induces ER expansion by generating more ER sheets than tubules to facilitate protein folding (*Papagiannidis et al., 2021; Schuck et al., 2009*). (*Reinhard et al., 2024*) analyzed the lipid composition of the ER membrane in BY4741 yeast cells and showed that DTT and Tm-treated cells have overall reduced anionic lipids which could not be compensated by enhanced phosphatidic acid (PA) synthesis and diacylglycerol. Furthermore, lipids became longer and more saturated, affecting membrane thickness and fluidity. This in turn leads to lipid bilayer stress and hydrophobic mismatch of membrane proteins, affecting their structure, topology and oligomerization (*Renne and Ernst, 2023*).

DOMs was able to predict the known shift of integral tubular ER membrane shaping proteins Rtn1 and Yop1 from the ER into the cytosol fraction (*Papagiannidis et al., 2021*), together with newly identified tail-anchored Dpm1. Rtn1 and Yop1 both contain a reticulon homology

domain (RHD) which are hydrophobic transmembrane segments, which only span the membrane partially and therefore might adopt a wedge-shaped structure (*Hu et al., 2008*). Because of this transmembrane conformation, reticulons and related shaping proteins might be very susceptible to lipid bilayer stress.

ER stress induces ER expansion by generating more ER sheets than tubules to facilitate protein folding (*Papagiannidis et al., 2021; Schuck et al., 2009*). Reticulons and Yop1 induce membrane curvature, hence they localize to ER tubules and ER sheet edges (*Shibata et al., 2010*). Upon excessive generation of ER sheets the amount of tubular shaping proteins exceeds the demands of the flat sheets and hence needs to be reduced. Since the abundance of these proteins did not change, they are neither transcriptionally downregulated nor degraded. Moreover, the clusters contained exclusively ER membrane proteins, were formed independent of the autophagy machinery and dissolved after DTT removal (Natalie Friemel, Klára Odehnalová; unpublished). Hence, it is possible that folded and functional proteins are recruited from the ER into ER subdomains and either stay embedded in a membrane or are extracted by cytosolic chaperones, which keep them in a "waiting position" until stress is resolved and they are reintegrated into the ER membrane. Surprisingly, I found Msp1, a AAA-ATPase in the outer mitochondria membrane to be in the close neighborhood of Rtn1, Yop1 and Dpm1, and vice versa. Msp1 recognizes and extracts mislocalized tail-anchored proteins from the outer mitochondria membrane or peroxisomes and passes them to the GET machinery for targeting to the ER and degradation by the ERAD pathway (*Matsumoto et al., 2019; Matsumoto et al., 2022*). Moreover, Msp1 is 3-fold upregulated and shifted away from mitochondria upon DTT stress. Thus, I suggest that Msp1 recognizes destabilized Dpm1 in an unknown mechanism, extracts Dpm1 and with it, other membrane proteins in the same ER subdomain. How this clustering is regulated and if these proteins are still attached to the ER membrane and reinserted back into the ER membrane, remains to be investigated.

4.2.4 Nuclear pore complex assembly might be impaired

Surprisingly as a new aspect of organellar remodeling during ER stress, DOMs showed me that NPC integrity and nuclear import are altered. Formation of cytosolic puncta of nucleoporins upon stress have been reported before in both yeast and metazoan (*Garcia et al., 2021; Thomas et al., 2023; McGoldrick et al., 2023*), presumably as a result of cytosolic protein condensates. However, the selective formation of cytosolic puncta of not only phenylalanine-

glycine-rich nucleoporins (FG-nucleoporins) but of all nucleoporins, predicted to move away from the NE cluster in the PCA plot, has not been observed to this extent. It is yet unclear why and how nucleoporin puncta form upon ER stress. Current literature describes puncta formation of FG-nucleoporins due to unfunctional Nup116 and karyopherins impairing NPC assembly (*Ryan et al., 2007; Lord and Wente, 2020*). I speculate that ER stress affects NPC assembly and thus impairs nuclear import by the Kap95 pathway, because of misfolding of newly synthesized nucleoporins and importins.

Furthermore, the ERAD pathway contributes to clearing of misfolded cytosolic proteins. Prolonged ER stress can overload the proteasome and thereby accumulated misfolded proteins reduce cytosolic chaperone availability (*Schmidt et al., 2019*), suggesting that newly synthesized nucleoporins, misfold and aggregate in the cytosol because they could not be degraded yet.

Yet, the FG-nucleoporins of the nuclear basket were less affected by ER stress. All linker nucleoporins and FG-nucleoporins are co-translationally assembled in the cytoplasm. In contrast, Nup1 and 2 in the nuclear basket are locally translocated at the NPC (*Lautier et al., 2021; Seidel et al., 2022*). Hence, it is likely that the FG-nucleoporins of the nuclear basket were less affected by ER stress, because nuclear import was still functional but retarded and thus I did not observe puncta formation.

Moreover, it is proposed that FG-nucleoporin Nsp1 possesses chaperone functions to regulate the phase state of FG-nucleoporin condensates promoting a liquid-like state of native cytosolic condensates (*Otto et al., 2024*), which is in agreement with Nsp1 being the only nucleoporin cytosolic shift hit. Lastly, ER stress might induce a partial disassembly of existing NPCs and subsequent degradation via autophagy. This is similar to long-term starvation where Nup159 acts as selective autophagy receptor and binds Atg8 via its AIM (*Lee et al., 2020*).

The altered lipid environment of ER and nuclear envelope membranes might compromise nuclear envelope remodeling for NPC assembly and insertion (*Thaller et al., 2021*). Molecular dynamic simulations revealed that upon DTT and Tm the ER membrane is significantly thicker (*Reinhard et al., 2024*), potentially affecting fusion of inner and outer nuclear envelope membrane (*Kralt et al., 2022*) and thus decreasing NPC assembly efficiency.

4.2.5 Outlook

Next, I will investigate if ER retention and ER reflux phenotypes are indeed a result of newly synthesized and misfolded proteins; and if nucleoporin puncta-formation is only a result of misfolded nucleoporins stalling NPC assembly. As cycloheximide treatment would abolish the effect of ER stress, fluorescent tagged proteins under the galactose promoter have to be used. Initially, I will try and optimize this with Gas1 or Gas3, since their expression is already regulated by the *GAL* promoter. If I can establish an easy workflow, I will also tag and image proteins of the Golgi and the vacuole. Alternatively, an irreversible photoconvertible fluorescent protein can be used to endogenously tag my proteins such as moxDendra2 (*Kaberniuk et al., 2017*) or mEos3.2 (*Lajoie and Snapp, 2020; Sun et al., 2021*). Prior to treatment the fluorophores would be converted, so that old proteins have only the red state and new proteins the green state, enabling to distinguish between the two endogenous pools of protein.

Lastly, we identified several more proteins shifting away from mitochondria, which might derive from destabilization of translocases by altered lipid composition and decreased protein import of both membrane and soluble proteins (*Poveda-Huertes et al., 2021*). Part of the immense organellar remodeling were also proteins forming organelle contact sites, which mediate non-vesicular signaling between organelles and could be disrupted by misfolding or destabilization (*Voeltz et al., 2024*). These hits need further evaluation of their phenotype by microscopy.

By further understanding which components of the cell are affected during stress, I can define selectivity mechanisms of stress response pathways.

4.3 DOMs detect many potential new cargos for non-selective autophagy

Autophagy maintains cellular homeostasis by degrading unrequired proteins and organelles. Starvation-induced macroautophagy has been regarded as being non-selective and randomly sequestering cytosolic proteins, complexes and molecules. Several studies demonstrated that some cytosolic cargos are preferably degraded over others (*Makino et al., 2021; Isoda et al., 2024; Takeda et al., 2024*). This raised some new questions: (1) Are specific proteins and molecules selectively degraded? (2) Why does the cell degrade cargo proteins and molecules

both selectively and non-selectively (3) If there is selectivity during starvation-induced autophagy, how is it mediated?

To identify novel cargo proteins degraded by macroautophagy, I applied DOMs to nitrogen-starved cells. I identified roughly 200 proteins which significantly changed their localization upon starvation potentially by intact macroautophagy. Some of the identified hits are already known to be involved in autophagy (Table 2), either as core autophagy machinery (Atg1, Atg8), as cargos (Fas1, Fas2), as selective autophagy receptors (Atg19, Atg34, Hab1) or known to be affected by starvation such as ribosomal proteins and ribosomal regulatory factors or metabolic processes. Many of these identified proteins are not yet associated with non-selective autophagy or the regulatory mechanism has not yet been elucidated.

Nitrogen starvation quickly arrests rRNA processing and decreases ribosome protein expression via TORC1 inhibition (*Powers and Walter, 1999*) and activates degradation via autophagy (*Takeshige et al., 1992; Takeda et al., 2024*). I identified a few ribosomal subunits, ribosome assembly factors and RNA processing factors to not only be downregulated but also to significantly shift upon starvation only in cells with intact macroautophagy (Table 2). Even though I cannot exclude an upregulated ubiquitin-proteasome system or an altered cargo ubiquitylation pattern to enhance proteasomal degradation of that respective cargo protein. Since DOMs use normalized profiles of each replicate map, only the distribution of signal is taken into account and excludes abundance changes from the analysis, hence the predicted protein shifts are justified.

The ribophagy receptor Hab1 was the strongest hit to be predicted by MR analysis. Unfortunately, expression levels of Hab1 were so low that it was not detected in any WT and Δatg7 control replicate, and could neither perform cytosol shift analysis nor identify the steady-state localization to analyze the complete shift trajectory. Analysis of the neighborhood showed that Hab1 only correlated highly with Atg1, Atg3 and Atg8 in WT starved cells but did not correlate with any other selective autophagy receptors such as, Atg40 for ER-phagy, Atg39 mediating autophagy of the nuclear envelope (*Mochida et al., 2015*) or Atg19 and Atg34 mediating Cvt cargo transport (*Watanabe et al., 2010*). This indicates that also in my starvation maps Hab1 was sequestered in autophagosomes or located to the PAS in during starvation. Moreover, the other autophagic cargos Fas1 and Fas2 were highly correlating with only Hab1 but not Atg8 in WT starved maps. Besides these, the Hab1

neighborhood contained almost exclusively ribosomal proteins in starved Δatg7 cells, suggesting that it was indeed interacting with mature ribosomes (*Takeda et al., 2024*).
In WT cells excessive ribosomes are quickly degraded by the proteasome (*Sung et al., 2016*). Neighborhood analysis of the ribosomal hits revealed that indeed the ribophagy receptor Hab1 and also the HSP40 chaperone Zuo1 and HSP70 chaperone Ssz1 (*Gautschi et al., 2002*) are correlating in Δatg7 starved cells. Suggesting that ribophagy was blocked and the UPS had limited capacities (*Schmidt et al., 2019*), the ribosomal proteins which were still generated could potentially have aggregated (*Sung et al., 2016*). In these aggregates other ribosomal binding proteins could be accumulated as well, such as the ribophagy receptor Hab1 and the chaperones Zuo1 and Ssz1, which control translation (*Black et al., 2023*). This would also explain the sedimentation characteristics of Hab1 which were similar to ribosomal sedimentation.
It was striking that only two ribosomal proteins, Rpl37a and Rps3, were predicted to change their localization significantly and have a recovery of their cytosolic pool. These three ribosomal proteins do not share obvious properties, but it is known that different subunits form different heterogeneous ribosomes for translation of specific mRNAs, which are differentially regulated upon particular stresses (*Pietras et al., 2024; Wang et al., 2024*). Also some subunits have a different cellular function besides translation. (*Bhavsar et al., 2010*). (*Makino et al., 2021*) proposed that selected mRNAs coding for amino acid biogenesis and ribosomal proteins were degraded by autophagy. Surprisingly some of these mRNAs contained associated ribosomes, pointing towards a regulation of translation and autophagy at the RNA level. In order to find out if this proposed mechanism can be adapted to the few shifting ribosomal protein hits in my maps, ribosomal profiling needs to be performed.

Furthermore, among my 45 shifting hits of both MR analysis and cytosol shift analysis, were proteins involved amino acid synthesis, lipid synthesis and glycogen synthesis (Table 2). Thus, I propose that the components of these metabolic pathways are non-selectively cleared by macroautophagy upon nitrogen starvation to introduce an additional regulatory level.
Upon nitrogen starvation uncharged tRNAs are sensed and subsequently inhibit mRNA translation and induce the transcription factor Gcn4 (*Wek et al., 1995*). Active Gcn4 induces the expression of proteins that enable adaptation to nitrogen deprivation. The targeted genes are associated with pathways such as, amino acid metabolism, amino acid transporters and

components of the autophagy machinery (*Hinnebusch and Natarajan, 2002*). The three hits involved in amino acid biosynthesis are Gly1, involved in glycine synthesis (*Monschau et al., 1997*) and the S-adenosylmethionine (SAM) synthetases Sam1 and Sam2. SAM is a widely used cofactor and is used for methylation of proteins, RNAs and lipids (*Thomas and Surdin-Kerjan, 1997; Kodaki et al., 2003*). It has been described that upon nitrogen starvation glutamate synthesis is supported by the amino acids derived from protein turnover and maintains subsequent aspartate synthesis, which serves as hub for synthesis of nucleic acids and amino acids such as glycine (*Liu et al., 2021*). In my strains however, proteins are not degraded in the vacuole and hence the nitrogen to support amino acid synthesis is not available. This might target proteins involved in amino acid synthesis for degradation, which is impaired in my Δatg7 cells.

Another recently discovered cargo of non-selective autophagy is glycogen (glycophagy). Glycogen is synthesized during starvation, but prolonged starvation leads to transport and degradation in the vacuole by autophagy through the selective autophagy receptor Atg45 (*Isoda et al., 2024*). Two of the identified shifting proteins, Ugp1 and Psk2, are involved in synthesis and regulation of glycogen synthesis. Ugp1 catalyzes the last steps in glycogen synthesis (*Daran et al., 1995*) and Psk2 is a PAS-kinase which directly downregulates Ugp1 by phosphorylation (*Rutter et al., 2002*). Since Ugp1 produces storage carbohydrates, the protein levels are actively upregulated upon oxidative stress to ensure long-term survival (*Yi and Huh, 2015*). DOMs showed that the abundance of Ugp1 did not change in WT or Δatg7 cells upon stress, whereas Psk2 was downregulated. Unfortunately the proposed selective autophagy receptor Atg45 for Ugp1 was not detected in my maps, hence I need experimental validation if Ugp1 is also a target of glycophagy. Furthermore, SVMs predicted that Ugp1 is localized to the Golgi in WT cells upon starvation. Since UDP-glucose is a precursor for other molecules involved in N-glycosylation, cell wall synthesis, trehalose and glycogen synthesis the predicted shift of Ugp1 might be caused due to altered needs for synthesis of different molecules which affects spatial regulation of the enzyme itself.

Moreover, DOMs identified Fas1 and Fas2 to shift significantly in the starved maps. (*Shpilka et al., 2015; Jang et al., 2024*) demonstrated that upon TORC1 inhibition the fatty acid synthetase (FAS) is preferably degraded which is essential for cell survival upon prolonged

starvation. (*Jang et al., 2024*) showed that upon starvation in autophagy deficient cells FAS is degraded by ubiquitination-mediated proteasomal degradation mediated by the E3 Ligase Ubr1. Since I found another protein, Ipt1 responsible for sphingolipid synthesis, I suggest that similar to the FAS, other unexplored proteins associated with lipid metabolism are degraded by macroautophagy upon starvation.

In conclusion, I already detected many components of pathways known to be affected by autophagy but have not been characterized in the context of global cellular stress response to nitrogen-starvation. However, upon starvation not only macroautophagy is activated but other transport pathways towards the vacuole are still active and distinct forms of microautophagy which function independent of Atg8 are activated (*Schuck, 2020*). Therefore, I might only detect a large fraction but not all proteins which change their localization by macroautophagy.

In a recent publication (*Ginevskaia et al., 2024*) presented a detailed quantification of non-selective and selective autophagy activity of all Atg proteins (Atg1-Atg42) upon nitrogen-starvation. They found that in Δatg7 samples, the Cvt pathway, mitophagy and selective ER-phagy, similar to previous results (*Schafer et al., 2020*), were nearly or completely abolished. On the other hand, cytosolic cargo degradation (Pgk1), similar to previous results (*Muller et al., 2000*), and pexophagy were impaired but functional. Furthermore, in Δatg8 cells, autophagy of vacuolar membrane proteins was only slightly impaired (*Li et al., 2019; Rahman et al., 2018*).

All of these non-selective autophagy pathways are associated with general microautophagy (*Schuck, 2020*) , because additional knockout of ESCRT components abolished residual activity in most cases completely.

Due to the *Δpep4 Δprb1* mutation, degradation of cargo proteins is disabled in the vacuole and accumulated, thereby upscaling the native number of proteins and distorting results. Hence, the slight downregulation of most hits in the autophagy mutant upon starvation, points towards transcriptional downregulation rather than a massive compensatory activation of proteasomal degradation, since proteasomes were neither differentially regulated nor shifted significantly and it was reported that their activity is only slightly enhanced in autophagy-deficient cells but not in WT cells (*Athane et al., 2015*).

In order to evaluate the predicted results, the dual-color reporter, pHluorin-mCherry, will be fused to selected hits and imaged. Cargo proteins in the cytosol will have a fluorescent signal in both green and red channels. Once the protein is taken up into the acidic vacuole lumen, the pH sensitive green fluorescent pHluorin is quenched (*Miesenbock et al., 1998*), whereas mCherry stays fluorescent. Besides microscopy, GFP cleavage assays will be performed in using proteins tagged with GFP in a strain with intact vacuolar degradation. If the autophagic cargo is taken up into the vacuole, the GFP tag is cleaved off and can be detected by immunoblotting as a single 27 kDa band. Using several Atg mutants and ESCRT mutants, autophagic activity can be quantified similar to (*Ginevskaia et al., 2024*) and new cargo proteins verified.

On the basis of the list of old and potential new cargo proteins, I will design my ideal cargo protein abundance profile to perform neighborhood and organelle shift analyses. This profile will allow me to specifically find proteins which correlate with already known cargos affected by non-selective autophagy, such as Fas1 and Fas2. This might specify the data analysis to find more autophagic cargos and subsequently will enable me to further characterize the sorting mechanism of general macroautophagy and potentially microautophagy.

The proteins here described serve as starting point to experimentally evaluate if DOMs were able to detect starvation-induced non-selective macroautophagy cargos and will assist in answering the question how non-selective macroautophagy selects its cargos.

Furthermore, applying DOMs to microautophagy deficient cells might provide insights into these conserved but difficult to screen pathways to uncover new aspects in stress responses and to reevaluate the interplay and regulation of simultaneous active autophagic pathways.

4.4 Limitations of this technique

Since DOMs only work with crudely separated organelles, a specific localization prediction is not possible but limited to the classification groups. Moreover, the visualization of the organellar maps is very intuitive and also helpful to evaluate the quality of organelle separation and direction of shifts. However, reducing these multidimensional datasets to only two dimensions disregards parts of the information contained in the maps and further evaluation of hits should only be based on the statistical analyses.

The multiple analysis tools optimized by Georg Borner using my organellar maps, are nonetheless very powerful in predicting global localization changes such as localization

changes of single proteins, known complexes or whole organelles upon a respective treatment. But in some distinct cases the predictive power even extends to the suborganellar or subcomplex level as for the Rtn1 clusters and NPC segregation.

Furthermore, there might have been technical problems while generating organellar maps which subsequently resulted in less well-defined clusters. In order to generate profiles, I needed to homogenize my cells by which larger organelles, especially the vacuoles, were ruptured. The leakage of lumenal proteins into the cytosol fraction distorted the abundance profiles and complicated the starvation maps analysis. Reducing homogenization might keep organelles intact, but changing the homogenization will affect vesiculation of organelles, and hence the whole sedimentation behavior of the organelles. This would result in the necessity to laboriously optimize yeast DOMs again.

Another technical problem was that for each biological replicate, I lysed and homogenized all samples sequentially. Thus, some samples were consistently stored on ice much longer than the control samples prior to homogenization. If my cells were still intact prior to homogenizing, the protease inhibitors in the lysis buffer could not work properly. This potentially resulted in lysis of proteins in the cells, destabilization organelles and led to a different sedimentation behavior. This could in the end distort the organelle abundance profiles and complicate data analysis. Though, by evaluating some of the predicted hits experimentally, the data analysis can be tailored to the research question even utilizing the unrefined maps.

Ultimately, verification of the predicted shifts is usually performed using an imaging technique or by immunoblotting, since these are cheaper, faster and easier to learn, revoking the advantage of label-free and unbiased analysis.

All in all, the here described DOMs approach established in yeast is a valuable tool to investigate yet difficult to study pathways in a global context and thereby redefine our understanding of stress response pathways in eukaryotes and their physiological role to maintain cellular homeostasis.

5 MATERIALS AND METHODS

5.1 Materials

5.1.1 Chemicals and buffers

Table 3: Chemicals and reagents used in this study.

Name	Supplier	Catalogue number
Acetone	Sigma-Aldrich	32201-M
Acetonitrile, Optima	Fisher Scientific	10055454
Agar for bacteriology	NeoFroxx GmbH	2235GR100
Agarose	VWR Life Science	443666A
Ammonium hydroxide, 25%	Sigma	1.05428
cOmplete protease inhibitors (EDTA) free	Roche	04693132001
DNA stain G	Serva	39803.01
dNTPS	Thermo Fisher Scientific	R0181
DTT	Merck	10708984001
EDTA-free protease inhibitor cocktail	Sigma-Aldrich	04693159001
Ethylenediaminetetraacetic acid (EDTA)	AppliChem	A3553, 1000
GeneRuler 1kb Plus DNA ladder	Thermofisher Scientific	SM1332
Geneticin (G418)	Biochrom	A 2912
Glycerol	Riedel-de Haen	15523-1L
Glycine	Thermo Fisher Scientific	220910010
HEPES	Roth	9150.4
Hygromycin B	Sigma-Aldrich	31282-04-9
Iodoacetamide, >99%	Sigma	I1149-5G
Methanol, LC/MS grade	Fisher Scientific	10031094
$MgCl_2$	Merck	1.05833.0250
Milk powder	Roth	T145.2
NaCl	Fisher Scientific	231-598-3
NaOH	Sigma-Aldrich	30620-1KG-R
nitrocellulose membranes, 0.45 µm	Cytiva (Amersham)	10600007
Nourseothricin, clonNAT	Werner BioAgents	5.003.00
PageRuler Plus Prestained Protein ladder	Thermofisher Scientific	26619
Sodium dodecyl sulfate	Roth	2326.2
ß-estradiol	Sigma-Aldrich	E8875
Styrene-divinylbenzene reversed-phase sulfonate (SDB-RPS) solid-phase extraction material	VWR	66886-U
Trifluoroacetic acid for spectroscopy, >99%	Merck	Uvasol 1.08262
Tris base	Roth	4855.2
Tryptone/Peptone ex casein	Roth	8952.3
Tween-20	AppliChem	A1389, 1000
Urea	Sigma-Aldrich	33247-1KG

Water for chromatography (LC-MS Grade)	Merck	115333
Yeast extract	Roth	2363.3
Yeast Nitrogen Base without Amino acids and without Ammonium sulphate	Formedium	CYN0502

Table 4: Buffers and solutions used in this study.

Buffer/ solution	**Composition**
Acrylamide mix (30%, 37.5:1)	29.2% (w/v) acrylamide 0.8% (w/v) N,N'-myethylen-bisacrylamide
Agarose gel loading dye (5x)	50% (v/v) glycerol 10% (v/v) 10x TAE buffer 0.05% (w/v) Orange G
Amino acid mix	2% in water, autoclaved
Ammonium persulfate (APS)	10% (w/v) in water
Ampicillin	100 mg/mL in water
β-estradiol	10 mM in ethanol
Betaine	5 M in water containing 0.5% (w/v) Orange G
Blotting buffer	25 mM Tris 192 mM glycine 20% (v/v) techn. EtOH
Buffer A*	0.1% trifluoracetic acid 2% acetonitrile LC-MS grade water
Colony PCR buffer (10x)	200 mM Tris-HCl, pH 8.8 100 mM (NH4)2SO4 100 mM KCl 25 mM $MgCl_2$
Digestion buffer	50 mM Tris, pH 8.1 8 M Urea 1 mM DTT (freshly) LC-MS grade water
dNTPs	10 mM each; dATP, dGTP, dCTP, dTTP
Dithiothreitol (DTT)	1 M in water, sterile-filtered

Glucose (10x)	20% (w/v) in water, autoclaved
Iodoacetamide (10x)	550 mM iodoacetamide LC-MS grade water
Lithium acetate	1 M in water, sterile-filtered
Lysis buffer	25 mM Tris HCl, pH 7.5 200 mM sorbitol 1 mM EGTA 0.5 mM $MgCl_2$ 1 tablet cOmplete protease inhibitor per 50 ml
LysC stock solution (0.5 mg/ml)	100 µg lyophilized powder in 200 µl 50 mM Tris HCl, pH 8.1 LC-MS grade water
Polyethylene glycol (PEG) 3350	50% (w/v) in water, sterile-filtered
RPS-Elution buffer	1.25% ammonium hydroxide 80% acetonitrile LC-MS grade water
Salmon sperm DNA	10 mg/ml in water
Separating gel buffer	2 M Tris, pH 8.8
Spheroplast buffer	50 mM Tris HCl, pH 7.5 1 M Sorbitol 0.5 mM $MgCl_2$
Sodium dodecyl sulfate (SDS)	15% (w/v) in water
Stacking gel buffer	0.5 M Tris, pH 6.8
1x SDS resuspension buffer	50 mM Tris HCl, pH 8.1 2.5% SDS LC-MS grade water
5x SDS resuspension buffer	50 mM Tris HCl, pH 8.1 12.5% SDS LC-MS grade water
SDS-PAGE running buffer	25 mM Tris 0.1% (w/v) SDS 192 mM glycine

SDS-PAGE sample buffer (4x)	278 mM Tris, pH 6.8 44.4% (v/v) glycerol 4.4% (w/v) Lithium dodecyl sulfate (LDS) 0.02% (w/v) bromophenol blue 10 mM DTT (freshly to each sample)
TAE buffer (50x)	2 M Tris 1 M acetic acid 50 mM EDTA
TBS/Tween (TBS-T)	10 mM Tris, pH 7.4 150 mM NaCl 0.1% (v/v) Tween 20
Transformation mix	33% (w/v) PEG 3350 100 mM Lithium acetate 0.28 µg/mL salmon sperm DNA, freshly boiled before use
Trypsin stock solution (0.5 mg/ml)	100 µg lyophilized powder in 200 µl 50 mM Tris HCl, pH 8.1 LC-MS grade water
Tunicamycin (Tm)	1 mg/ml in DMSO
Yeast nitrogen base (YNB)	6.9% (w/v) in water, autoclaved
Yeast nitrogen base without ammonium sulfate	1.7% (w/v) in water, autoclaved

5.1.2 Growth media and plates

Table 5: Composition of synthetic complete amino acid mix.

Component	Amount
Adenine	0.5 g
Alanine, Arginine, Asparagine, Aspartic Acid, Cysteine, Glutamic acid, Glutamine, Glycine, Histidine, Inositol, Isoleucine, Lysine, Methionine, Phenylalanine, Proline, Serine, Threonine, Tryptophan, Uracil, Valine	2 g each
Leucine	4 g
Para-aminobenzoic acid	0.2

For selection plates (SC-His/ -Leu/ -Trp/ -Ura), the respective amino acid was excluded from the total amino acid mix.

Table 6: Growth media used for liquid culture of yeast and bacteria.

Medium	Composition
SCD	2% (w/v) glucose 0.69% (w/v) YNB 0.2% (w/v) amino acid mix
SD-N	2% (w/v) glucose 0.17% (w/v) YNB without ammonium sulfate
Buffered SCD	SCD medium 50 mM HEPES pH 7.5
YPD	1% (w/v) yeast extract 2% (w/v) peptone 2% (w/v) glucose
LB	1% (w/v) tryptone 0.5% (w/v) yeast extract 1% (w/v) NaCl
LB + amipicillin	1% (w/v) tryptone 0.5% (w/v) yeast extract 1% (w/v) NaCl 100 µg/mL ampicillin

Table 7: Plates used for growth and selection of yeast and bacteria.

Medium	Composition
SCD plates	2% (w/v) glucose 0.69% (w/v) YNB 0.2% (w/v) amino acid mix 2% (w/v) agar
YPD plates	1% (w/v) yeast extract 2% (w/v) peptone 2% (w/v) glucose 2% (w/v) agar
YPD G418 plates	1% (w/v) yeast extract 2% (w/v) peptone 2% (w/v) glucose 1% (w/v) agarose 20 µg/mL Geneticin (G418)
YPD hph plates	1% (w/v) yeast extract

	2% (w/v) peptone 2% (w/v) glucose 1% (w/v) agarose 100 µg/mL Hygromycin B
YPD nat plates	1% (w/v) yeast extract 2% (w/v) peptone 2% (w/v) glucose 1% (w/v) agarose 10 µg/mL Nourseothricin (ClonNat)
LB amipicillin plates	1% (w/v) tryptone 0.5% (w/v) yeast extract 1% (w/v) NaCl 2% (w/v) agar 100 µg/mL ampicillin

5.1.3 Enzymes and kits

Table 8: Enzymes used in this study.

Name	Supplier	Catalogue number
ALLin™ HiFi DNA Polymerase	highQu	HLE401c1
BssHII	NEB	R0199
DpnI	NEB	R0176
EcoRV	NEB	R0195
Opti Taq DNA Polymerase	Roboklon	E2600-02
PacI	NEB	R0547
Phusion DNA polymerase	NEB	M0530
Pierce™ Lys-C Protease, MS Grade	ThermoFisher Scientific	90307
Pierce™ Trypsin Protease, MS Grade	ThermoFisher	90058
PmeI	NEB	R0560
Q5 High-Fidelity DNA polymerase	NEB	M0491S
T4 DNA ligase	ThermoFisher Scientific	EL011
T5 exonuclease	NEB	M0663
Taq DNA ligase	NEB	M0208
Taq DNA Polymerase	Sigma-Aldrich	D1806
ZYMOLYASE 100T 1 * 25 mg	VWR	USBIZ1004-025

Table 9: Kits used in this study.

Name	Supplier	Catalogue number
miniBio Column DNA Gel and PCR Extraction Kit	miniBio Life Science Products	mB003

miniBio Column Plasmid Mini-Preps Kit	miniBio Life Science Products	mB001
Pierce™ Rapid Gold BCA Protein Assay Kit	ThermoFisher	A53225
SuperSignal™ West Pico PLUS Chemiluminescent Substrate	Thermo Scientific	34577

5.1.4 Antibodies

Table 10: Antibodies used for Immunoblotting.

Name	Host species	Dilution	Source	Catalogue number
Dpm1	mouse	1:10,000	Invitrogen	A-6429
Gas1	rabbit	1:5,000	Howard Riezman	n.a.
Kar2	rabbit	1:50,000	Peter Walter	n.a.
Pgk1	mouse	1:500,000	Abcam	ab113687
Pma1	mouse	1:5,000	Abcam	ab4645
Sec63	rabbit	1:10,000	Randy Schekman	n.a.
Vph1	mouse	1:20,000	Abcam	ab113683
anti-mouse HRP	goat	1:10,000	Pierce (Thermo Fisher Scientific)	31432
anti-rabbit HRP	goat	1:10,000	Pierce (Thermo Fisher Scientific)	31462

5.1.5 Equipment and software

Table 11: Equipment used in this study.

Name	Manufacturer
Bioruptor® Plus sonication device	Diagenode
Dounce homogenizer, 7 ml, tight pestle	Fisher Scientific
EASY-nLC 1200 ultra-high-pressure system	ThermoFisher Scientific
Evosep One LC	Evosep Biosystems
Heraeus Pico 17 centrifuge	Thermo Scientific
ImageQuant LAS 4000	GE Healthcare
Infinite F50 plate reader	Tecan
Infors HT Multitron incubator shaker	Infors HT Multitron incubator shaker
Magnetic stirrer MR 3001 K	Heidolph
Megafuge 16R	Thermo Scientific
microcentrifuge, refrigerated 5417 R	Eppendorf
NanoDrop ND-1000 Spectrophotometer	ThermoFisher Scientific
Optima™ MAX Ultracentrifuge	Beckman Coulter
Orbitrap Exploris 480 mass spectrometer	Thermo Fisher Scientific
PepSep column (15 cm length, 75 µm ID, 1.5 µm C18 beads	Bruker Daltonics
PepSep Emitter FS with Liquid Junction (10 µm ID)	Bruker Daltonics
PowerPac Basic power supply	Bio-Rad

ReproSil-Pur C18-AQ 1.9 µm silica beads	Dr. Maisch GmbH
Roller mixer RM5	CAT
syringe 16 gauge, blunt end, ID: 1.19 mm, OD: 1.65 mm	Hamilton
Syringe plunger 1702	Hamilton
Thermocycler T Professional Trio	Biometra
timsTOF HT mass spectrometer	Bruker Daltonics
TLA 110 ultracentrifuge rotor	Beckman Coulter
TLA 110, 3.2 mL, Open-Top Thickwall Polycarbonate Tube, 13 x 56mm	Beckman, 362305
Ultra low freezer	Sanyo
Vacuum concentrator plus	Eppendorf

Table 12: Software used in this study.

Name	**Version**	**Company**
Affinity Designer	2.6.0	Serif
DIA-NN software	1.8.1	(*Demichev et al., 2022*)
Endnote	21.5	EndNote
FIJI	2.16.0	http://imagej.org
FragPipe computational platform	22.0	(*Demichev et al., 2022*)
Java	1.8.0	
MaxQuant	2.0.1.0	(*Tyanova et al., 2016a*)
NIS Elements software	5.42.05	Nikon
Perseus	1.6.1.13; 1.6.2.3	(*Tyanova et al., 2016b*)
Python	3.9.20	https://www.python.org/
timsControl	5.1	Bruker Daltonics
Xcalibur software		Thermo Fisher Scientific

5.2 Molecular biology methods

5.2.1 Plasmids

Table 13: Plasmids used in this study.

Plasmid	Alias	Source
pFA6a-mCherry-kanMX6	pSS061	Greg Tully
pFA6a-mNeonGreen-HIS3	pSS447	(*Papagiannidis et al., 2021*)
pFA6a-sfGFP-scTRP1	pSS424	Tamas Szoradi
pFA6a-cherry-klTRP1	pSS880	Katharina Schaeff
pFA6a-sfGFP-klTRP1	pSS1499	this study
pFA6a-mScarlet-i3-HIS3	pSS1421	Sebastian Schuck
pFA6a-mScarlet-i3-klTRP1	pSS1426	Sebastian Schuck
pFA6a-Halo-klTRP1	pSS1411	Sebastian Schuck
pFA6a-nat-P_{CYC}-yeGFP	pSS1066	(*Janke et al., 2004*)
pRS406-P_{GPD}-mCherry-Ubc6	pSS117	Benoit Kornmann
pRS406-P_{TEF}-TagBFP-Ubc6	pSS988	Sebastian Schuck
pFA6a-hph-P_{GPD}-Kar2ss-cherry	pSS485	Katharina Schaeff
pRS405-P_{GAL}-Kar2ss-sfGFP-HDEL	pSS1223	Carlos Martin de Hijas
pFA6a-hph-P_{GAL}-Kar2ss-sfGFP	pSS1367	this study
pNH605-P_{ADH}-GEM(Gal4DBD-EstR-Msn2TAD)	pDEP151	David Pincus
pNH605-P_{ADH}-GEM-P_{GAL}	pSS474	(*Schmidt et al., 2019*)
pNH605-P_{ADH}-GEM-P_{GAL}-NLS-neon-T_{CYC}	pSS1563	this study

5.2.2 Oligonucleotides

Table 14: Oligonucleotides used in this study. Oligonucleotides were purchased either from Integrated DNA Technologies (IDT) or Sigma-Aldrich. 100 µM stock solutions were prepared in water. Oligonucleotides for tagging and deletion of genes in *S. cerevisiae* were designed according to (*Longtine et al., 1998*) and (*Janke et al., 2004*) and are not listed in the table below.

Name	Sequence	Source
485 hom. GAL fwd	cctgttgtaatcgagctcagACGGATTAGAAGCCG CCGA	this study
485 hom. sfGFP rev	gaattctctgtcggaccagccttATACAATTCATCCA TACCG	this study
485 open fwd	gctggtccgacagagaattc	this study
485 open rev	ctgagctcgattacaacagg	this study
NLS-neon 474 Insert fwd	atgccaccaaaaaaaaaaagaaaagttaccggtGTTT CTAAGGGTGAAGAAGAC	this study
NLS-neon 474 Insert rev	gaattcctgcagcccgggggTTACTTGTACAATTCG TCCATACC	this study

pSS474 open Gibson fwd	CCCCCGGGCTGCAGGAAT	this study
pSS474 open Gibson rev	cttttttttttttggtggcatATCCACTAGTTCTAGAAT CCGGGGTTTTTTCTC	this study

5.2.3 Agarose gel electrophoresis

A 1% agarose gel was prepared by dissolving 1% agarose (w/v) in 2x TAE buffer, while maintaining a constant volume. I mixed 35 ml of liquid agarose with 0.7 µl of Stain G and poured it in a casting tray with a well comb attached. The PCR sample was mixed with 5x loading dye to 1x final concentration and loaded into wells. GeneRuler 1kb Plus DNA ladder was used as size reference. Electrophoresis was operated at 100 V for 20 min, DNA bands were imaged using a UV irradiator.

5.2.4 Bacterial transformation

Chemically competent *E. coli* (DH5α) were thawed on ice, plasmid added to 100 µl competent cells and incubated on ice for 10 min. Then cells were subjected to heat shock for 60 s at 42°C and incubated on ice again for 5 min. I added 900 µl of LB medium, followed by 1 h incubation at 37°C and 750 rpm in a ThermoMixer. I centrifuged bacteria at 10,000 g for 1 min, discarded 900 µl medium, resuspended bacteria in the residual volume, plated on a selective plate containing the appropriate antibiotic and incubated overnight at 37°C.

5.2.5 Molecular cloning

Plasmids used in this study are listed in Table 13 and oligonucleotides used for plasmid generation are listed in Table 14.

DNA fragments and vectors were amplified by polymerase chain reaction (PCR) using OptiTaq, ALLin HiFi or Q5 HF polymerase according to manufacturer's instructions. For long range PCR I used Q5 HF polymerase and increased the elongation time to 50s per kb and 0.3°C increase of the annealing temperature per cycle, starting from 60°C. Parental DNA templates were degraded by DpnI digestion for 1h at 37°C and heat inactivation for 20 min at 65°C. PCR products were either directly purified using the DNA gel and PCR extraction kit according to

the manufacturer's instructions or separated by electrophoresis on a 1% agarose gel and the correct PCR product was excised and purified using the mentioned kit.

Vectors which were not linearized by PCR, were digested for 1h at 37°C followed by heat inactivation at 65°C or 80°C for 20 min, according to New England Biolabs. PCR products were ligated with T4 DNA ligase reaction according to the manufacturer's instructions or by Gibson assembly. Gibson assembly reaction was prepared according to (*Gibson et al., 2009*). Reaction was incubated at 50°C for 1 h. I transformed 1 µl assembly or ligation reaction using competent *E. coli* DH5α cells. A single colony was inoculated in LB medium supplemented with the appropriate antibiotic and grown overnight at 37°C. Plasmids were isolated using the Mini-Prep kit and sequence was verified by Sanger sequencing by Microsynth Seqlab.

I generated pFA6a-sfGFP-klTRP1 (pSS1499), by inserting sfGFP of pFA6a-sfGFP-scTRP1 (pSS424), generated by Tamás Szórádi, into pFA6a-cherry-klTRP1 (pSS880), generated by Katharina Schaeff. For tagging of GPI-anchored proteins after their natural N-terminal signal sequence, I generated pFA6a-hph-P_{GAL}-Kar2ss-sfGFP (pSS1367) by amplifying PGAL-Kar2ss-sfGFP from pFA6a-hph-P_{GAL}-Kar2ss-sfGFP (pSS1223), generated by Carlos Martín de Hijas, and inserting it into pFA6a-hph-P_{GPD}-Kar2ss-cherry (pSS485), generated by Katharina Schaeff, using Gibson assembly. I generated pNH605-P_{ADH}-GEM-P_{GAL}-NLS-neon-T_{CYC} by amplifying the mNeonGreen sequence from pFA6a-mNeonGreen-HIS3 with an additional N-terminal nuclear localization sequence from Simian-Virus 40 and inserted the PCR product into pNH605-P_{ADH}-GEM-P_{GAL} by Gibson assembly.

pNH605 plasmids were digested with PmeI prior to yeast transformation. pRS406 plasmids were digested with EcoRV prior to yeast transformation.

5.3 Yeast methods

5.3.1 Yeast strains

Table 15: Yeast strains used in this study. Strains were derived from *S. cerevisiae* W303 mating type a. Neon, mNeonGreen; sfGFP, superfolder GFP; yeGFP, yeast-enhanced GFP; Kar2ss, Kar2 signal sequence; BFP, TagBFP; GEM, Gal4DBD-EstR-Msn2TAD.

Strain	Relevant genotype	Source
SSY122	*ADE2 leu2-3,112 trp1-1 ura3-1 his3-11,15 MATa*	(*Szoradi et al., 2018*)
SSY4076	*ura3::P_{GPD}-mCherry-Ubc6-URA3 Prc1-Neon::HIS3*	this study
SSY4356	*Sec63-mScarlet-i3::HIS3 Ero1-sfGFP::TRP1*	this study
SSY4402	*Sec63-mScarlet-i3::HIS3 Cpr5-sfGFP-HDEL::hph*	this study
SSY4403	*Sec63-mScarlet-i3::HIS3 Sil1-sfGFP-HDEL::hph*	this study
SSY4404	*Sec63-mScarlet-i3::HIS3 Pdi1-sfGFP-HDEL::hph*	this study
SSY1107	*Sec63-Neon::HIS3 KAR2-mCherry-HDEL::hph*	this study, Sebastian Schuck
SSY4355	*Rtn1-mCherry:kan P_{CYC1}-yeGFP-Dpm1::nat Yop1-Halo::TRP1 ura3::P_{TEF}-BFP-Ubc6-URA3*	this study, Klára Odehnalová
SSY4220	*Sec63-mScarlet-i3::HIS3 Prc1-sfGFP::scTRP1*	this study
SSY4278	*Sec63-mScarlet-i3::HIS3 Pep1-sfGFP::kITRP1*	this study
SSY4279	*Sec63-mScarlet-i3::HIS3 Atg42-sfGFP::kITRP1*	this study
SSY4257	*Sec63-mScarlet-i3::HIS3 Kre2-sfGFP::kITRP1*	this study
SSY4259	*Sec63-mScarlet-i3::HIS3 Mnn2-sfGFP::kITRP1*	this study
SSY4260	*Sec63-mScarlet-i3::HIS3 Mnn5-sfGFP::kITRP1*	this study
SSY4394	*Sec63-mScarlet-i3::HIS3 Aur1-sfGFP::kITRP1*	this study
SSY4251	*Sec63-Scarlet::HIS3 leu2::P_{ADH}-GEM-LEU2*	this study
SSY4280	*Sec63-mScarlet-i3::HIS3 leu2::GEM-LEU2 P_{GAL}-Kar2ss-sfGFP-GAS3::hph*	this study
SSY4281	*Sec63-mScarlet-i3::HIS3 leu2::GEM-LEU2 P_{GAL}-Kar2ss-sfGFP-GAS1::hph*	this study
SSY4283	*Sec63-mScarlet-i3::HIS3 leu2::GEM-LEU2 P_{GAL}-Kar2ss-sfGFP-UTR2::hph*	this study
SSY1212	*ura3::P_{GPD}-mCherry-Ubc6-URA3*	Jasmin Schäfer

SSY3788	*ura3::P_{GPD}-mCherry-Ubc6-URA3 Pom152-Neon::HIS3*	this study
SSY3789	*ura3::P_{GPD}-mCherry-Ubc6-URA3 Nup170-Neon::HIS3*	this study
SSY3790	*ura3::P_{GPD}-mCherry-Ubc6-URA3 Nup159-Neon::HIS3*	this study
SSY3791	*ura3::P_{GPD}-mCherry -Ubc6-URA3 Nup133-Neon::HIS3*	this study
SSY3792	*ura3::P_{GPD}-mCherry -Ubc6-URA3 Nup57-Neon::HIS3*	this study
SSY3793	*ura3::P_{GPD}-mCherry -Ubc6-URA3 Nic96-Neon::HIS3*	this study
SSY3794	*ura3::P_{GPD}-mCherry -Ubc6-URA3 Nup1-Neon::HIS3*	this study
SSY3885	*ura3::P_{GPD}-mCherry -Ubc6-URA3 Nup82-Neon::HIS3*	this study
SSY3886	*ura3::P_{GPD}-mCherry -Ubc6-URA3 Nup116-Neon::HIS3*	this study
SSY3980	*ura3::P_{GPD}-mCherry -Ubc6-URA3 Nup49-Neon::HIS3*	this study
SSY3981	*ura3::P_{GPD}-mCherry -Ubc6-URA3 Nsp1-Neon::HIS3*	this study
SSY4071	*ura3::P_{GPD}-mCherry -Ubc6-URA3 Nup42-Neon::HIS3*	this study
SSY4072	*ura3::P_{GPD}-mCherry -Ubc6-URA3 Gle1-Neon::HIS3*	this study
SSY4073	*ura3::P_{GPD}-mCherry -Ubc6-URA3 Gle2-Neon::HIS3*	this study
SSY4074	*ura3::P_{GPD}-mCherry -Ubc6-URA3 Dyn2-Neon::HIS3*	this study
SSY4129	*ura3::P_{GPD}-mCherry -Ubc6-URA3 Nup100-Neon::HIS3*	this study
SSY4410	*ura3:: P_{GPD}-mCherry-Ubc6-URA3 Nup157-Neon::HIS3*	this study
SSY4411	*ura3:: P_{GPD}-mCherry-Ubc6-URA3 Nup59-Neon::HIS3*	this study
SSY4413	*ura3:: P_{GPD}-mCherry-Ubc6-URA3 Ndc1-Neon::HIS3*	this study
SSY4414	*ura3:: P_{GPD}-mCherry-Ubc6-URA3 Nup53-Neon::HIS3*	this study
SSY4415	*ura3:: P_{GPD}-mCherry-Ubc6-URA3 Pom34-Neon::HIS3*	this study
SSY4418	*ura3:: P_{GPD}-mCherry-Ubc6-URA3 Nup188-Neon::HIS3*	this study
SSY4419	*ura3:: P_{GPD}-mCherry-Ubc6-URA3 Nup84-Neon::HIS3*	this study
SSY4420	*ura3:: P_{GPD}-mCherry-Ubc6-URA3 Nup120-Neon::HIS3*	this study
SSY4421	*ura3:: P_{GPD}-mCherry-Ubc6-URA3 Mlp2-Neon::HIS3*	this study
SSY4446	*ura3:: P_{GPD}-mCherry-Ubc6-URA3 Nup192-Neon::HIS3*	this study
SSY4456	*ura3:: P_{GPD}-mCherry-Ubc6-URA3 Nup85-Neon::HIS3*	this study
SSY4457	*ura3:: P_{GPD}-mCherry-Ubc6-URA3 Nup2-Neon::HIS3*	this study
SSY4458	*ura3:: P_{GPD}-mCherry-Ubc6-URA3 Nup60-Neon::HIS3*	this study
SSY4459	*ura3:: P_{GPD}-mCherry-Ubc6-URA3 Mlp1-Neon::HIS3*	this study
SSY4463	*ura3:: P_{GPD}-mCherry-Ubc6-URA3 Nup145C-Neon::HIS3*	this study

SSY4293	*ura3::P_{GPD}-mCherry-Ubc6-URA3 Kap95-Neon::HIS3*	this study
SSY4464	*ura3:: P_{GPD}-mCherry-Ubc6-URA3 Srp1-Neon::HIS3*	this study
SSY4444	*ura3:: P_{GPD}-mCherry-Ubc6-URA3 Nup116-Neon::HIS3 Kap95-Halo::TRP1*	this study
SSY4574	*his3:: P_{GPD}-BFP-hph leu2:: P_{GAL}-NLS-Neon-T_{CYC} P_{ADH}-GEM-LEU2 Pus1-Scarlet::klTRP1*	this study
SSY60	*Δpep4::TRP1 Δprb1::HIS3*	Sebastian Schuck
SSY61	*Δpep4::TRP1 Δprb1::HIS3 Δatg7:hph*	Sebastian Schuck

Yeast strains in this study were generated based on the PCR-based tagging method described in (*Janke et al., 2004*).

5.3.2 Yeast growth conditions and stress induction

I diluted yeast cells, less than 2 weeks old, into 5 ml SCD medium, incubated the cultures for 6h at 30°, 185 rpm shaking. In the evening, I diluted cultures freshly into SCD medium to ensure that after 16h incubation they were growing in early log phase. For yeast transformations, cells were cultured in YPD medium.

Cells expressing endogenous proteins under the estradiol-inducible GAL4DBD-EstR-Msn2TAD (GEM) *GAL* promoter, were cultured in the presence of 50 nM estradiol at all times.

To induce ER stress, I freshly diluted overnight cultures in SCD medium so that after 2 h they had an OD_{600} = 0.5 and added 8 mM DTT or 2 µg/ ml Tm. For nitrogen starvation I harvested 10 ODs for control or 120 ODs for starved cells, washed them once with the same volume of water and diluted them in the same volume of SCD for control or SD-N medium for starvation and incubated cultures for 6h.

5.3.3 Yeast transformation

Yeast strains were transformed based on the method by (*Ito et al., 1983*). Yeast cells were grown in YPD medium at 30°C overnight either so that they reached an OD_{600} = 1 after 16 h or until saturation and I diluted the culture 1:25 in fresh YPD and incubated for 4 h it so that the cells reached an OD_{600} = 1. Cells were harvested by centrifugation for 5 min at 3,000 g, the supernatant was removed, washed with 1 ml water, centrifuged for 2 min at 10,000 g. 10% of the PCR volume (about 0.5 µg DNA) was added, cells were resuspended in 360 µl

transformation mix (Table 4) and subjected to heat shock for 40 min at 42°C. Cells were centrifuged and resuspended in 1 ml YPD. If the transformed plasmid contained an antibiotic resistance gene, cells were recovered for three to six hours at 30°C shaking. 100 µl of the cell suspension were plated on selective plates and incubated for 2 days at 30°C. Single colonies were evaluated for successful integration by colony PCR and further restreaked on fresh selective plates.

5.3.4 Colony PCR

To confirm genetic modification of yeast strains, a fraction of single colonies were picked and resuspended in 40 µl colony PCR mix in 0.5 ml PCR strips. PCR mix with additional 500 mM final concentration of betaine was prepared and performed according to the Taq polymerase manufacturer's instructions. Next, 8 µl PCR product was loaded on a 1% agarose gel, operated and imaged as described in 5.2.3.

5.3.5 Light microscopy

Widefield microscopy images were acquired with the Nikon Ti2 microscope with a PLAN APO 100x/1.45 objective (Nikon) and an Orca Fusion-BT camera (Hamamatsu) from lab of Sebastian Schuck. Confocal microscopy images were acquired with a Nikon Ti2-W1 spinning disk confocal microscope equipped with a Yokogama W1 scanhead, a Nikon Plan Apo 100x/NA 1.45 objective and a Zyla 4.2P CMOS camera from the Nikon Imaging Center at the University of Heidelberg.

Overnight cultures were prepared as described in 5.3.2. Prior to any treatment, I diluted cells into 1.2 ml SCD medium in deep well plates and incubated the plates at 30 °C, at 185 rpm shaking. Estradiol-inducible ss-sfGFP-GPI-APs were diluted in buffered SCD medium with 50 nM estradiol. I harvested cells from 1 ml of cell suspension by centrifugation at room temperature for 2min at 10,000 g, removed the supernatant and resuspended cells in the residual medium. Proteins expressing a HaloTag, were stained with the silicon-rhodamine HaloTag ligand (*Lukinavicius et al., 2013*). After harvesting, I removed the supernatant completely and resuspended the cells in 30 µl PBS containing 500 nM HaloTag ligand. Cells were incubated for 10 min shaking at 800 rpm. Agarose pads were generated by dissolving 1% agarose (w/v) in SCD medium, pouring the mixture onto object slides and let it cool down.

Agarose pads for GPI-APs were made with PBS instead of SCD medium. 3 µl cell suspension was pipetted onto a coverslip and immediately covered with an agarose pad. For deconvolution I acquired images at the widefield microscope with multiple z slices (z-stacks) with a step size of 200 nm. At the confocal microscope I acquired single slices.

5.3.6 Imaging of the mNeonGreen library

The mNeonGreen library was kindly provided by the lab of Michael Knop at the Zentrum für Molekularbiologie (ZMBH) of Heidelberg University (*Meurer et al., 2018*).

Cells were cultured as described in 5.3.2. To induce ER stress, I freshly diluted overnight culture in SCD to OD_{600}=0.15, 0.3, 0.2 and did not treat, added 8 mM DTT, added 5 µg/ml Tm, respectively. After 2.5h incubation I prepared samples for microscopy as described in 5.3.3.

On the widefield microscope I acquired 2 fields of view with 7 z-stacks and 200 µm spacing in the Neon channel and brightfield.

I evaluated the phenotypes manually and consulted Sebastian Schuck in cases where the phenotype was not distinctive.

5.3.7 Image processing and analysis

All images which were not subjected to deconvolution, were background subtracted in FIJI software using the rolling ball method with 50 pixel radius. Images were deconvolved with the NIS Elements software using the Richardson-Lucy algorithm (30 iterations, automatic noise level detection, automatic background subtraction).

I manually adjusted images to the same display range, deviating from the ideal display range, to be able to compare phenotypes of different conditions. When expression levels differed too much between conditions, ideal display ranges were used, as indicated.

ER stress induced nucleoporin puncta-forming phenotypes were evaluated manually by Sebastian Schuck and me individually and results combined. To avoid bias, initially the ImageJ plugin “Blind Analysis Tools” was applied to randomize file names.

5.3.8 Nuclear import assay

Yeast cells (SSY4574), expressing NLS-mNeonGreen under the *GAL* promoter, were cultured as described in 5.3.2. I diluted cells to OD_{600} = 0.15 and not treated or OD_{600} = 0.25 and 8 mM DTT added. After 1 h growth I split each culture in two new tubes and added 500 nM estradiol to one culture each and further incubated. At 25 min, 40 min, 55 min after addition of estradiol I harvested 1 ml of culture by centrifugation at room temperature, at 10,000 g for 2 min. The remaining culture was incubated again. Cells were resuspended in 20 µl remaining medium, 3 µl mounted on coverslips and covered with 1% (w/v) agarose pad.

I prepared microscopy samples of each culture as described in 5.3.3. and I acquired 3 fields of view, single slice images acquired using a Nikon Ti2 microscope with a PLAN APO 100x/1.45 objective (Nikon) and an Orca Fusion-BT camera (Hamamatsu). Cultures were imaged over time to determine: (1) control mNeonGreen signal (untreated, NLS-neon expression); (2) DTT mNeonGreen signal (DTT, NLS-neon expression); (3) control mNeonGreen background autofluorescence (untreated, no expression); (4) DTT mNeonGreen background autofluorescence (untreated, no expression).

Images were quantified with FIJI software using a self-developed macro for semi-automated image quantification. Calculations and generation of plots were performed with a self-developed python script for automated data analysis. For each condition and timepoint I analyzed >400 cells from three biological replicates, as indicated in the figure legend.

The background was subtracted from each image in all channels, using the rolling ball method with a radius of 150 pixels. BFP and brightfield channels were combined, an automatic threshold defined based on global pixel intensity (Moments algorithm), objects segmented using the watershed algorithm and a cell mask generated for each individual image. Using the Pus1-mScarlet channel of each image a matching nucleus mask was generated in the same way. For segmented cells with a size between 9 and 27 µm2 and a circularity between 0.5 and 1, areas, mean mNeonGreen pixel intensities and mean BFP pixel intensities were determined. Similar measurements were performed for segmented nuclei with a size between 1.1 and 7 µm2 and a circularity between 0.1 and 1 and assigned to the respective cell measurements using the python script. Only cells with exactly one measured nucleus were further processed. Subsequent background correction was only performed for mNeonGreen signals, since autofluorescence of cytosolic BFP was neglectable. I first determined the overall mean cell and nucleus NLS-mNeonGreen background pixel intensities (samples 3, 4) for each condition and

timepoint. Then I subtracted these values from each individual cell and nucleus pixel intensities of NLS-mNeonGreen expressing cells (samples 1, 2) and removed cells with background-corrected pixel intensities <1 and its corresponding nucleus. With the remaining cell and nucleus background corrected pixel intensities I calculated nuclear enrichment by dividing the nucleus pixel intensity by the cell pixel intensity for each individual cell.

5.4 Biochemistry methods

5.4.1 Protein determination

Protein determination was performed with a BCA assay according to the manufacturer's instructions. In a 96-well flat bottom plate 10 µl of a BSA standard dilution series (0 to 2 mg/ml) was prepared in duplicates. 10 µl of each sample was diluted with 40 µl water, mixed gently and 10 µl transferred to a new well in triplicates. 200 µl of already combined BCA reagents were added and gently mixed by pipetting, plate was incubated for 10 min at room temperature, absorbance was measured at 480 nm using a plate reader. A standard curve was calculated based on the BSA absorbance and sample concentrations were determined. The median was used for further calculations.

5.4.2 Sodium dodecyl sulfate polyacrylamide gel electrophoresis (SDS-PAGE)

SDS-PAGE was used for protein analysis. Samples were diluted to the same protein amount with lysis buffer. 4x SDS-PAGE sample buffer was added to 1x final concentration and 10 mM DTT final concentration was added. Samples were loaded on 10% Tris-Glycine SDS gels. Prestained protein ladder was used as a size marker. The Bio-Rad systems were operated in SDS running buffer at 200 V until the running front reached the bottom of the separating gel.

5.4.3 Immunoblot

SDS-PAGE gels were rinsed once in blotting buffer and transferred onto a nitrocellulose membrane using the wet electroblotting system in cold transfer buffer at 400 mA for 90 min. After the transfer the membranes were rinsed with TBS-T, blocked in TBS-T with 5% nonfat dry milk for 1 h at room temperature before incubating with antigen-specific primary antibodies in 5% milk/TBS-T overnight rotating at 4°C. Then membranes were washed three times with TBS-T for 5 min and incubated for 1 h at room temperature with species-specific horseradish peroxidase (HRP)-conjugated secondary antibodies in 5% milk/TBS-T at dilutions listed in Table 10. Membranes were washed again three times with TBS-T for 5 min. To activate chemiluminescence SuperSignalTM West Pico PLUS substrate was added according to the manufacturer's instructions and membrane incubated for 5 min in the dark. Signal was

detected using the ImageQuant LAS 4000 imaging system. Editing of the images was done with FIJI software.

5.5 Dynamic Organellar Maps

I adapted and optimized this method for yeast, based on the protocol provided by (*Itzhak et al., 2019*).

5.5.1 Growth and stress induction

For reference and ER stress maps, I cultured WT yeast cells (SSY122) not older than 2 weeks in SCD at 30°C shaking so that they reach early log phase OD_{600}=0.5 after 14h. For starvation maps I cultured yeast cells (SSY060, SSY061) as described.

I generated 6 reference maps with unperturbed WT cells, as technical duplicates on 3 different days. I harvested 200 ODs per replicate (400 ml, OD_{600}=0.5) by centrifugation for 5 min at 3,000 g at room temperature. For ER stress maps, I prepared new 400 ml cultures and diluted them to (1) OD_{600}=0.1 and incubated it for 3h; (2) OD_{600}=0.15, incubated it for 1 h, then added 8 mM DTT and incubated for 2 h; OD_{600}=0.2 added 2 µg/ml Tm and incubated it for 3h. After 3h incubation times all cultures were harvested by centrifugation.

For starvation maps, I pelleted 10 ODs for control and 120 ODs for starved replicate by centrifugation, resuspended the pellet in the same volume of water and pelleted again by centrifugation. Each culture was resuspended in 400 ml SCD as control or SD-N for starvation, incubated for 6h and harvested by centrifugation.

5.5.2 Spheroplasting and cell lysis

Harvested cells were resuspended in 10 ml spheroplast buffer, 40 µl zymolyase T100 added and the cell suspension incubated at 30°C for 20 min with occasional inverting. Cell wall removal was monitored by measuring the OD of an aliquot diluted 1:40 in water every 10 min. After the OD decreased by 70%, spheroplasts were stored on ice. I washed the spheroplasts a total of 3 times by pelleting for 2 min at 1,000g at 4°C and gently resuspending in 5 ml cold spheroplast buffer. I resuspended the washed spheroplasts in lysis buffer, adjusted to a total volume of 4 ml and homogenized them by 20 strokes in a Dounce homogenizer. 50 µl of each homogenate was collected, resuspended in 1:4 5x SDS buffer and used as full proteome sample.

5.5.3 Fractionation

All subsequent steps are performed at 4°C. Homogenates were transferred to a 15 ml conical tube and unbroken cells removed by a clearing spin for 5 min at 300g. I transferred the supernatant to a new 15 ml conical tube and centrifuged for 10 min at 1,000 g. I transferred the supernatant to a new 15 ml conical tube and kept the 1,000 g pellet (1k pellet) on ice. I centrifuged for 10 min at 3,000g. I transferred the new supernatant to a TLA-110 compatible ultracentrifuge tube and centrifuged for 15 min at 6,000 g. This process was repeated three more times for 20 min, 20 min and 30 min at 12,000 g, 24,000 g and 78,000 g, respectively. The 3k, 6k, 12k, 24k and 78k pellets were kept on ice. 800 µl of the 78k supernatant, referred to as cytosolic fraction, was transferred to a 1 ml tube and mixed with 200 µl of 5x SDS resuspension buffer.

I resuspended all pellets in 1x SDS resuspension buffer with adjusted volumes to obtain concentrations higher than 1 µg/µl: 1k fraction 200 µl; 3k to 24k fraction 100 µl; 78k fraction 150 µl. Samples were incubated for 3 min at 65°C. Since the 1k sample contained the majority of DNA I further solubilized it by sonication with a Bioruptor for 15 cycles 30 s on/off at maximum intensity.

I added 0.1 mM DTT to a final concentration to all samples before flash freezing in liquid nitrogen and storage at -80°C.

5.5.4 Generation of tryptic peptides for mass spectrometry

I determined protein concentrations as described in 5.4.1 and diluted my samples with 1x SDS buffer to 1 µg/µl in 50 µl total volume. To precipitate proteins, I added 5 volumes of ice-cold acetone, mixed well and incubated at -20°C for 1 h. Samples were centrifuged for 5 min at 10,000 g at 4°C, the supernatant removed and pellets air dried for 5 min. I resuspended the pellets in 50 µl freshly made digestion buffer and incubated them at room temperature for 30 min to reduce disulfide bonds. Iodoacetamide was diluted to a final concentration of 55 mM in digestion buffer, 5 µl added to each sample and between 20 to 60 min incubated in the dark to alkylate cysteines. 2 µl of 0.5 µg/µl LysC stock solution were added, tubes inverted and incubated overnight at room temperature.

I added 171 µl of 50 mM Tris HCl, pH 8.1 and added 2 µl of 0.5 µg/µl trypsin stock solution. After gentle mixing, I incubated the samples for 3h at room temperature. Meanwhile, I

prepared Stop and Go Extraction (STAGE) tips by punching out circles of two overlaid SDB-RPS membranes and forcing them into a 200 µl tip using the blunt end needle with a matching plunger (Hamilton). STAGE tips were equilibrated with a series of washes of 100 µl acetonitrile, 100 µl 1% acetonitrile + 30% methanol, 100 µl 0.2 trifluoracetic acid.

Digested samples were acidified with 25 µl 10% trifluoracetic acid, incubated for 10 min on ice, centrifugated for 5 min at 4°C. 50.6 µl of the supernatant (equal to 10 µg peptides) was loaded onto the STAGE tips and washed with 100 µl isopropanol and 100 µl 0.2% TFA. Purified peptides were eluted with 60 µl freshly prepared elution buffer and into PCR tubes. Using a vacuum Concentrator plus (aqueous settings, 30°C) the sample volume was reduced to less than 5 µl. I resuspended samples in 10 µl Buffer A*, determined the concentrations with a NanoDrop 1000 spectrophotometer and adjusted the concentrations to 150 ng/µl. Acidified peptides and purified peptides were flash frozen in liquid nitrogen and stores at -80°C until further use.

5.5.5 Mass spectrometry acquisition

Reference maps and ER stress maps:

“Mass spectrometric measurements were done with data-dependent acquisition (DDA) (Schessner et al, 2023). Nanoflow reversed-phase chromatography was performed with an EASY-nLC 1200 ultra-high-pressure system coupled to an Orbitrap Exploris 480 mass spectrometer via a nano-electrospray ion source (Thermo Fisher Scientific). A binary buffer system with mobile phases A (0.1% v/v formic acid) and B (80% acetonitrile, 0.1% v/v formic acid) was used. Peptides were separated in 110 min on a 50 cm × 75 µm (i.d.) column, packed in-house with ReproSil-Pur C18-AQ 1.9 µm silica beads (Dr. Maisch GmbH). The column was operated at 60°C. Purified peptides were loaded onto the column in buffer A and eluted with a linear 5 - 30% gradient of buffer B, followed by washout and column re-equilibration. The mass spectrometer was controlled by Xcalibur software (Thermo Fisher Scientific) and operated in top 15 scan mode with a full scan range of 300 - 1650 Th. Survey scans were acquired at 60,000 resolution, with automatic gain control (AGC) set to 300% and a maximum ion injection time of 25 ms. Charge states were filtered for 2 - 5. Precursor ions were isolated in a window of 1.4 Th, fragmented by higher-energy collisional dissociation with normalized collision energies of 30%. Fragment scans were performed at 15,000 resolution with a

maximum injection time of 28 ms, AGC set to 100% and a dynamic precursor exclusion for 30 s." Platzek et al., *bioRxiv*:2025.2002.2021.639471. (2025) (*Platzek et al., 2025*)

Starvation maps:

An Evosep One LC system was used to carry out nanoflow reversed-phase chromatography, which was coupled online via a nano-electrospray ion source to a timsTOF HT mass spectrometer (Bruker Daltonics). On the Evosep One LC system peptides were separated in 44 min at a constant flow rate of 1.0 µL/min on a PepSep column (15 cm length, 75 µm ID, 1.5 µm C18 beads) (with a throughput of 30 samples per day [SPD]) using a dual buffer system with the mobile phases A (0.1% v/v formic acid) and B (0.1% v/v formic acid in 80% acetonitrile). The analytical column was connected to a fused silica emitter with a 10 µm ID (Bruker Daltonics) and maintained at 50°C.

Data acquisition settings are based on (*Skowronek et al., 2025*). The mass spectrometer was controlled by timsControl software. For the library, data was acquired in DDA-Parallel Accumulation Serial Fragmentation (PASEF) mode and the maps were acquired in DIA-PASEF mode, both covering a full scan range from 100 to 1,700 m/z and an ion mobility (IM) range of 0.7 to 1.3 Vs cm^{-2}. DDA-PASEF specific settings include: 100 ms ramp time; MS averaging of 1; Capillary captive spray: 1750 V; Intensity threshold: 2500; Target intensity: 20000; 10 PASEF scans. DIA-PASEF specific settings include: 100 ms accumulation time; MS averaging of 1; Capillary captive spray: 1750 V; high sensitivity detection: Inactive; Collision energy settings: 0.6 Vs cm^{-2} with 20 eV and 1.6 Vs cm^{-2} with 59 eV.

5.5.6 Mass spectrometry raw data analysis

Reference maps and ER stress maps:

"For protein identification, mass spectrometry raw data were analyzed in MaxQuant version 2.0.1.0 (*Tyanova et al., 2016a*). Match between runs and label-free quantification (LFQ) were enabled. The minimum LFQ count was set to 1. Default parameters were used for all other settings. The MaxQuant experimental design restricted matching to equivalent and adjacent fractions within the six-fraction profiling speed gradient. Cytosol and full proteome fractions were only matched to equivalent fractions. For ER stress maps, matching was only possible within a treatment condition. Spectra were searched against the SwissProt FASTA Saccharomyces cerevisiae database downloaded from UniProt (6,750 entries). The resulting intensity data and normalized profiles are provided as Supplemental Datasets 1 and 2. Mass

spectrometry data generated here will be made available at the ProteomeXchange Consortium via the PRIDE partner repository." Platzek et al., *bioRxiv*:2025.2002.2021.639471. (2025) (*Platzek et al., 2025*)

Starvation maps:

DDA-PASEF data was used to generate spectral libraries constructed with FragPipe version 22.0 with MSFragger version 4.1, IonQuant version 1.10.27, diaTracer version 1.1.5 and EasyPQP version 0.1.50.

DIA-PASEF data was analyzed with DIA-NN version 1.8.1. using the previously generated spectral library (*Demichev et al., 2022*). Default parameters were used (https://github.com/vdemichev/DiaNN?tab=readme-ov-file) with several changes to the settings as described in the following.

Precursor ion generation: Missed cleavages, 2; maximum number of variable modifications, 1; oxidation of methionines (Ox(M)) was enabled.

Algorithm: Mass accuracy, 15.0; MS1 accuracy, 15.0; isotopologues were enabled; MBR was enabled; no shared spectra was enabled; Heuristic protein interference was enabled; Protein interference, Genes; Neural network classifier, Single-pass mode; Quantification strategy, Robust LC (high precision); Library generation, Smart profiling.

Output: Threads, 40.

5.5.7 Mass spectrometry data analysis

5.5.7.1 Generation of compartment marker list

"A reference database was created containing 5389 proteins for which abundance estimates in molecules per cell were available (Table S2A; Ho et al, 2018). Eighteen localization categories were defined: actin-associated, cell wall, COPI coat, COPII coat, cytosol, ER, endosomes, ER-Golgi intermediate compartment (ERGIC), Golgi, lipid droplets, mitochondria, nucleus, nuclear envelope, peroxisomes, plasma membrane, proteasome core, ribosome core and vacuole. Two additional categories were 'ambiguous' (proteins for which evidence suggested localization to more than one subcellular compartment) and 'unknown' (proteins for which no assignment was possible). Based on an analysis of the GFP fusion collection (Kraus et al, 2017; data downloaded from the CYCLoPs web site), the Saccharomyces Genome Database and primary literature, proteins were manually assigned to one of the above categories.

The 2971 protein groups present in steady-state maps of unperturbed yeast were taken from the reference database and used for iterative training of the SVM module in DOM-ABC (see below). The first training set consisted of 868 protein groups, which were the 100 most abundant protein groups in the categories cytosol, ER, mitochondria, nucleus, plasma membrane and vacuole including endosomes, as well as all available protein groups in the categories Golgi, lipid droplets, nuclear envelope, peroxisomes, proteasome core and ribosome core. Proteins from the remaining categories were omitted because their localizations are inherently ambiguous. COPI, COPII and ERGIC proteins show complex distributions at the ER/Golgi interface and proteins related to the actin cytoskeleton are cytosolic but can associate with the plasma membrane. In addition, cell wall proteins were omitted because the cell wall had to be removed as part of the subcellular fractionation procedure. A first round of training achieved 94% recall, i.e. the SVM prediction agreed with the reference database for 815 protein groups. Furthermore, there were 682 additional protein groups for which a localization was predicted with at least medium confidence and matched the annotation in the reference database. A second training set was assembled by combining the 815 correctly recalled protein groups and the 682 additional protein groups correctly predicted during the first training round. The second round of training achieved 99.9% recall and correctly predicted the localization of 269 additional protein groups, and these results were used to assemble the third training set. This procedure was repeated until, after the seventh iteration, recall of the 1908 protein groups in the training set was 100% and no further protein groups were predicted correctly with at least medium confidence. The resulting final compartment marker set consisted of 1908 protein groups, corresponding to 1937 unique proteins." Platzek et al., *bioRxiv*:2025.2002.2021.639471. (2025) (*Platzek et al., 2025*)

5.5.7.2 Organellar mapping data analysis in DOM-ABC web app

"Data filtering, annotation, normalization, quality control, and mapping analyses were performed as described (Schessner et al, 2023). Briefly, the protein groups output file from MaxQuant is loaded into the online tool domaps version 1.0 (https://github.com/JuliaS92/SpatialProteomicsQC/tree/1.0), which formats the data for downstream analysis and quality control. Intensities in each of the six organelle fractions (1,000-78,000 x g pellets) are normalized to the total summed intensity across all fractions to obtain 0-to-1 normalized profiles. These can be directly compared 23 between proteins,

irrespective of relative abundance, and reflect subcellular distribution. Normalized profiles are then used for all downstream analyses, including calculation of map depth, fraction correlation evaluation, visualization by PCA, protein shift analysis, and compartment classification by SVMs. Relevant parameters were:

(1) Data annotation. Proteins were annotated with the compartment markers list and current gene names obtained from the Saccharomyces Genome Database.

(2) Data filtering. Only profiles with at least three consecutive fraction MS intensities and a minimum average MS count of two were retained.

(3) Principal component analysis (PCA). " Platzek et al., *bioRxiv*:2025.2002.2021.639471. (2025) (*Platzek et al., 2025*)

I performed all PCAs and generated scatter plots in python based on the adapted source code https://github.com/JuliaS92/SpatialProteomicsQC (*Schessner et al., 2023*). I averaged each fraction of triplicate abundance profiles in one condition, retaining also partial profiles. I performed PCA in three dimensions and plotted PC1 versus PC2 since they represented about 80% of the reference and ER stress maps data and about 70% of the starvation maps data (summed variance explained). Proteins identified as significant shifting hits and vacuole proteins annotated with their topology, were filtered after PCA and plotted individually in Figure 6D, Figure 17C and Figure 18B.

"(4) SVM compartment classification. Default settings were used to train and benchmark SVMs (C parameter range 1-30, gamma parameter range 1-50, 5 iterations with built-in five-fold cross validation). For model training, all markers were used and the optimized parameters were used for classification (test set proportion set to 0). For performance benchmarking, markers were split 80:20 into training and leave-out test sets (test set proportion set to 0.2). Models were trained with five-fold cross-validation on the training set only. Optimized SVMs were then applied to the test set to evaluate prediction performance via the F1 score (i.e. the harmonic mean of recall and precision). Average F1 scores across 20 sub-samples (i.e. 75%) of the predictions on the test set were then calculated for each organelle. The classes 'lipid droplets' and 'peroxisomes' had too few members to generate informative test sets and were excluded from performance benchmarking. For [reference] maps, all six replicates were combined into one dataset and processed jointly in the 'analysis' module of DOM-ABC to generate a single .json file. This file was then loaded into the 'benchmark' module of DOM-ABC for SVM classification. For ER stress [and starvation] maps , data for each condition were

separated into three [and four] protein groups files and processed individually in the analysis module to generate three [and four] .json files. These were then loaded into the benchmark module and jointly subjected to SVM analysis. The output of the SVM classification is a probability score for the likelihood of model fit for each of the 12 compartments represented in the compartment marker list (see above). For each protein, scores across compartments therefore add up to 1. Protein are assigned to the compartment with the highest score. Assignments are grouped into confidence classes depending on the magnitude of the score: >0.95 = very high, >0.8 = high, >0.65 = medium,

>0.4 = low, <0.4 = best guess. For Figure 1C, predictions with 'very high' and 'high' confidence were further grouped as 'high confidence', and predictions with 'low confidence' and 'best guess' as 'low confidence'.

(5) Movement-reproducibility (MR) analysis. To detect proteins with localization changes, default settings were applied for data pre-filtering (cosine correlation >0.9) and statistical testing (static data proportion = 0.75, number of iterations = 11). For each protein, the profiles from control cells are subtracted from profiles from [treated] cells to obtain a 'delta profile'. Proteins without significant changes have delta profiles close to baseline. To identify significantly deviating delta profiles, a robust multivariate outlier test is performed. P-values from three replicates are then combined with the Fisher method. The joint p-value is corrected with the Benjamini-Hochberg method and -log10 transformed to obtain the movement (M) score. M = 2 means that a protein undergoes a significant movement with an estimated FDR of 1%. Here, an M-score of 1.3 was chosen as cut-off for significance (FDR <5%). As an additional stringency filter, the direction of movement had to be consistent across replicates. The test therefore calculates the pairwise Pearson correlation of delta profile replicates (Rep1 vs Rep2, Rep1 vs Rep3 and Rep2 vs Rep3). The median of these three values was chosen as the R-score, with a value of 0.8 as cut-off for reproducibility. Finally, proteins had to have a p-value for movement <0.05 in at least two of the three replicates to qualify as hits. DOM-ABC performs a data quality filtering step prior to MR analysis so that only profiles with high replicate reproducibility (all pairwise cosine correlations >0.9) and only proteins profiled in all three replicates of both compared conditions are included. Hence, the number of proteins in the MR analysis is usually lower than the number of mapped proteins." Platzek et al., *bioRxiv*:2025.2002.2021.639471. (2025) (*Platzek et al., 2025*)

5.5.7.3 Full proteome quantification analysis

"Full proteome LFQ intensities were extracted from MaxQuant protein groups file and analyzed with Perseus software V1.6.2.3 (*Tyanova et al., 2016b*). [For the starvation maps full proteome LFQ intensities were analyzed with Perseus software version 1.6.1.13.] Proteins were filtered to remove reverse hits, proteins 'only identified by site' and potential contaminants.

For pairwise 'volcano' analyses, proteins were required to include at least three measured datapoints within one condition. Following log transformation, missing data were imputed from a normal distribution with a downshift of 1.8 standard deviations and a width of 0.3 standard deviations. Data were then analyzed with a two-tailed t-test [(500 iterations)] to identify proteins with altered abundance. Non-linear significance cut-offs (i.e. the 'volcano lines') were defined via Perseus' permutation-based FDR calculation (FDR <5%, S0 = 0.1).

For 1D-annotation enrichment, proteins were annotated with GO terms in Perseus and the results of the volcano analyses were analyzed with default settings." Platzek et al., *bioRxiv*:2025.2002.2021.639471. (2025) (*Platzek et al., 2025*)

5.5.7.4 Cytosolic shift analysis

"To estimate protein cytosolic pools, a second set of abundance profiles was generated in DOM-ABC that included the six organellar fractions and also the cytosol fraction. Normalized intensities in each fraction were weighted with the corresponding relative protein yields as measured by BCA assay. Weights for each fraction were calculated as average percentual protein recovery across replicates. Weighted intensities were divided by the sum across all fractions to obtain 0-to-1 normalized weighted intensities. These seven-datapoint profiles reflect percentage recovery of a protein across subcellular fractions. The cytosol fraction corresponds to the actual cytosolic pool (which is excluded from the six-datapoint profiles used to generate organellar maps, see above). The sum of the first six fractions indicates a protein's non-cytosolic pool. " Platzek et al., *bioRxiv*:2025.2002.2021.639471. (2025) (*Platzek et al., 2025*)

To determine the leakage of proteins during fractionation in the starvation maps, the proportion of cytosolic pool to non-cytosolic pool with the weighted intensities is calculated. I performed the analysis with a revised list of 126 vacuole marker proteins. The topology for each protein was classified with UniProt information as "integral", "peripheral", "lumenal".

"For ER stress maps, cytosolic pools were analyzed to identify proteins that shift to or away from the cytosol upon ER stress. First, proteins not quantified in all maps were excluded. Second, proteins minimally had to have a measured cytosolic pool in all three replicates of one treatment condition. For the remaining 2204 proteins, the cytosolic pool change was analyzed in control relative to DTT- or tunicamycin-treated cells with a paired two-tailed t-test. Since generation of the cytosolic pool data required several processing steps, which may contribute additional noise, the results for DTT- and tunicamycin-treated cells were combined to increase stringency and statistical power. The two individual p-values were combined with the Fisher method and the joint p-values were corrected for multiple testing with the Benjamini-Hochberg method. To qualify as hits, proteins had to have: an overall FDR <5%; significant individual p-values with both DTT and tunicamycin treatment (<0.05 for the DTT set and <0.1 for the slightly noisier tunicamycin set); an absolute cytosolic pool change >10% with DTT and tunicamycin treatment; the same direction of change (i.e. towards or away from the cytosol) under both conditions. 74 proteins passed these filters." Platzek et al., *bioRxiv*:2025.2002.2021.639471. (2025) (*Platzek et al., 2025*)

In the starvation dataset, cytosolic shift hits fulfilled following requirements: less than 60% of the cytosolic pool remained in WT starved compared to WT control but more than 90% were maintained in Δatg7 starved compared to Δatg7 control. 129 proteins passed that filter.

5.5.7.5 Identification of proteins shifting towards the ER during ER stress (organellar shift analysis)

"First, profile Pearson correlation of mapped proteins with the average ER marker profile was determined for control and DTT-treated cells. For each protein, the change of correlation with ER markers was calculated as Delta correlER = (correlationDTT ER) – (correlationCon ER). A positive Delta CorrelER identified proteins that correlated better with ER markers under ER stress. To identify proteins shifting towards the ER, the following filters were applied: hit in the DTT MR analysis (M >1.3, R >0.8); positive Delta CorrelER; Pearson correlation with average ER marker profile in DTT-treated cells >0.75; protein has post-ER secretory pathway localization in untreated cells according to reference database or SVM classification. This analysis identified 86 proteins. Inspection of the 410 DTT hits identified three proteins (Ape3, Sln1, Toh1) that narrowly failed the second filter but passed all other filters and had a convincing shift towards the ER in PCA plots. They were therefore added to the final list of 89 proteins." Platzek et al., *bioRxiv*:2025.2002.2021.639471. (2025) (*Platzek et al., 2025*)

5.5.7.6 Nearest neighbor profile analysis

Neighborhood analysis was based on (*Borner et al., 2014*) to calculate the similarity of protein profiles. In brief, the distances or Pearson correlations of a given protein and all mapped proteins are determined and sorted in ascending or descending order, respectively. The smaller the distance or the closer the correlation to 1, the more similar are the abundance profiles. This enables detection of interacting proteins and proteins in the vicinity.

6 REFERENCES

Akey, C.W., D. Singh, C. Ouch, I. Echeverria, I. Nudelman, J.M. Varberg, Z. Yu, F. Fang, Y. Shi, J. Wang, D. Salzberg, K. Song, C. Xu, J.C. Gumbart, S. Suslov, J. Unruh, S.L. Jaspersen, B.T. Chait, A. Sali, J. Fernandez-Martinez, S.J. Ludtke, E. Villa, and M.P. Rout. 2022. Comprehensive structure and functional adaptations of the yeast nuclear pore complex. *Cell*. 185:361-378 e325.

Anantharaman, V., and L. Aravind. 2002. The GOLD domain, a novel protein module involved in Golgi function and secretion. *Genome Biol*. 3:research0023.

Athane, A., A. Buisson, M. Challier, F. Beaumatin, S. Manon, I. Bhatia-Kissova, and N. Camougrand. 2015. Insights into the relationship between the proteasome and autophagy in human and yeast cells. *Int J Biochem Cell Biol*. 64:167-173.

Baba, M., M. Osumi, S.V. Scott, D.J. Klionsky, and Y. Ohsumi. 1997. Two distinct pathways for targeting proteins from the cytoplasm to the vacuole/lysosome. *J Cell Biol*. 139:1687-1695.

Baba, M., K. Takeshige, N. Baba, and Y. Ohsumi. 1994. Ultrastructural analysis of the autophagic process in yeast: detection of autophagosomes and their characterization. *J Cell Biol*. 124:903-913.

Barlowe, C., L. Orci, T. Yeung, M. Hosobuchi, S. Hamamoto, N. Salama, M.F. Rexach, M. Ravazzola, M. Amherdt, and R. Schekman. 1994. COPII: a membrane coat formed by Sec proteins that drive vesicle budding from the endoplasmic reticulum. *Cell*. 77:895-907.

Barnes, G., W.J. Hansen, C.L. Holcomb, and J. Rine. 1984. Asparagine-linked glycosylation in Saccharomyces cerevisiae: genetic analysis of an early step. *Mol Cell Biol*. 4:2381-2388.

Bernales, S., K.L. McDonald, and P. Walter. 2006. Autophagy counterbalances endoplasmic reticulum expansion during the unfolded protein response. *PLoS Biol*. 4:e423.

Bertolotti, A., Y. Zhang, L.M. Hendershot, H.P. Harding, and D. Ron. 2000. Dynamic interaction of BiP and ER stress transducers in the unfolded-protein response. *Nat Cell Biol*. 2:326-332.

Bhavsar, R.B., L.N. Makley, and P.A. Tsonis. 2010. The other lives of ribosomal proteins. *Hum Genomics*. 4:327-344.

Bieber, A., C. Capitanio, P.S. Erdmann, F. Fiedler, F. Beck, C.W. Lee, D. Li, G. Hummer, B.A. Schulman, W. Baumeister, and F. Wilfling. 2022. In situ structural analysis reveals membrane shape transitions during autophagosome formation. *Proc Natl Acad Sci U S A*. 119:e2209823119.

Black, A., T.D. Williams, F. Soubigou, I.M. Joshua, H. Zhou, F. Lamoliatte, and A. Rousseau. 2023. The ribosome-associated chaperone Zuo1 controls translation upon TORC1 inhibition. *EMBO J*. 42:e113240.

Borner, G.H., M.Y. Hein, J. Hirst, J.R. Edgar, M. Mann, and M.S. Robinson. 2014. Fractionation profiling: a fast and versatile approach for mapping vesicle proteomes and protein-protein interactions. *Mol Biol Cell*. 25:3178-3194.

Braakman, I., J. Helenius, and A. Helenius. 1992. Manipulating disulfide bond formation and protein folding in the endoplasmic reticulum. *EMBO J*. 11:1717-1722.

Breker, M., M. Gymrek, and M. Schuldiner. 2013. A novel single-cell screening platform reveals proteome plasticity during yeast stress responses. *J Cell Biol*. 200:839-850.

Carlsson, S.R., and A. Simonsen. 2015. Membrane dynamics in autophagosome biogenesis. *J Cell Sci*. 128:193-205.

Castillon, G.A., R. Watanabe, M. Taylor, T.M. Schwabe, and H. Riezman. 2009. Concentration of GPI-anchored proteins upon ER exit in yeast. *Traffic*. 10:186-200.

Chapman, J.D., D.R. Goodlett, and C.D. Masselon. 2014. Multiplexed and data-independent tandem mass spectrometry for global proteome profiling. *Mass Spectrom Rev*. 33:452-470.

Chatterjee, S., M. Javier, and U. Stochaj. 1997. In vivo analysis of nuclear protein traffic in mammalian cells. *Exp Cell Res*. 236:346-350.

Chen, X., C. VanValkenburgh, H. Liang, H. Fang, and N. Green. 2001. Signal peptidase and oligosaccharyltransferase interact in a sequential and dependent manner within the endoplasmic reticulum. *J Biol Chem*. 276:2411-2416.

Cooper, A.A., and T.H. Stevens. 1996. Vps10p cycles between the late-Golgi and prevacuolar compartments in its function as the sorting receptor for multiple yeast vacuolar hydrolases. *J Cell Biol*. 133:529-541.

Cowles, C.R., G. Odorizzi, G.S. Payne, and S.D. Emr. 1997. The AP-3 adaptor complex is essential for cargo-selective transport to the yeast vacuole. *Cell*. 91:109-118.

Cox, J.S., R.E. Chapman, and P. Walter. 1997. The unfolded protein response coordinates the production of endoplasmic reticulum protein and endoplasmic reticulum membrane. *Mol Biol Cell*. 8:1805-1814.

Daran, J.M., N. Dallies, D. Thines-Sempoux, V. Paquet, and J. Francois. 1995. Genetic and biochemical characterization of the UGP1 gene encoding the UDP-glucose pyrophosphorylase from Saccharomyces cerevisiae. *Eur J Biochem*. 233:520-530.

Davies, A.K., D.N. Itzhak, J.R. Edgar, T.L. Archuleta, J. Hirst, L.P. Jackson, M.S. Robinson, and G.H.H. Borner. 2018. AP-4 vesicles contribute to spatial control of autophagy via RUSC-dependent peripheral delivery of ATG9A. *Nat Commun*. 9:3958.

Demichev, V., L. Szyrwiel, F. Yu, G.C. Teo, G. Rosenberger, A. Niewienda, D. Ludwig, J. Decker, S. Kaspar-Schoenefeld, K.S. Lilley, M. Mulleder, A.I. Nesvizhskii, and M. Ralser. 2022. dia-PASEF data analysis using FragPipe and DIA-NN for deep proteomics of low sample amounts. *Nat Commun*. 13:3944.

Diekmann, Y., and J.B. Pereira-Leal. 2013. Evolution of intracellular compartmentalization. *Biochem J*. 449:319-331.

Doms, R.W., A. Ruusala, C. Machamer, J. Helenius, A. Helenius, and J.K. Rose. 1988. Differential effects of mutations in three domains on folding, quaternary structure, and intracellular transport of vesicular stomatitis virus G protein. *J Cell Biol*. 107:89-99.

Dultz, E., M. Wojtynek, O. Medalia, and E. Onischenko. 2022. The Nuclear Pore Complex: Birth, Life, and Death of a Cellular Behemoth. *Cells*. 11.

Eising, S., B. Esch, M. Walte, P. Vargas Duarte, S. Walter, C. Ungermann, M. Bohnert, and F. Frohlich. 2022. A lysosomal biogenesis map reveals the cargo spectrum of yeast vacuolar protein targeting pathways. *J Cell Biol*. 221.

Enenkel, C., G. Blobel, and M. Rexach. 1995. Identification of a yeast karyopherin heterodimer that targets import substrate to mammalian nuclear pore complexes. *J Biol Chem*. 270:16499-16502.

Evans, E.A., R. Gilmore, and G. Blobel. 1986. Purification of microsomal signal peptidase as a complex. *Proc Natl Acad Sci U S A*. 83:581-585.

Fabre, E., T. Hurtaux, and C. Fradin. 2014. Mannosylation of fungal glycoconjugates in the Golgi apparatus. *Curr Opin Microbiol*. 20:103-110.

Fauconnier, C., and G. Haesbroeck. 2009. Outliers detection with the minimum covariance determinant estimator in practice. *Statistical Methodology*. 6:363-379.

Fregno, I., and M. Molinari. 2018. Endoplasmic reticulum turnover: ER-phagy and other flavors in selective and non-selective ER clearance. *F1000Res*. 7:454.

Garcia, E.J., P.C. Liao, G. Tan, J.D. Vevea, C.N. Sing, C.A. Tsang, J.M. McCaffery, I.R. Boldogh, and L.A. Pon. 2021. Membrane dynamics and protein targets of lipid droplet microautophagy during ER stress-induced proteostasis in the budding yeast, Saccharomyces cerevisiae. *Autophagy*. 17:2363-2383.

Gardner, B.M., and P. Walter. 2011. Unfolded proteins are Ire1-activating ligands that directly induce the unfolded protein response. *Science*. 333:1891-1894.

Gautschi, M., A. Mun, S. Ross, and S. Rospert. 2002. A functional chaperone triad on the yeast ribosome. *Proc Natl Acad Sci U S A*. 99:4209-4214.

Gibson, D.G., L. Young, R.Y. Chuang, J.C. Venter, C.A. Hutchison, 3rd, and H.O. Smith. 2009. Enzymatic assembly of DNA molecules up to several hundred kilobases. *Nat Methods*. 6:343-345.

Ginevskaia, T., A. Innokentev, K. Furukawa, T. Fukuda, M. Hayatsu, S.I. Yamashita, K. Inoue, S. Shibata, and T. Kanki. 2024. Comprehensive analysis of non-selective and selective

autophagy in yeast atg mutants and characterization of autophagic activity in the absence of the Atg8 conjugation system. *J Biochem*. 176:217-227.

Gonzalez, A., and M.N. Hall. 2017. Nutrient sensing and TOR signaling in yeast and mammals. *EMBO J*. 36:397-408.

Gorlich, D., F. Vogel, A.D. Mills, E. Hartmann, and R.A. Laskey. 1995. Distinct functions for the two importin subunits in nuclear protein import. *Nature*. 377:246-248.

Graham, J.M. 2001. Biological centrifugation. Bios, Oxford. x, 210 p. pp.

Guo, G.G., K. Patel, V. Kumar, M. Shah, V.A. Fried, J.D. Etlinger, and P.B. Sehgal. 2002. Association of the chaperone glucose-regulated protein 58 (GRP58/ER-60/ERp57) with Stat3 in cytosol and plasma membrane complexes. *J Interferon Cytokine Res*. 22:555-563.

Halbleib, K., K. Pesek, R. Covino, H.F. Hofbauer, D. Wunnicke, I. Hanelt, G. Hummer, and R. Ernst. 2017. Activation of the Unfolded Protein Response by Lipid Bilayer Stress. *Mol Cell*. 67:673-684 e678.

Hamada, K., S. Fukuchi, M. Arisawa, M. Baba, and K. Kitada. 1998. Screening for glycosylphosphatidylinositol (GPI)-dependent cell wall proteins in Saccharomyces cerevisiae. *Mol Gen Genet*. 258:53-59.

Hanada, T., N.N. Noda, Y. Satomi, Y. Ichimura, Y. Fujioka, T. Takao, F. Inagaki, and Y. Ohsumi. 2007. The Atg12-Atg5 conjugate has a novel E3-like activity for protein lipidation in autophagy. *J Biol Chem*. 282:37298-37302.

Harding, T.M., A. Hefner-Gravink, M. Thumm, and D.J. Klionsky. 1996. Genetic and phenotypic overlap between autophagy and the cytoplasm to vacuole protein targeting pathway. *J Biol Chem*. 271:17621-17624.

Hatakeyama, R., and C. De Virgilio. 2019. TORC1 specifically inhibits microautophagy through ESCRT-0. *Curr Genet*. 65:1243-1249.

Hein, M.Y., D. Peng, V. Todorova, F. McCarthy, K. Kim, C. Liu, L. Savy, C. Januel, R. Baltazar-Nunez, M. Sekhar, S. Vaid, S. Bax, M. Vangipuram, J. Burgess, L. Njoya, E. Wang, I.E. Ivanov, J.R. Byrum, S. Pradeep, C.G. Gonzalez, Y. Aniseia, J.S. Creery, A.H. McMorrow, S. Sunshine, S. Yeung-Levy, B.C. DeFelice, S.B. Mehta, D.N. Itzhak, J.E. Elias, and M.D. Leonetti. 2025. Global organelle profiling reveals subcellular localization and remodeling at proteome scale. *Cell*. 188:1137-1155 e1120.

Hinnebusch, A.G., and K. Natarajan. 2002. Gcn4p, a master regulator of gene expression, is controlled at multiple levels by diverse signals of starvation and stress. *Eukaryot Cell*. 1:22-32.

Hirst, J., W.W. Lui, N.A. Bright, N. Totty, M.N. Seaman, and M.S. Robinson. 2000. A family of proteins with gamma-adaptin and VHS domains that facilitate trafficking between the trans-Golgi network and the vacuole/lysosome. *J Cell Biol*. 149:67-80.

Ho, B., A. Baryshnikova, and G.W. Brown. 2018. Unification of Protein Abundance Datasets Yields a Quantitative Saccharomyces cerevisiae Proteome. *Cell Syst*. 6:192-205 e193.

Hollenstein, D.M., R. Gomez-Sanchez, A. Ciftci, F. Kriegenburg, M. Mari, R. Torggler, M. Licheva, F. Reggiori, and C. Kraft. 2019. Vac8 spatially confines autophagosome formation at the vacuole in S. cerevisiae. *J Cell Sci*. 132.

Hu, J., Y. Shibata, C. Voss, T. Shemesh, Z. Li, M. Coughlin, M.M. Kozlov, T.A. Rapoport, and W.A. Prinz. 2008. Membrane proteins of the endoplasmic reticulum induce high-curvature tubules. *Science*. 319:1247-1250.

Hughes Hallett, J.E., X. Luo, and A.P. Capaldi. 2015. Snf1/AMPK promotes the formation of Kog1/Raptor-bodies to increase the activation threshold of TORC1 in budding yeast. *Elife*. 4.

Huh, W.K., J.V. Falvo, L.C. Gerke, A.S. Carroll, R.W. Howson, J.S. Weissman, and E.K. O'Shea. 2003. Global analysis of protein localization in budding yeast. *Nature*. 425:686-691.

Ichimura, Y., T. Kirisako, T. Takao, Y. Satomi, Y. Shimonishi, N. Ishihara, N. Mizushima, I. Tanida, E. Kominami, M. Ohsumi, T. Noda, and Y. Ohsumi. 2000. A ubiquitin-like system mediates protein lipidation. *Nature*. 408:488-492.

Igbaria, A., P.I. Merksamer, A. Trusina, F. Tilahun, J.R. Johnson, O. Brandman, N.J. Krogan, J.S. Weissman, and F.R. Papa. 2019. Chaperone-mediated reflux of secretory proteins

to the cytosol during endoplasmic reticulum stress. *P Natl Acad Sci USA*. 116:11291-11298.

Iovine, M.K., and S.R. Wente. 1997. A nuclear export signal in Kap95p is required for both recycling the import factor and interaction with the nucleoporin GLFG repeat regions of Nup116p and Nup100p. *J Cell Biol*. 137:797-811.

Isoda, T., E. Takeda, S. Hosokawa, S. Hotta-Ren, and Y. Ohsumi. 2024. Atg45 is an autophagy receptor for glycogen, a non-preferred cargo of bulk autophagy in yeast. *iScience*. 27:109810.

Ito, H., Y. Fukuda, K. Murata, and A. Kimura. 1983. Transformation of intact yeast cells treated with alkali cations. *J Bacteriol*. 153:163-168.

Itzhak, D.N., C. Davies, S. Tyanova, A. Mishra, J. Williamson, R. Antrobus, J. Cox, M.P. Weekes, and G.H.H. Borner. 2017. A Mass Spectrometry-Based Approach for Mapping Protein Subcellular Localization Reveals the Spatial Proteome of Mouse Primary Neurons. *Cell Rep*. 20:2706-2718.

Itzhak, D.N., J.P. Schessner, and G.H.H. Borner. 2019. Dynamic Organellar Maps for Spatial Proteomics. *Curr Protoc Cell Biol*. 83:e81.

Itzhak, D.N., S. Tyanova, J. Cox, and G.H. Borner. 2016. Global, quantitative and dynamic mapping of protein subcellular localization. *Elife*. 5.

Jang, H.S., Y. Lee, Y. Kim, and W.K. Huh. 2024. The ubiquitin-proteasome system degrades fatty acid synthase under nitrogen starvation when autophagy is dysfunctional in Saccharomyces cerevisiae. *Biochem Biophys Res Commun*. 733:150423.

Janke, C., M.M. Magiera, N. Rathfelder, C. Taxis, S. Reber, H. Maekawa, A. Moreno-Borchart, G. Doenges, E. Schwob, E. Schiebel, and M. Knop. 2004. A versatile toolbox for PCR-based tagging of yeast genes: new fluorescent proteins, more markers and promoter substitution cassettes. *Yeast*. 21:947-962.

Johansen, T., and T. Lamark. 2011. Selective autophagy mediated by autophagic adapter proteins. *Autophagy*. 7:279-296.

Jones, C.B., E.M. Ott, J.M. Keener, M. Curtiss, V. Sandrin, and M. Babst. 2012. Regulation of membrane protein degradation by starvation-response pathways. *Traffic*. 13:468-482.

Kaberniuk, A.A., N.C. Morano, V.V. Verkhusha, and E.L. Snapp. 2017. moxDendra2: an inert photoswitchable protein for oxidizing environments. *Chem Commun (Camb)*. 53:2106-2109.

Kalderon, D., B.L. Roberts, W.D. Richardson, and A.E. Smith. 1984. A short amino acid sequence able to specify nuclear location. *Cell*. 39:499-509.

Kaufmann, A., V. Beier, H.G. Franquelim, and T. Wollert. 2014. Molecular mechanism of autophagic membrane-scaffold assembly and disassembly. *Cell*. 156:469-481.

Khalfan, W.A., and D.J. Klionsky. 2002. Molecular machinery required for autophagy and the cytoplasm to vacuole targeting (Cvt) pathway in S. cerevisiae. *Curr Opin Cell Biol*. 14:468-475.

Kira, S., K. Tabata, K. Shirahama-Noda, A. Nozoe, T. Yoshimori, and T. Noda. 2014. Reciprocal conversion of Gtr1 and Gtr2 nucleotide-binding states by Npr2-Npr3 inactivates TORC1 and induces autophagy. *Autophagy*. 10:1565-1578.

Kobayashi, Y., A. Oguro, Y. Hirata, and S. Imaoka. 2021. The regulation of Hypoxia-Inducible Factor-1 (HIF-1alpha) expression by Protein Disulfide Isomerase (PDI). *PLoS One*. 16:e0246531.

Kodaki, T., S. Tsuji, N. Otani, D. Yamamoto, K.S. Rao, S. Watanabe, M. Tsukatsune, and K. Makino. 2003. Differential transcriptional regulation of two distinct S-adenosylmethionine synthetase genes (SAM1 and SAM2) of Saccharomyces cerevisiae. *Nucleic Acids Res Suppl*:303-304.

Kozik, P., M. Gros, D.N. Itzhak, L. Joannas, S. Heurtebise-Chretien, P.A. Krawczyk, P. Rodriguez-Silvestre, A. Alloatti, J.G. Magalhaes, E. Del Nery, G.H.H. Borner, and S. Amigorena. 2020. Small Molecule Enhancers of Endosome-to-Cytosol Import Augment Anti-tumor Immunity. *Cell Rep*. 32:107905.

Kraft, C., A. Deplazes, M. Sohrmann, and M. Peter. 2008. Mature ribosomes are selectively degraded upon starvation by an autophagy pathway requiring the Ubp3p/Bre5p ubiquitin protease. *Nat Cell Biol*. 10:602-610.

Kraft, C., M. Kijanska, E. Kalie, E. Siergiejuk, S.S. Lee, G. Semplicio, I. Stoffel, A. Brezovich, M. Verma, I. Hansmann, G. Ammerer, K. Hofmann, S. Tooze, and M. Peter. 2012. Binding of the Atg1/ULK1 kinase to the ubiquitin-like protein Atg8 regulates autophagy. *EMBO J*. 31:3691-3703.

Kralt, A., M. Wojtynek, J.S. Fischer, A. Agote-Aran, R. Mancini, E. Dultz, E. Noor, F. Uliana, M. Tatarek-Nossol, W. Antonin, E. Onischenko, O. Medalia, and K. Weis. 2022. An amphipathic helix in Brl1 is required for nuclear pore complex biogenesis in S. cerevisiae. *Elife*. 11.

Kraus, O.Z., B.T. Grys, J. Ba, Y. Chong, B.J. Frey, C. Boone, and B.J. Andrews. 2017. Automated analysis of high-content microscopy data with deep learning. *Mol Syst Biol*. 13:924.

Lajoie, P., and E.L. Snapp. 2020. Size-dependent secretory protein reflux into the cytosol in association with acute endoplasmic reticulum stress. *Traffic*. 21:419-429.

Lautier, O., A. Penzo, J.O. Rouviere, G. Chevreux, L. Collet, I. Loiodice, A. Taddei, F. Devaux, M.A. Collart, and B. Palancade. 2021. Co-translational assembly and localized translation of nucleoporins in nuclear pore complex biogenesis. *Mol Cell*. 81:2417-2427 e2415.

Lee, C.W., F. Wilfling, P. Ronchi, M. Allegretti, S. Mosalaganti, S. Jentsch, M. Beck, and B. Pfander. 2020. Selective autophagy degrades nuclear pore complexes. *Nat Cell Biol*. 22:159-166.

Li, C., A. Goryaynov, and W. Yang. 2016. The selective permeability barrier in the nuclear pore complex. *Nucleus*. 7:430-446.

Li, D., J.Z. Song, H. Li, M.H. Shan, Y. Liang, J. Zhu, and Z. Xie. 2015. Storage lipid synthesis is necessary for autophagy induced by nitrogen starvation. *FEBS Lett*. 589:269-276.

Li, J., M. Breker, M. Graham, M. Schuldiner, and M. Hochstrasser. 2019. AMPK regulates ESCRT-dependent microautophagy of proteasomes concomitant with proteasome storage granule assembly during glucose starvation. *PLoS Genet*. 15:e1008387.

Litsios, A., B.T. Grys, O.Z. Kraus, H. Friesen, C. Ross, M.P.D. Masinas, D.T. Forster, M.T. Couvillion, S. Timmermann, M. Billmann, C. Myers, N. Johnsson, L.S. Churchman, C. Boone, and B.J. Andrews. 2024. Proteome-scale movements and compartment connectivity during the eukaryotic cell cycle. *Cell*. 187:1490-1507 e1421.

Liu, K., B.M. Sutter, and B.P. Tu. 2021. Autophagy sustains glutamate and aspartate synthesis in Saccharomyces cerevisiae during nitrogen starvation. *Nat Commun*. 12:57.

Lodish, H.F. 1988. Transport of secretory and membrane glycoproteins from the rough endoplasmic reticulum to the Golgi. A rate-limiting step in protein maturation and secretion. *J Biol Chem*. 263:2107-2110.

Loewith, R., and M.N. Hall. 2011. Target of rapamycin (TOR) in nutrient signaling and growth control. *Genetics*. 189:1177-1201.

Longtine, M.S., A. McKenzie, 3rd, D.J. Demarini, N.G. Shah, A. Wach, A. Brachat, P. Philippsen, and J.R. Pringle. 1998. Additional modules for versatile and economical PCR-based gene deletion and modification in Saccharomyces cerevisiae. *Yeast*. 14:953-961.

Lord, C.L., and S.R. Wente. 2020. Nuclear envelope-vacuole contacts mitigate nuclear pore complex assembly stress. *J Cell Biol*. 219.

Lukinavicius, G., K. Umezawa, N. Olivier, A. Honigmann, G. Yang, T. Plass, V. Mueller, L. Reymond, I.R. Correa, Jr., Z.G. Luo, C. Schultz, E.A. Lemke, P. Heppenstall, C. Eggeling, S. Manley, and K. Johnsson. 2013. A near-infrared fluorophore for live-cell super-resolution microscopy of cellular proteins. *Nat Chem*. 5:132-139.

Lundberg, E., and G.H.H. Borner. 2019. Spatial proteomics: a powerful discovery tool for cell biology. *Nat Rev Mol Cell Biol*. 20:285-302.

Lynch-Day, M.A., and D.J. Klionsky. 2010. The Cvt pathway as a model for selective autophagy. *FEBS Lett*. 584:1359-1366.

Makino, S., T. Kawamata, S. Iwasaki, and Y. Ohsumi. 2021. Selectivity of mRNA degradation by autophagy in yeast. *Nat Commun*. 12:2316.

Martinez-Bono, B., I. Quilis, E. Zalve, and J.C. Igual. 2010. Yeast karyopherins Kap123 and Kap95 are related to the function of the cell integrity pathway. *FEMS Yeast Res*. 10:28-37.

Marzioch, M., D.C. Henthorn, J.M. Herrmann, R. Wilson, D.Y. Thomas, J.J. Bergeron, R.C. Solari, and A. Rowley. 1999. Erp1p and Erp2p, partners for Emp24p and Erv25p in a yeast p24 complex. *Mol Biol Cell*. 10:1923-1938.

Mast, F.D., A. Jamakhandi, R.A. Saleem, D.J. Dilworth, R.S. Rogers, R.A. Rachubinski, and J.D. Aitchison. 2016. Peroxins Pex30 and Pex29 Dynamically Associate with Reticulons to Regulate Peroxisome Biogenesis from the Endoplasmic Reticulum. *J Biol Chem*. 291:15408-15427.

Matsumoto, S., K. Nakatsukasa, C. Kakuta, Y. Tamura, M. Esaki, and T. Endo. 2019. Msp1 Clears Mistargeted Proteins by Facilitating Their Transfer from Mitochondria to the ER. *Mol Cell*. 76:191-205 e110.

Matsumoto, S., S. Ono, S. Shinoda, C. Kakuta, S. Okada, T. Ito, T. Numata, and T. Endo. 2022. GET pathway mediates transfer of mislocalized tail-anchored proteins from mitochondria to the ER. *J Cell Biol*. 221.

McGoldrick, P., A. Lau, Z. You, T.M. Durcan, and J. Robertson. 2023. Loss of C9orf72 perturbs the Ran-GTPase gradient and nucleocytoplasmic transport, generating compositionally diverse Importin beta-1 granules. *Cell Rep*. 42:112134.

Meiling-Wesse, K., H. Barth, C. Voss, E.L. Eskelinen, U.D. Epple, and M. Thumm. 2004. Atg21 is required for effective recruitment of Atg8 to the preautophagosomal structure during the Cvt pathway. *J Biol Chem*. 279:37741-37750.

Metur, S.P., and D.J. Klionsky. 2024. Nutrient-dependent signaling pathways that control autophagy in yeast. *FEBS Lett*. 598:32-47.

Meurer, M., Y. Duan, E. Sass, I. Kats, K. Herbst, B.C. Buchmuller, V. Dederer, F. Huber, D. Kirrmaier, M. Stefl, K. Van Laer, T.P. Dick, M.K. Lemberg, A. Khmelinskii, E.D. Levy, and M. Knop. 2018. Genome-wide C-SWAT library for high-throughput yeast genome tagging. *Nat Methods*. 15:598-600.

Miesenbock, G., D.A. De Angelis, and J.E. Rothman. 1998. Visualizing secretion and synaptic transmission with pH-sensitive green fluorescent proteins. *Nature*. 394:192-195.

Miller, E.A., T.H. Beilharz, P.N. Malkus, M.C. Lee, S. Hamamoto, L. Orci, and R. Schekman. 2003. Multiple cargo binding sites on the COPII subunit Sec24p ensure capture of diverse membrane proteins into transport vesicles. *Cell*. 114:497-509.

Mizushima, N., T. Yoshimori, and Y. Ohsumi. 2011. The role of Atg proteins in autophagosome formation. *Annu Rev Cell Dev Biol*. 27:107-132.

Mochida, K., Y. Oikawa, Y. Kimura, H. Kirisako, H. Hirano, Y. Ohsumi, and H. Nakatogawa. 2015. Receptor-mediated selective autophagy degrades the endoplasmic reticulum and the nucleus. *Nature*. 522:359-362.

Monschau, N., K.P. Stahmann, H. Sahm, J.B. McNeil, and A.L. Bognar. 1997. Identification of Saccharomyces cerevisiae GLY1 as a threonine aldolase: a key enzyme in glycine biosynthesis. *FEMS Microbiol Lett*. 150:55-60.

Muller, M., O. Schmidt, M. Angelova, K. Faserl, S. Weys, L. Kremser, T. Pfaffenwimmer, T. Dalik, C. Kraft, Z. Trajanoski, H. Lindner, and D. Teis. 2015. The coordinated action of the MVB pathway and autophagy ensures cell survival during starvation. *Elife*. 4:e07736.

Muller, O., T. Sattler, M. Flotenmeyer, H. Schwarz, H. Plattner, and A. Mayer. 2000. Autophagic tubes: vacuolar invaginations involved in lateral membrane sorting and inverse vesicle budding. *J Cell Biol*. 151:519-528.

Muniz, M., and H. Riezman. 2016. Trafficking of glycosylphosphatidylinositol anchored proteins from the endoplasmic reticulum to the cell surface. *J Lipid Res*. 57:352-360.

Natarajan, K., M.R. Meyer, B.M. Jackson, D. Slade, C. Roberts, A.G. Hinnebusch, and M.J. Marton. 2001. Transcriptional profiling shows that Gcn4p is a master regulator of gene expression during amino acid starvation in yeast. *Mol Cell Biol*. 21:4347-4368.

Nickel, W., and F.T. Wieland. 1997. Biogenesis of COPI-coated transport vesicles. *FEBS Lett*. 413:395-400.

Nightingale, D.J., A. Geladaki, L.M. Breckels, S.G. Oliver, and K.S. Lilley. 2019. The subcellular organisation of Saccharomyces cerevisiae. *Curr Opin Chem Biol*. 48:86-95.

Noda, T., and D.J. Klionsky. 2008. The quantitative Pho8Delta60 assay of nonspecific autophagy. *Methods Enzymol*. 451:33-42.

Noda, T., A. Matsuura, Y. Wada, and Y. Ohsumi. 1995. Novel system for monitoring autophagy in the yeast Saccharomyces cerevisiae. *Biochem Biophys Res Commun*. 210:126-132.

Nyathi, Y., B.M. Wilkinson, and M.R. Pool. 2013. Co-translational targeting and translocation of proteins to the endoplasmic reticulum. *Biochim Biophys Acta*. 1833:2392-2402.

Oda, M.N., S.V. Scott, A. Hefner-Gravink, A.D. Caffarelli, and D.J. Klionsky. 1996. Identification of a cytoplasm to vacuole targeting determinant in aminopeptidase I. *J Cell Biol*. 132:999-1010.

Otto, T.A., T. Bergsma, M. Dekker, S.N. Mouton, P. Gallardo, J.C. Wolters, A. Steen, P.R. Onck, and L.M. Veenhoff. 2024. Nucleoporin Nsp1 surveils the phase state of FG-Nups. *Cell Rep*. 43:114793.

Paine, P.L., L.C. Moore, and S.B. Horowitz. 1975. Nuclear envelope permeability. *Nature*. 254:109-114.

Panchaud, N., M.P. Peli-Gulli, and C. De Virgilio. 2013. Amino acid deprivation inhibits TORC1 through a GTPase-activating protein complex for the Rag family GTPase Gtr1. *Sci Signal*. 6:ra42.

Panzner, S., L. Dreier, E. Hartmann, S. Kostka, and T.A. Rapoport. 1995. Posttranslational protein transport in yeast reconstituted with a purified complex of Sec proteins and Kar2p. *Cell*. 81:561-570.

Papagiannidis, D., P.W. Bircham, C. Luchtenborg, O. Pajonk, G. Ruffini, B. Brugger, and S. Schuck. 2021. Ice2 promotes ER membrane biogenesis in yeast by inhibiting the conserved lipin phosphatase complex. *EMBO J*. 40:e107958.

Pearse, B.M., and M.S. Robinson. 1990. Clathrin, adaptors, and sorting. *Annu Rev Cell Biol*. 6:151-171.

Pédelacq, J.D., S. Cabantous, T. Tran, T.C. Terwilliger, and G.S. Waldo. 2006. Engineering and characterization of a superfolder green fluorescent protein. *Nat Biotechnol*. 24:79-88.

Pelham, H.R., K.G. Hardwick, and M.J. Lewis. 1988. Sorting of soluble ER proteins in yeast. *EMBO J*. 7:1757-1762.

Pietras, P.J., A. Wasilewska-Burczyk, K. Peplowska, L. Marczak, A. Tyczewska, and K. Grzywacz. 2024. Dynamic protein composition of Saccharomyces cerevisiae ribosomes in response to multiple stress conditions reflects alterations in translation activity. *Int J Biol Macromol*. 268:132004.

Pincus, D., A. Aranda-Díaz, I.A. Zuleta, P. Walter, and H. El-Samad. 2014. Delayed Ras/PKA signaling augments the unfolded protein response. *P Natl Acad Sci USA*. 111:14800-14805.

Platzek, A., J.P. Schessner, K. Odehnalová, G.H.H. Borner, and S. Schuck. 2025. Dynamic Organellar Mapping in yeast reveals extensive protein localization changes during ER stress. *bioRxiv*:2025.2002.2021.639471.

Poveda-Huertes, D., A.A. Taskin, I. Dhaouadi, L. Myketin, A. Marada, L. Habernig, S. Buttner, and F.N. Vogtle. 2021. Increased mitochondrial protein import and cardiolipin remodelling upon early mtUPR. *PLoS Genet*. 17:e1009664.

Powers, T., and P. Walter. 1999. Regulation of ribosome biogenesis by the rapamycin-sensitive TOR-signaling pathway in Saccharomyces cerevisiae. *Mol Biol Cell*. 10:987-1000.

Radanovic, T., and R. Ernst. 2021. The Unfolded Protein Response as a Guardian of the Secretory Pathway. *Cells*. 10.

Rahman, M.A., M. Terasawa, M.G. Mostofa, and T. Ushimaru. 2018. The TORC1-Nem1/Spo7-Pah1/lipin axis regulates microautophagy induction in budding yeast. *Biochem Biophys Res Commun*. 504:505-512.

Rapoport, T.A., L. Li, and E. Park. 2017. Structural and Mechanistic Insights into Protein Translocation. *Annu Rev Cell Dev Biol*. 33:369-390.

Reinhard, J., L. Starke, C. Klose, P. Haberkant, H. Hammaren, F. Stein, O. Klein, C. Berhorst, H. Stumpf, J.P. Saenz, J. Hub, M. Schuldiner, and R. Ernst. 2024. MemPrep, a new technology for isolating organellar membranes provides fingerprints of lipid bilayer stress. *EMBO J*. 43:1653-1685.

Renne, M.F., and R. Ernst. 2023. Membrane homeostasis beyond fluidity: control of membrane compressibility. *Trends Biochem Sci*. 48:963-977.

Robinson, M.S. 1997. Coats and vesicle budding. *Trends Cell Biol*. 7:99-102.

Rogov, V., V. Dotsch, T. Johansen, and V. Kirkin. 2014. Interactions between autophagy receptors and ubiquitin-like proteins form the molecular basis for selective autophagy. *Mol Cell*. 53:167-178.

Rutter, J., B.L. Probst, and S.L. McKnight. 2002. Coordinate regulation of sugar flux and translation by PAS kinase. *Cell*. 111:17-28.

Ryan, K.J., Y. Zhou, and S.R. Wente. 2007. The karyopherin Kap95 regulates nuclear pore complex assembly into intact nuclear envelopes in vivo. *Mol Biol Cell*. 18:886-898.

Schafer, J.A., J.P. Schessner, P.W. Bircham, T. Tsuji, C. Funaya, O. Pajonk, K. Schaeff, G. Ruffini, D. Papagiannidis, M. Knop, T. Fujimoto, and S. Schuck. 2020. ESCRT machinery mediates selective microautophagy of endoplasmic reticulum in yeast. *EMBO J*. 39:e102586.

Schessner, J.P., V. Albrecht, A.K. Davies, P. Sinitcyn, and G.H.H. Borner. 2023. Deep and fast label-free Dynamic Organellar Mapping. *Nat Commun*. 14:5252.

Schmidt, R.M., J.P. Schessner, G.H. Borner, and S. Schuck. 2019. The proteasome biogenesis regulator Rpn4 cooperates with the unfolded protein response to promote ER stress resistance. *Elife*. 8.

Schuck, S. 2020. Microautophagy - distinct molecular mechanisms handle cargoes of many sizes. *J Cell Sci*. 133.

Schuck, S., C.M. Gallagher, and P. Walter. 2014. ER-phagy mediates selective degradation of endoplasmic reticulum independently of the core autophagy machinery. *J Cell Sci*. 127:4078-4088.

Schuck, S., W.A. Prinz, K.S. Thorn, C. Voss, and P. Walter. 2009. Membrane expansion alleviates endoplasmic reticulum stress independently of the unfolded protein response. *J Cell Biol*. 187:525-536.

Schuldiner, M., J. Metz, V. Schmid, V. Denic, M. Rakwalska, H.D. Schmitt, B. Schwappach, and J.S. Weissman. 2008. The GET complex mediates insertion of tail-anchored proteins into the ER membrane. *Cell*. 134:634-645.

Schulz, B.L., C.U. Stirnimann, J.P. Grimshaw, M.S. Brozzo, F. Fritsch, E. Mohorko, G. Capitani, R. Glockshuber, M.G. Grutter, and M. Aebi. 2009. Oxidoreductase activity of oligosaccharyltransferase subunits Ost3p and Ost6p defines site-specific glycosylation efficiency. *Proc Natl Acad Sci U S A*. 106:11061-11066.

Schwarz, D.S., and M.D. Blower. 2016. The endoplasmic reticulum: structure, function and response to cellular signaling. *Cell Mol Life Sci*. 73:79-94.

Scott, S.V., J. Guan, M.U. Hutchins, J. Kim, and D.J. Klionsky. 2001. Cvt19 is a receptor for the cytoplasm-to-vacuole targeting pathway. *Mol Cell*. 7:1131-1141.

Seidel, M., A. Becker, F. Pereira, J.J.M. Landry, N.T.D. de Azevedo, C.M. Fusco, E. Kaindl, N. Romanov, J. Baumbach, J.D. Langer, E.M. Schuman, K.R. Patil, G. Hummer, V. Benes, and M. Beck. 2022. Co-translational assembly orchestrates competing biogenesis pathways. *Nat Commun*. 13:1224.

Shamu, C.E., and P. Walter. 1996. Oligomerization and phosphorylation of the Ire1p kinase during intracellular signaling from the endoplasmic reticulum to the nucleus. *EMBO J*. 15:3028-3039.

Shibata, Y., T. Shemesh, W.A. Prinz, A.F. Palazzo, M.M. Kozlov, and T.A. Rapoport. 2010. Mechanisms determining the morphology of the peripheral ER. *Cell*. 143:774-788.

Shpilka, T., E. Welter, N. Borovsky, N. Amar, F. Shimron, Y. Peleg, and Z. Elazar. 2015. Fatty acid synthase is preferentially degraded by autophagy upon nitrogen starvation in yeast. *Proc Natl Acad Sci U S A*. 112:1434-1439.

Skowronek, P., G. Wallmann, M. Wahle, S. Willems, and M. Mann. 2025. An accessible workflow for high-sensitivity proteomics using parallel accumulation-serial fragmentation (PASEF). *Nat Protoc*.

Smith, M.H., H.L. Ploegh, and J.S. Weissman. 2011. Road to ruin: targeting proteins for degradation in the endoplasmic reticulum. *Science*. 334:1086-1090.

Spang, A. 2015. The Road not Taken: Less Traveled Roads from the TGN to the Plasma Membrane. *Membranes (Basel)*. 5:84-98.

Steffen, K.K., M.A. McCormick, K.M. Pham, V.L. MacKay, J.R. Delaney, C.J. Murakami, M. Kaeberlein, and B.K. Kennedy. 2012. Ribosome deficiency protects against ER stress in Saccharomyces cerevisiae. *Genetics*. 191:107-118.

Stepp, J.D., K. Huang, and S.K. Lemmon. 1997. The yeast adaptor protein complex, AP-3, is essential for the efficient delivery of alkaline phosphatase by the alternate pathway to the vacuole. *J Cell Biol*. 139:1761-1774.

Strating, J.R., and G.J. Martens. 2009. The p24 family and selective transport processes at the ER-Golgi interface. *Biol Cell*. 101:495-509.

Stromhaug, P.E., F. Reggiori, J. Guan, C.W. Wang, and D.J. Klionsky. 2004. Atg21 is a phosphoinositide binding protein required for efficient lipidation and localization of Atg8 during uptake of aminopeptidase I by selective autophagy. *Mol Biol Cell*. 15:3553-3566.

Sun, M., K. Hu, J. Bewersdorf, and T.D. Pollard. 2021. Sample Preparation and Imaging Conditions Affect mEos3.2 Photophysics in Fission Yeast Cells. *Biophys J*. 120:21-34.

Sung, M.K., J.M. Reitsma, M.J. Sweredoski, S. Hess, and R.J. Deshaies. 2016. Ribosomal proteins produced in excess are degraded by the ubiquitin-proteasome system. *Mol Biol Cell*. 27:2642-2652.

Suzuki, K., Y. Kamada, and Y. Ohsumi. 2002. Studies of cargo delivery to the vacuole mediated by autophagosomes in Saccharomyces cerevisiae. *Dev Cell*. 3:815-824.

Suzuki, K., C. Kondo, M. Morimoto, and Y. Ohsumi. 2010. Selective transport of alpha-mannosidase by autophagic pathways: identification of a novel receptor, Atg34p. *J Biol Chem*. 285:30019-30025.

Suzuki, K., S. Nakamura, M. Morimoto, K. Fujii, N.N. Noda, F. Inagaki, and Y. Ohsumi. 2014. Proteomic profiling of autophagosome cargo in Saccharomyces cerevisiae. *PLoS One*. 9:e91651.

Szoradi, T., K. Schaeff, E.M. Garcia-Rivera, D.N. Itzhak, R.M. Schmidt, P.W. Bircham, K. Leiss, J. Diaz-Miyar, V.K. Chen, D. Muzzey, G.H.H. Borner, and S. Schuck. 2018. SHRED Is a Regulatory Cascade that Reprograms Ubr1 Substrate Specificity for Enhanced Protein Quality Control during Stress. *Mol Cell*. 70:1025-1037 e1025.

Takeda, E., T. Isoda, S. Hosokawa, Y. Oikawa, S. Hotta-Ren, A.I. May, and Y. Ohsumi. 2024. Receptor-mediated cargo hitchhiking on bulk autophagy. *EMBO J*. 43:3116-3140.

Takeshige, K., M. Baba, S. Tsuboi, T. Noda, and Y. Ohsumi. 1992. Autophagy in yeast demonstrated with proteinase-deficient mutants and conditions for its induction. *J Cell Biol*. 119:301-311.

TerBush, D.R., T. Maurice, D. Roth, and P. Novick. 1996. The Exocyst is a multiprotein complex required for exocytosis in Saccharomyces cerevisiae. *EMBO J*. 15:6483-6494.

Thaller, D.J., D. Tong, C.J. Marklew, N.R. Ader, P.J. Mannino, S. Borah, M.C. King, B. Ciani, and C.P. Lusk. 2021. Direct binding of ESCRT protein Chm7 to phosphatidic acid-rich membranes at nuclear envelope herniations. *J Cell Biol*. 220.

Thomas, D., and Y. Surdin-Kerjan. 1997. Metabolism of sulfur amino acids in Saccharomyces cerevisiae. *Microbiol Mol Biol Rev*. 61:503-532.

Thomas, L., B. Taleb Ismail, P. Askjaer, and G. Seydoux. 2023. Nucleoporin foci are stress-sensitive condensates dispensable for C. elegans nuclear pore assembly. *EMBO J*. 42:e112987.

Thumm, M., R. Egner, B. Koch, M. Schlumpberger, M. Straub, M. Veenhuis, and D.H. Wolf. 1994. Isolation of autophagocytosis mutants of Saccharomyces cerevisiae. *FEBS Lett*. 349:275-280.

Timney, B.L., B. Raveh, R. Mironska, J.M. Trivedi, S.J. Kim, D. Russel, S.R. Wente, A. Sali, and M.P. Rout. 2016. Simple rules for passive diffusion through the nuclear pore complex. *J Cell Biol*. 215:57-76.

Tkach, J.M., A. Yimit, A.Y. Lee, M. Riffle, M. Costanzo, D. Jaschob, J.A. Hendry, J. Ou, J. Moffat, C. Boone, T.N. Davis, C. Nislow, and G.W. Brown. 2012. Dissecting DNA damage response pathways by analysing protein localization and abundance changes during DNA replication stress. *Nat Cell Biol*. 14:966-976.

Todorow, Z., A. Spang, E. Carmack, J. Yates, and R. Schekman. 2000. Active recycling of yeast Golgi mannosyltransferase complexes through the endoplasmic reticulum. *Proc Natl Acad Sci U S A*. 97:13643-13648.

Travers, K.J., C.K. Patil, L. Wodicka, D.J. Lockhart, J.S. Weissman, and P. Walter. 2000. Functional and genomic analyses reveal an essential coordination between the unfolded protein response and ER-associated degradation. *Cell*. 101:249-258.

Tsukada, M., and Y. Ohsumi. 1993. Isolation and characterization of autophagy-defective mutants of Saccharomyces cerevisiae. *FEBS Lett*. 333:169-174.

Tyanova, S., T. Temu, and J. Cox. 2016a. The MaxQuant computational platform for mass spectrometry-based shotgun proteomics. *Nat Protoc*. 11:2301-2319.

Tyanova, S., T. Temu, P. Sinitcyn, A. Carlson, M.Y. Hein, T. Geiger, M. Mann, and J. Cox. 2016b. The Perseus computational platform for comprehensive analysis of (prote)omics data. *Nat Methods*. 13:731-740.

Ulrich, K., A. Farkas, O. Chan, O. Katamanin, B. Schwappach, and U. Jakob. 2022. From guide to guard-activation mechanism of the stress-sensing chaperone Get3. *Mol Cell*. 82:3226-3238 e3227.

Varmuza, K., and P. Filzmoser. 2009. Introduction to multivariate statistical analysis in chemometrics. CRC Press, Boca Raton. xiii, 321 p. pp.

Voeltz, G.K., W.A. Prinz, Y. Shibata, J.M. Rist, and T.A. Rapoport. 2006. A class of membrane proteins shaping the tubular endoplasmic reticulum. *Cell*. 124:573-586.

Voeltz, G.K., E.M. Sawyer, G. Hajnoczky, and W.A. Prinz. 2024. Making the connection: How membrane contact sites have changed our view of organelle biology. *Cell*. 187:257-270.

Volmer, R., K. van der Ploeg, and D. Ron. 2013. Membrane lipid saturation activates endoplasmic reticulum unfolded protein response transducers through their transmembrane domains. *Proc Natl Acad Sci U S A*. 110:4628-4633.

Walter, P., and G. Blobel. 1980. Purification of a membrane-associated protein complex required for protein translocation across the endoplasmic reticulum. *Proc Natl Acad Sci U S A*. 77:7112-7116.

Walter, P., and D. Ron. 2011. The unfolded protein response: from stress pathway to homeostatic regulation. *Science*. 334:1081-1086.

Wang, J., G. Zhang, W. Qian, and K. Li. 2024. Decoding the Heterogeneity and Specialized Function of Translation Machinery Through Ribosome Profiling in Yeast Mutants of Initiation Factors. *Adv Biol (Weinh)*. 8:e2300494.

Wang, N., Y. Shibata, J.A. Paulo, S.P. Gygi, and T.A. Rapoport. 2023. A conserved membrane curvature-generating protein is crucial for autophagosome formation in fission yeast. *Nature Communications*. 14.

Watanabe, Y., N.N. Noda, H. Kumeta, K. Suzuki, Y. Ohsumi, and F. Inagaki. 2010. Selective transport of alpha-mannosidase by autophagic pathways: structural basis for cargo recognition by Atg19 and Atg34. *J Biol Chem*. 285:30026-30033.

Weill, U., G. Krieger, Z. Avihou, R. Milo, M. Schuldiner, and D. Davidi. 2019. Assessment of GFP Tag Position on Protein Localization and Growth Fitness in Yeast. *J Mol Biol*. 431:636-641.

Weill, U., I. Yofe, E. Sass, B. Stynen, D. Davidi, J. Natarajan, R. Ben-Menachem, Z. Avihou, O. Goldman, N. Harpaz, S. Chuartzman, K. Kniazev, B. Knoblach, J. Laborenz, F. Boos, J. Kowarzyk, S. Ben-Dor, E. Zalckvar, J.M. Herrmann, R.A. Rachubinski, O. Pines, D. Rapaport, S.W. Michnick, E.D. Levy, and M. Schuldiner. 2018. Genome-wide SWAp-Tag yeast libraries for proteome exploration. *Nat Methods*. 15:617-622.

Wek, S.A., S. Zhu, and R.C. Wek. 1995. The histidyl-tRNA synthetase-related sequence in the eIF-2 alpha protein kinase GCN2 interacts with tRNA and is required for activation in response to starvation for different amino acids. *Mol Cell Biol*. 15:4497-4506.

Wu, X., C. Cabanos, and T.A. Rapoport. 2019. Structure of the post-translational protein translocation machinery of the ER membrane. *Nature*. 566:136-139.

Yamaguchi, M., N.N. Noda, H. Nakatogawa, H. Kumeta, Y. Ohsumi, and F. Inagaki. 2010. Autophagy-related protein 8 (Atg8) family interacting motif in Atg3 mediates the Atg3-Atg8 interaction and is crucial for the cytoplasm-to-vacuole targeting pathway. *J Biol Chem*. 285:29599-29607.

Yi, D.G., and W.K. Huh. 2015. UDP-glucose pyrophosphorylase Ugp1 is involved in oxidative stress response and long-term survival during stationary phase in Saccharomyces cerevisiae. *Biochem Biophys Res Commun*. 467:657-663.

Zhang, X., and Y. Wang. 2016. Glycosylation Quality Control by the Golgi Structure. *J Mol Biol*. 428:3183-3193.

7 ACKNOWLEDGEMENT

First, I would like to thank Sebastian for giving me the opportunity to work in his lab. Even though I started out with the goal to unravel the mysteries of micro-ER-phagy and got side-tracked by all the moving proteins in the ER, I came back to autophagy in the end. Thank you for always getting me excited about science again, listening to my experimental suggestions and helped me to become a better scientist. I would also like to thank Britta Brügger as my first supervisor and Matthias Mayer for acknowledging my progress throughout the four years and giving motivational input during my TACs. Thank you Georg for giving me the opportunity to learn such an awesome method in your lab, learning parts of MS experiments and providing constant data analysis input and also the patience to explain it to me. Also a huge thanks to Julia, Alex and Vincent for the nice welcome in Munich and the help with the MS measurements and data analysis. Thank you Florian and Sebastian for the perfect four days in Osnabrück to learn vacuole purification and Florian again for being part of my TAC meetings twice. And a huge thank you to Matthias Meurer for showing me and Petra how to replicate libraries. Auch ein Riesendankeschön an die Spülküche des BZH Melanie und Linda, dank euch ist die Laborarbeit so viel leichter.

A huge thank you to all past and present Schookees for making my PhD such a positive and valuable experience in my life.

Thank you Oli for sharing my weird humor, teaching me how to do lab work correctly, for always asking me if I want to join, sharing the joy of a good cup of coffee, paying every time for food and drinks (seriously it's too much) and enjoying the drinks after a good bouldering session. Thank you Lis(ssss) for always making me smile, being the emotional support I never knew I needed sometimes and sharing many bouldering sessions and coffees out of red mugs. Thank you Sibi for appreciating the very weird music I sometimes send you and sharing the knowledge about how it feels to finally stand on a surfboard for a second. Thank you Giulia for always looking out for me. Thank you Niklas for always getting me safely to bouldering, sharing biochemical advice and bringing your truly amazing Windbeuteltorte as honorary member of the ICC. Thank you Natalie for being so chill and continuing the legacy of DOMs in the lab. Thank you Rolf for also sharing my weird humor, sharing bouldering sessions, lecturing me about guitars and making me happy when you talk about your cats. Thank you Sneha for explaining Indian culture to me and also sharing the joy of autophagy. Gracias Ayita por compartir la pasión por la autofagia, mostrarme lo increíble que puede ser el arte científico y

enseñarme un poco más de español argentino. y por supuesto también gracias a carlos por enseñarme español y compartir el banco durante unos meses

Thank you Klára for the amazing crocheting, poster, painting and what not art experiences and of course sharing the scouting advices and adventure stories.

Thank you Petra for keeping the lab running, welcoming everyone and helping out and showing us the cool artistic things you do. Thank you Inge for having kept the lab running and sharing many happy images about cacti. Thank you Dimitris for showing me how to spheroplast, fractionate and getting me excited about my own results.

Thank you Uxia for sparking my interest in the Schuck lab and to Jasmin for convincing me to do my PhD here. It was a great advice!

Thank you Aurel for providing the medical, kicking and additional bouldering support in my life. You were the reason Teakwondo was so much more fun and motivating me to kick you in your face or jumping up the bouldering wall.

Danke Mama, Papa und auch Paulchen dafür, dass ihr mich einfach machen lasst und mich in allen Dingen unterstützt und immer an mich glaubt, bis zur letzten Sekunde. Bald gibt es wohl den zweiten Dr. Platzek in der Familie.

Last but not least, dear Tim, thank you for putting up with me all the 6 years and especially the support during the last weeks and only once complaining that I have not moved in yet. I am so grateful that you are the counterweight in my life to keep everything balanced and happy.